Title	Development of ELEGANTS V and Double Beta Decay of 100Mo
Author(s)	嶋, 達志
Citation	大阪大学, 1990, 博士論文
Version Type	VoR
URL	https://hdl.handle.net/11094/2553
rights	
Note	

DEVELOPMENT OF ELEGANTS V
AND
DOUBLE BETA DECAY OF ^{100}Mo

TATSUSHI SHIMA

THE OSAKA UNIVERSITY
GRADUATE SCHOOL OF SCIENCE
TOYONAKA, OSAKA

January, 1990

Abstract

A high sensitive low background detector 'ELEGANTS V' (ELEctron- GAmma-NeuTrino- Spectrometer V) has been developed. It is an emsemble of three types of detectors, large drift chambers with 868 cells for the β ray track, 16 modules of plastic scintillators for energy and timing of the β ray, and 20 modules of NaI scintillators for γ rays and X rays. The drift chamber, which is the major part of the present development, is a key detector for high selectivity of true $\beta\beta$ events from huge background ones in the low energy region of the present concerns.

This chamber system is made of low background materials. Safe operation at the underground laboratry and small Coulomb scattering effect on the electron trajectry are achieved by using He - CO_2 gas mixture. The large acceptance of $\Omega = 3.2\ \pi$ and the high efficiency of $\varepsilon \geq 98.5$ % are realized with a cylindrical shape of the electric field. The acceptance (solid angle) of the PL modules and that of the NaI modules are as large as $\Omega \simeq 3.4\ \pi$ and $\Omega \simeq 3.2\ \pi$, respectively.

The performance of ELEGANTS V has been tested at the Osaka University sea level laboratry and at the Kamioka underground laboratry. ELEGANTS V is considered to be able to investigate the neutrinoless $\beta\beta$ decay ($0\nu\beta\beta$) in the region of $T_{1/2}^{0\nu\beta\beta} \geq 10^{23}$ years.

Clean Mo source film with less than 0.5 ppb of U and Th contaminations has been developed. The first short run for a few days with both the ^{100}Mo and natural Mo sources gives $T_{1/2}^{0\nu\beta\beta} > 1.4 \times 10^{20}$ years (68 % C.L.) of the lower limit on $0\nu\beta\beta$ of ^{100}Mo. The main origin of the backgrounds at the $0\nu\beta\beta$ region is attributed to the β decay of ^{214}Bi, which is a decay product of ^{222}Rn in the air. It is indicated by careful analysis of the background events that the goal of the sensitivity up to $T_{1/2}^{0\nu\beta\beta} \sim 10^{23}$ years can be achieved by removing the remaining Rn gas in the vicinity of the plastic scintillators.

ELEGANTS V can be used not only for studying $\beta\beta$ decays of ^{100}Mo, but also for studying other $\beta\beta$ decays and other rare decays.

Contents

Chapter 1. Introduction

1-1. Rare decay physics and the $\beta\beta$ decay

Recently, many interesting works have been carried out in the field of non-accellarator physics. They provide quite valuable information on particle and nuclear physics, which cannot be obtained by experiments with accelerators. Studies of the rare decays are important and major subjects of the non-accellarator physics. It is important for experimental studies of the rare decays to develop detectors with very high sensitivity and low background.

One of the most attractive theme in the field of the rare decay physics is the neutrinoless double beta dacay ($0\nu\beta\beta$).

$0\nu\beta\beta$ process violates the lepton number consevation law. It requires the helicity mixing of the neutrino, which leads to the existence of a non-vanishing Majorana neutrino mass.The $0\nu\beta\beta$ process is considered to be due to the Majorana mass term $<\mathrm{m}_\nu>$ and/or the right handed weak current term <RHC>. $0\nu\beta\beta$ is forbidden in the frame work of the minimal standard theory of electro-weak interaction and also in SU(5) GUT (grand unified theory). So far experimental studies have given only upper limits on the neutrino mass and on the right handed weak current. There is, however, no reason to believe that the neutrino is massless and weak interaction is perfectly left handed. Actually, some of the extended electro-weak theories and GUTs predict the existence of $<\mathrm{m}_\nu>$ and <RHC>. For example, SO(10) GUT with the see-saw mechanism explaines naturally the small neutrino mass, and leads to the massive Majorana neutrino and the right handed weak interaction (Ref. 1.1). Thus the experimental study of $0\nu\beta\beta$ can provide quite stringent tests of the unified theories of the fundamental interactions.

The neutrino mass is also of interest in views of astrophysics and cosmology. There are relic neutrinos with a density of 100 to 150 per cc. in the universe. If the neutrino has a small mass of the order of eV, it may be a candidate of the cosmic dark matter.

The $\beta\beta$ decay accompanied by two neutrinos ($2\nu\beta\beta$) is allowed in the frame work of the standard electro-weak theory of $\mathrm{SU}(2)_L \times \mathrm{U}(1)$. Its experimental half life provides a good check for the caluculation of the $2\nu\beta\beta$ matrix element. Reliable values of the $0\nu\beta\beta$ nuclear matrix element are neccessary to deduce $<\mathrm{m}_\nu>$ and <RHC> from experimental $0\nu\beta\beta$ half lives. The $0\nu\beta\beta$ matrix element is closely related with the $2\nu\beta\beta$ one, which is deduced directly from the $2\nu\beta\beta$ half life. Therefore experimental studies of $2\nu\beta\beta$ is very important.

From the experimental side, development of new techniques with high sensitivity and high accuracies is quite valuable to overcome the present limits on rare decay experiments.

1-2. Theoretical aspects of the $\beta\beta$ decay

The $\beta\beta$ decay is the process that two β decays occur in a nucleus. It can be the dominant process in case that single β decay is forbidden by the pair-breaking energy cost or suppressed due to large difference of spins. The $\beta\beta$ decay can be classified into following three modes,

$$2\nu\beta\beta:\quad (A,Z) \rightarrow (A,Z+2) + 2e^- + 2\bar{\nu} \qquad (1.1.a)$$

$$0\nu\beta\beta:\quad (A,Z) \rightarrow (A,Z+2) + 2e^- \qquad (1.1.b)$$

$$0\nu B\beta\beta:\quad (A,Z) \rightarrow (A,Z+2) + 2e^- + B \qquad (1.1.c)$$

where B is the massless neutral Goldstone boson, named Majoron, which arises in the B(baryon number) – L(lepton number) symmetry breaking GUT.

Figure 1.1 shows the decay diagrams of the $\beta\beta$ decays involving two nucleons. Figure 1.1(a), (b) and (c) are the diagrams of $2\nu\beta\beta$, $0\nu\beta\beta$, and $0\nu B\beta\beta$, respectively. There are other processes involving the Δ-isober (Ref. 1.2,) , the π or ρ meson exchange currents (Ref. 1.3), Higgs particle(Ref. 1.4), and the gaugeno (Ref. 1.5), as shown in Figure 1.2 (a) ~ (c), (d), (e) ~ (i), and (j), respectively.

Since the $\beta\beta$ decay is the second order process of the weak interaction, the theoretically estimated half life is extremely long, and it may be longer than 10^{17} years for $2\nu\beta\beta$, and 10^{22} years for $0\nu\beta\beta$ with 1 eV of $<m_\nu>$ (Ref. 1.6).

The $0\nu\beta\beta$ process, which is beyond the standard model, implies followings (Ref. 1.7).

1) Neutrino is the Majorana particle and not the Dirac particle, i.e. neutrino and anti-neutrino are the same particle ($\nu = \bar{\nu}$).
2) Neutrino has a finite (non-zero) Majorana mass ($<m_\nu>$).
3) There must be a finite mixing of the neutrino helicity, which is due to the finite $<m_\nu>$ or the finite <RHC>.

If these conditions are satisfied, the virtual neutrino following the β decay of one neutron (or one d-quark) can be absorbed by another nucleon (or quark) to make another β decay. Consequently, no neutrino is emitted.

$0\nu\beta\beta$ occurs according to the following hamiltonian generalized under the left-right symmetric electro-weak theory like $SU(2)_L \times SU(2)_R \times U(1)$ (Ref. 1.7).

$$H_W = G/\sqrt{2}\ [\, j_L^\rho J_{L\rho}^\dagger + \kappa j_L^\rho J_{R\rho}^\dagger + \eta j_R^\rho J_{L\rho}^\dagger + \lambda j_R^\rho J_{R\rho}^\dagger)\ ] + \text{h.c.}\ , \tag{1.2}$$

where j and J represent the leptonic and the hadronic currents, respectively. L and R mean light handed and right handed, respectively. The first term in eq.(1.2) corresponds to the hamiltonian of the standard model with the finite $<m_\nu>$, and others represent right handed V+A interactions. κ, η, and λ are coupling constants. The half life of the $0\nu\beta\beta$ $0^+ \rightarrow 0^+$ transition is expressed as follows;

$$T_{1/2}^{0\nu}(0^+ \rightarrow 0^+) = [\log 2 \cdot F(x,y,z) \cdot |M_{GT}^{0\nu}|^2]^{-1} \tag{1.3.a}$$

$$F(x,y,z) = c_1x^2 + c_2xy\cdot\cos(\psi + \alpha) + c_3xz\cdot\cos\psi + c_4y^2 + c_5z^2 + c_6yz\cdot\cos\alpha \tag{1.3.b}$$

$$\psi = \arg[\textstyle\sum_j (m_j/m_e)\cdot U_{ej} \times (\sum_j U_{ej}\cdot V_{ej})] \tag{1.3.c}$$

$$\alpha = \arg(g_v'/g_v) \tag{1.3.d}$$

$$x = |\textstyle\sum_j m_j\cdot U_{ej}^2|/m_e,$$

$$y = \lambda\cdot|\textstyle\sum_j U_{ej}\cdot V_{ej}|\cdot|g_v'/g_v|,$$

$$z = \eta\cdot|\textstyle\sum_j U_{ej}\cdot V_{ej}| \tag{1.3.e}$$

Here $M_{GT}^{0\nu}$ is the Gamow-Teller nuclear matrix element for the $0\nu\beta\beta$ $0^+ \rightarrow 0^+$ transition, c_i are coefficients which include nuclear and kinematical factors, and U and V are the mixing matrices between flavor eigenstates and mass eigenstates of the neutrinos. Here the term with κ can be omitted, because it is much smaller than unity and always appears as $(1\pm\kappa)$ form.

In case of $0\nu B\beta\beta$ the half life is expressed as

$$T_{1/2}^{0\nu B} = [\log 2\cdot G_B^{0\nu}\cdot |\ M_{\beta\beta}^{0\nu}|^2\cdot <g_B>^2\ ]^{-1} \tag{1.4}$$

where $G_B^{0\nu}$ is the kinematical factor, and $<g_B>$ is given by $\Sigma\ g_{ik}\cdot U_{ei}\cdot U_{ek}$ with g_{ik} being coupling coefficients of the Majorana neutrino to the Majoron field.

In case of the $2\nu\beta\beta$ the half life is simply written as

$$T_{1/2}^{2\nu} = [\log 2\cdot G^{2\nu}\cdot |\ M_{\beta\beta}^{2\nu}|^2\ ]^{-1}, \tag{1.5}$$

where $G^{2\nu}$ and $M_{\beta\beta}^{2\nu}$ are the kinematical factor and the nuclear matrix element, respectively. The $2\nu\beta\beta$ halflife gives the $2\nu\beta\beta$ matrix element $M_{\beta\beta}^{2\nu}$ with 1^+. It is closely related to the 1^+ compornent of $M_{\beta\beta}^{0\nu}$. Since the 1^+ component is the major one of $M_{GT}^{0\nu}$, $M_{\beta\beta}^{2\nu}$ gives a good guideline to calucurations of $M_{GT}^{0\nu}$.

1-3. Experimental study of the $\beta\beta$ decay

There are two methods of the $\beta\beta$ decay experiment; one is the direct counting method, and another is the geochemical method.

(1) Direct counting method

In the direct counting method (Ref. 1.8), the two β rays (and also the γ ray in case that the $0^+ \rightarrow 2^+$ transition takes place) are detected directly by counters. This metod has following features and advantages;

1) The $\beta\beta$ decay is an extremely rare process, and the counting rate of the true $\beta\beta$ event is expected to be of the order of or less than 1 part of 10^8 or 10^9 of background events. Thus one needs detectors with very high sensitivity and selectivity. The high sensitivity and the high selectivity may be achieved to some extent by high resolution measurements for energy, time, and track of two β rays, and by proper combination of various kinds of detectors with high sensitivity.

2) The transition probability is proportional to the square of the nuclear matrix element, and to roughly 5th power of the Q value in $0\nu\beta\beta$ and 11th in $2\nu\beta\beta$. Then nuclei with large $\beta\beta$ matrix elements and large Q values are efficient as the $\beta\beta$ source nuclei. These nuclei can be called the nuclei with high $\beta\beta$ nuclear sensitivity.

3) It is possible to distinguish $0\nu\beta\beta$ from $2\nu\beta\beta$ by measuring the sum energy soectrum of the two β rays. Measurement of the energy- and the angular- correlations of the two β rays is used to identify the terms ($<m_\nu>$, <RHC>) responsible for $0\nu\beta\beta$. Detection of the $2^+ \rightarrow 0^+$ γ ray enables one to separate the $0^+ \rightarrow 0^+$ $\beta\beta$ decay from the $0^+ \rightarrow 2^+$ $\beta\beta$ decay.

Previously, the $\beta\beta$ decay of ^{76}Ge has been extensively studied (Ref. 1.8). Since natural germanium containes 7.78 % of ^{76}Ge, the Ge detector itself is used as the ^{76}Ge $\beta\beta$ source. Use of the germanium solid state detector is one of the most effective ways to investigate $0\nu\beta\beta$. It has almost 100 % of the detection efficiency and the best energy resolution without any energy loss. The world record of the lower limit on the half life for $0\nu\beta\beta$ of ^{76}Ge is 1.1×10^{24} years (68 % C.L.) (Ref. 1.8), which is given by the UCSB and LBL collaboration. In the same sense, ^{48}Ca in the CaF_2 scintillator and ^{136}Xe with high pressure gas chamber or liquid chamber are also attractive (Ref. 1.9). As a matter of fact, the source nuclei are limitted to such special nuclei that are used also for detectors.

Another effective way of the direct measurement is to measure $\beta\beta$ decays of more suitable nuclei than ^{76}Ge by using detectors separated from the source. Then one can study various kinds of $\beta\beta$ source nuclei with large $M^{0\nu}_{\beta\beta}$ and/or large $Q_{\beta\beta}$, even with large amount. It also become possible to measure energy- and angular- correlations of the two β rays and also the γ ray of the $0^+ \rightarrow 2^+$ transition).
UCI group observed first $2\nu\beta\beta$ of ^{82}Se, and the experimental half life was obtained as 2×10^{18} years (90 % C.L.) (Ref. 1.10). The Osaka group is carrying on the measurement of ^{100}Mo with the Si(Li) solid state detector array, called 'ELEGANTS IV' (Ref. 1.11). ^{100}Mo is one of the good candidates for the $\beta\beta$ source nuclei, because it has a very large Q value ($Q_{\beta\beta}$ = 3.034 MeV), and is expected to have a large nuclear matrix element. ELEGANTS IV uses 11 modules of Si(Li) detectors and ten sheets of the ^{100}Mo source foils in between. It is possible to measure the energy correlation of the two β rays. A lower limit on the half life of $2\nu\beta\beta$ was obtained as (Ref. 1.11)

$$T^{2\nu}_{1/2} > 5.4 \times 10^{18} \text{ yrs (90 \% C.L., on } 2\nu\beta\beta) \tag{1.6}$$

The ^{100}Mo experiment with Si(Li) detecters is also carried out by LBL group, and they give following limits (Ref. 1.12).

$$T^{0\nu}_{1/2} > 4 \times 10^{21} \text{ yrs (68 \% C.L., on } 0^+ \rightarrow 0^+) \tag{1.7.a}$$

$$T^{0\nu}_{1/2} > 4 \times 10^{20} \text{ yrs (68 \% C.L., on } 0^+ \rightarrow 2^+) \tag{1.7.b}$$

The results for ^{100}Mo are summarized in Table 1.1.

QRPA (quasi-particle random phase approximation) theories predict that the $2\nu\beta\beta$ matrix element with 1^+ is very sensitive to the particle - particle coupling strength (g_{pp}) and the cancellation mechanism suppresses the transition amplitude, especially in $2\nu\beta\beta$ of ^{100}Mo (Ref. 1.13, 1.14). Thus $2\nu\beta\beta$ of ^{100}Mo is also a matter of great interest from the view point of the nuclear structure theories. The nuclear matrix element for $0\nu\beta\beta$, however, is considered to be not suppressed much because $0\nu\beta\beta$ involves not only the 1^+ compornent of the intermediate states but also many higher spin 2^-, 3^+, 4^-,... compornents due to energetic virtual neutrino. The cancellation is effective mainly for the 1^+ compornent, but not for the higher spin ones.

(2) Geochemical method

The geochemical method measures the total amount of the daughter nuclei of the $\beta\beta$ decay in the old ore by mass spectroscopy. It is concidered that the excess of the isotope abundance compared with that of the atmosphere is due to the $\beta\beta$ decay

(Ref. 1.19). The advantage of this method is the very long effective measurement time, which is about the age of the ore, which is $10^7 \sim 10^9$ years. This method, however, has following demerits;

1) There is some ambiguity on the age of the ore.
2) The daughter nuclei may escape or may be produced by other processes.
3) Source nuclei is limited to such nuclei that the daughter nuclei are of rare gas form to be ready for the mass analysis.
4) No information about the energy, the timing, and the trajectry of the β rays. No imformation about γ rays.

Thus one can get only inclusive data. $0\nu\beta\beta$ and $2\nu\beta\beta$, the $0^+ \rightarrow 0^+$ $\beta\beta$ decay and the $0^+ \rightarrow 2^+$ ones, and contributions of the terms $<m\nu>$ and <RHC> in the $0\nu\beta\beta$ Hamiltonian are not identified.

1-4. Development of the low background detector

In most case of rare decay measurements, the true decay rate is smaller than the rate of the backgrounds even after all kinds of conditions (cuts). Thus the sensitivity of the detector for rare decay studies is limited by the background rate. The maximum half life (the minimum decay rate) to be measured is expressed as follows.

$$T_{1/2}(\text{max.}) < \ln 2 \cdot N_o \cdot k \cdot t / \sqrt{n_{BG} \cdot \Delta E \cdot t} \qquad (1.8)$$

where $T_{1/2}(\text{max.})$ is the detection limit of the half life, N_o is the number of the source nuclei, k is the detection efficiency, n_{BG} is the back ground density, ΔE is energy resolution of the detector around the energy of the present concerns, and t is the measurement time. Key points for the rare decay detector are;

(1) to use large amount of the source (large N_o),
(2) to use detectors with high efficiency (large k),
(3) to realize very low background circumstance and high selectivity of the true events (small n_{BG}),
(4) to measure for a long time, actualy a few years, with good stability (long t).

Consequently advanced rare decay detectors must have high effciency (solid angle) and such large size (volume) that large amount of the source can be used. They are made of low background materials, well shielded by heavy metals against the external radiation, and are placed in mine or tunnel to avoid cosmic rays.

A new rare decay detector, called 'ELEGANTS V' (ELEctron- GAmma- NeuTrino-Spectrometer- V), has been developed by our group (Ref. 1.20). In addition to the features mentioned above, ELEGANTS V has very excellent selectivity of the true events from the background ones, as described in Chapter 2.

Chapter 2. Outline of ELEGANTS V

2-1. Aims

ELEGANTS V has following aims;

1) Search for $0\nu\beta\beta$ in the region of $T^{0\nu}_{1/2} > 10^{23}$ years for ^{100}Mo. This life time region corresponds to $<m_\nu> \leq 0.5$ eV, and $<\lambda> \leq 5 \times 10^{-6}$. ELEGANTS V can measure the $\beta\beta$ decay with at least one order of magnitude better sensitivity than previous experiments, as shown in Table 1.1.
2) Measurement of $2\nu\beta\beta$ with good statistics.
3) Study of the energy- and angular- correlations between the two β rays, and γ rays in case of the $0^+ \rightarrow 2^+$ $\beta\beta$ decay.
4) Development of the ultra low background detector which is used for external sources. Such detector enables one to study various kinds of $\beta\beta$ nuclei, and other kinds of rare decays.

2-2. Requirements

The goal of ELEGANTS V is to achieve sensitivity up to about 10^{23} years in $T^{0\nu}_{1/2}$. A few events have to be detected for one year measurement with a few mols of the $\beta\beta$ source. The backgrounds (BG) due to natural radioactivities or cosmic rays are more than 10^9 or 10^{10} events per year without any active or non-active shilds at the sea-level laboratry. It is essential to reject the backgrounds and to select true. The true $\beta\beta$ events are found by observing the excess of the number of the true events ($N_{\beta\beta}$) from the fluctuation of the background events (N_{BG}) after various kinds of selections (cuts), i.e.

$$N_{\beta\beta} > \sqrt{N_{BG}} \tag{2.1}$$

$N_{\beta\beta}$ is expressed in terms of the number of source nuclei N_o, the measurement time t, the detector efficiency k, the kinematical factor G, the nuclear matrix element $M_{\beta\beta}$, and the half life $T^{\beta\beta}_{1/2}$. It is written as

$$N_{\beta\beta} = N_o \cdot t \cdot k \cdot \ln 2/T^{\beta\beta}_{1/2} \cdot G \cdot |M_{\beta\beta}|^2. \tag{2.2}$$

N_{BG} is expressed as,

$$N_{BG} = n_{BG} \cdot \Delta E \cdot t, \tag{2.3}$$

where n_{BG} and ΔE are the background density and the energy resolution at the energy concerned. Defining the nuclear sensitivity S_N and the detector sensitivity S_D as

$$S_N = G \cdot |M_{\beta\beta}|^2, \tag{2.4}$$

$$S_D = N_o \cdot k \cdot t / \sqrt{n_{BG} \cdot \Delta E \cdot t}, \tag{2.5}$$

the observable limit on $T_{1/2}^{\beta\beta}$ is simply expressed as

$$T_{1/2}^{\beta\beta} < \ln 2 \cdot S_N \cdot S_D. \tag{2.6}$$

In general source nuclei with large S_N and detectors with large S_D are required for studying rare decays in the large $T_{1/2}$ region. In practice, following conditions are required.

(1) The source nucleus with large S_N.

The kinematical factor G is roughly proportional to the 5th, 7th, and 11th power of the Q value for $0\nu\beta\beta$, $0\nu B\beta\beta$, and $2\nu\beta\beta$, respectively. In ELEGANTS V, 93.5 % enriched ^{100}Mo is used as the $\beta\beta$ source nucleus. ^{100}Mo is expected to have a large $M_{\beta\beta}$. Since the Q value is as large as 3.034 MeV, G for $0\nu\beta\beta$ is about 8 times larger than that of ^{76}Ge. Since the sum energy $E_{\beta\beta}$ = Q for $0\nu\beta\beta$ exceed most of β and γ ray energies from natural radioactivities, origins of background events at the $0\nu\beta\beta$ energy region are limited to ^{214}Bi in U chain, ^{208}Tl in Th chain, and cosmic rays.

(2) Large number of the $\beta\beta$ source nuclei.
ELEGANTS V uses 200 g of the enriched ^{100}Mo isotope. The number of the ^{100}Mo nuclei is 1.2×10^{24} which is about 2 mols.

(3) High detection efficiency and large acceptance of the solid angle.

ELEGANTS V uses plastic scintillators for the β ray detection. They can detect charged particles with almost 100 % of the detection efficiency, while the sensitivity for background γ rays is very small. Since large plastic scintillators are available, large acceptance is easily realized. In case of ELEGANTS V, 3.2 π of the solid angle is covered by the plastic scintillators. Total efficiency is as large as 54 % for $0\nu\beta\beta$.

(4) Low background.

Radioactive contaminants in all materials used for ELEGANTS V have been checked. They were sufficintly small. The whole β and γ detector system is surrounded by 15 cm thick lead and 10 cm OFHC to reject external γ rays from environment. Detectors and shields are kept airtight, and pure N_2 gas is circulated to purge ^{220}Rn and ^{222}Rn in the air around the detectors. ELEGANTS V is set in the Kamioka underground laboratory at 1000 m depth (2700 m w.e.) to reduce cosmic rays.

(5) High selectivity of the true event from backgrounds.

ELEGANTS V consists of three types of detectors, drift chambers (DC), plastic scintillators (PL), and NaI scintillators (NaI). DC detects the tracks of the β rays and other charged particles. The angle between the two β rays of $0\nu\beta\beta$ can be measured. Some of the advanced $\beta\beta$ decay detectors have gas chambers like TPC (time projection chamber) (Ref. 2.1) or MWPC (multi wire proportional chamber) (Ref. 2.2), because it is essential for identification of the $\beta\beta$ decay to observe tracks and vertex of the two β rays. The energy resolution of TPC is almost same as the plastic scintillator. Thus TPC has no advantage in general, except for studying the ^{136}Xe $\beta\beta$ decay where high pressure Xe TPC can be used. MWPC does not have sufficient spatial resolution to examine the $\beta\beta$ vertex point. On the other hand, DC has very good spatial resolution. Use of DC together triggered by PL is effective for reducing backgrounds. The energy and the timing of the two β rays are measured by PL. NaI is used as a veto counter to reject background γ rays and cosmic rays, and is used as a coincidence counter for the $2^+ \rightarrow 0^+$ γ ray following the $0^+ \rightarrow 2^+ \beta\beta$ transition. The combination of these detectors is powerful for reducing all kinds of background events.

2-3. Detectors

As shown in Figure 2.1, ELEGANTS V consists of three types of detectors.

(1) Drift Chamber (DC)

DC system is placed at the center of ELEGANTS V. It consists of 12 planes, each plane consisting of 72 cells. The sensitive volume is 864 mm × 864 mm × 200 mm. The $\beta\beta$ source film is suspended between 6th and 7th plane. The trajectries of the two β rays and the vertix are determined. Details of this DC system are discribed in Chapter 3.

(2) Plastic scintillator (PL)

Two types (type A and type B) of the plastic scintillation counters are used to get the energy and the timing signals of the β rays. Type A with 12 cm (W) × 100 cm (L) × 1.5 cm (t) is made of the BC408 scintillator provided by BICRON Co., Ltd. Two H1161 (2 inch diameter) PM tubes through 20 cm long light guides are attached on both ends of each PL module. The 16 modules of type A PLs are used. The 8 PL's are placed at the top side of DC, and other 8 are at the bottom side. The total acceptance of 16 PLs are as large as 80 % for the β rays emitted from the source plane. The 24 PL modulesof the type B are arranged at the inner walls of DC, 6 modules at each side. Each modules has 2.1 cm (W) × 90 cm (L) × 1.1 cm (t) effective volume, and is also made of BC408. The 10 cm long light guide and the R1450 (3/4 inch diameter) PM tube are used at each end. Neary 90 % of the total solid angle is covered by the type A and the type B PL modules, and about 70 % of the overall detection efficiency is achieved for the $0\nu\beta\beta$ $0^+ \rightarrow 0^+$ transition caused by the $<m_\nu>$ term. Figure 2.4 shows the energy resolutions of the type A and the type B PL modules, which are obtained from the shape of the measured Compton edge for discrete γ rays. The energy resolution ΔE (full width at half maximum) is given by the following equation.

$$\Delta E = E(0.12) - E(0.88). \tag{2.7}$$

Here E(0.12) and E(0.88) are the energys where height of the spectrum are 12 % and 88 % of the maximum height of the Compton edge, respectively (see Figure 2.3). The validity of this relation has been checked by the Monte Carlo simulation and by measuring monoenergetic electrons from the ^{90}Y β ray source selected by the electron spectrometer TESS (Ref. 2.3). ΔE = 140 keV is obtained for 1.5 MeV electron. Taking into account the energy loss in the $\beta\beta$ source film, the overall energy resolution for $0\nu\beta\beta$ $0^+ \rightarrow 0^+$ transition of ^{100}Mo is estimated to be ΔE = 250 keV at around 3 MeV by the Monte

Carlo simulation. The resolution of the time difference between the PM tubes at both ends of one PL is 700 psec (FWHM) at 1.5 MeV.

(3) NaI scintillator (NaI)

NaI scintillators have two roles, one is to select the $0^+ \rightarrow 2^+$ $\beta\beta$ decay by measuring the γ ray from the 2^+ excited state of ^{100}Ru in coincidence with the $\beta\beta$ decay, and another is to veto background γ rays and cosmic rays. The NaI array consists of 20 modules of the 10 cm (H) × 10 cm (W) × 100 cm (L) sigle polyscin crystal provided by Harshaw Co., Ltd. The 10 cm × 10 cm × 10 cm quartz light guide and 3.5 inch PM tube are attached at both ends of each crystal. Ordinaly NaI crystal contains about 1 ppm potasium. The NaI crystals used for ELEGANTS V has been purified. Potasium content is less than 0.3 ppm. K-free glass has been used as the window of the PM tubes. A quartz light guide is inserted between the NaI crystal end and the PM tube in order to absorb the γ rays from PM tubes. The γ rays are reduced down to be 1/40.

The energy resolution was measured at several energys by using standard γ ray sources. It is shown in Figure 2.5 as a function of the energy of the γ ray. In this measurement, the γ ray was not collimated, and the source was placed at 1 m apart from the center of the NaI crystal. The energy resolution for the ^{137}Cs 662 keV γ ray is 7.7 % (FWHM). Pulse height difference between PM tubes of both ends is discribed in terms of so-called roll-off ratio defined as

$$\mathrm{R} = (\, \mathrm{V}_L - \mathrm{V}_R \,)/(\, \mathrm{V}_L + \mathrm{V}_R \,), \tag{2.8}$$

where V_L and V_R correspond to light outputs from left and right ends, respectively. Figure 2.6 shows the measured value for R as a function of the position of the NaI crystal along the long axis. At the center of the crystal, Δx = 20 cm (FWHM) is obtained as the position resolution.

2-4. Shields and Radon rejection

(1) Shields

All detectors are surrounded by 10 cm thick OFHC and 15 cm thick lead. External γ rays due to ^{40}K, U-chain, Th-chain, and so on, are reduced to 10^{-3}. OFHC and lead have been checked for contamination of natural radioactivities. The amounts of radioactive contamination of them are given in Table 2.1.

(2) Radon rejection

^{220}Rn and ^{222}Rn in the air are also background sources. Especially, ^{222}Rn produces ^{214}Bi, which causes one of the most serious backgrounds, as discussed in Chapter 4. The radon gas content in the underground laboratry is roughly 15 times larger than that in the sea level laboratry. ELEGANTS V is kept airtight, and pure N_2 gas provided by evapolation of liquid N_2 is circulated to purge radon gas arround the detectors of ELEGANTS V.

2-5. Electronics and Data acquisition

There are 32 energy and 32 timing signals from the 32 PM tubes of the 16 PL modules, and 40 energy and 40 timing signals from each PM tubes of the 20 NaI modules. They are taken by LeCroy 2248A ADCs and LeCroy 2228A TDCs. About 1000 ch signals from DC are amplified and are discriminated by KAIZU TYPE 1 Amp. & Discri. Card. ECL logic outputs are digitized by LeCroy 4291B 32 ch TDCs and condensed by LeCroy 4298B TDC controller. All digitized data are acquired by the micro-PDP 11/53 mini computer through CAMAC, and are accumulated into a 1 Gb hard disk. Stored data are dumped from the hard disk into magnetic tapes once a week, and are sent to Osaka. These data are analyzed by the FACOM M360 computer.

Chapter 3. Development of the Drift Chamber

3-1. Requirements for DC

The drift chamber (DC) is the most important detector of ELEGANTS V. Therefore we have developed a new type of DC in the present work for studying rare $\beta\beta$ decays. Following conditions are required for DC.

1) Low background.

Radioactive contaminants in the material used for DC, which is placed close to the source, should be small.

2) High efficiency for β ray and α ray.

High efficiency and large acceptance for the β rays from the source plane are neccessary. DC is required to accept most of the β rays emitted from the source plane with very wide angular distribution. The most serious background source in the measurement of $0\nu\beta\beta$ is ^{214}Bi contaminated in the $\beta\beta$ source. ^{214}Bi has the Q value of 3.27 MeV, which is close to $Q_{\beta\beta}$ = 3.03 MeV for ^{100}Mo. Then the β ray from ^{214}Bi followed by internal conversion or Compton scattering contributes to the background events in the $0\nu\beta\beta$ energy region. This process cannot be rejected just by looking at the tracks of the β ray and the electron, since two tracks cross at just one point on the source plane like the true $\beta\beta$ event. The β decay of ^{214}Bi, however, is followed by the α decay with E_α = 7.41 MeV and $T_{1/2}$ = 164 μs as shown in Figure 3.1. Thus they can be rejected by detecting the delayed α ray. Then large detection efficiency for the α ray is also required.

3) High spatial resolution for trajectry.

Energies of most β rays of the present concerns are less than 3 MeV of the energy. Such low energy β rays are easily Coulomb scattered and their tracks are bent. In order to get high spatial resolution for trajectries and vertices, such multiple scattering effect should be as small as possible.

4) Long run stability and safe operation;

Since the rare decay measurement runs for one year or longer, DC has to work stable for such a long time. Since DC is placed at the closed underground room, flammable quenching gas, such as ethan, iso-buthan, etc, should be avoided for safety.

3-2. Design of DC

A new DC system has been developed so as to meet the requirements as given in Chapter 3.1.

(1) Materials and compornents

The main frame of DC is made of OFHC. Selected stainless steel is used for the window frame and for other mechanically stressed parts. Glass epoxy, which has been used conventionally for a frame of multi wire chambers, contains 10 ~ 20 pCi/kg of U-chain and Th-chain isotopes. Thus glass epoxy is not suitable for the present case. Cathode and field wires with 100 μm diameter are also made of OFHC. Low background gold plated tungstain wire with 30 μm diameter was selected to be used as the anode wires. These wires were stretched between the frames of DC with feed-throughs made of delrine, and were soldered to brass pipe electrodes. Radioactivities contained in the feed-throughs, the brass pipes, the solders, and the flux used were measured to be quite small. The signal read out assembly is also made of OFHC and delrine. The data of the radioactivities in the materials used are listed in Table 3.1.

(2) Structure

Figure 3.2(a) and (b) are the top view and the side view of the DC system, respectively. This system consists of two large chambers (track chamber) and one thin chamber (vertex chamber).

The track chambers are used to identify trajectories of the β rays and other charged particles. Each track chamber has 6 layers, 3 for x-direction and other 3 for y-direction, and each layer has 72 cells eacept 2nd and 4th layers. These two layers have 73 cells. The active volume of each track chamber is 864 mm (W) × 864 mm (D) × 72 mm (H).

The cell structure is shown in Figure 3.3. The cross section is 12 mm × 12 mm square. The anode wire is placed at the center of the square, and all the field wires and the cathode wires above the anode plane run pararell to the anode wire with 6 mm gap. The cathode wires below the anode plane are parpendicular to the anode wire. Then the anode wires of one anode plane are also parpendicular to those of the neighboring anode plane. Each cathode plane acts as a common cathode plane for the layers of above and below. Thus the total thickness of the track chamber is saved so as to get large acceptance.

As shown in Figure 3.3, the contor of the electric field in one cell is cylindrical. A conventional DC has a long drift region with uniform field gradient. Such type of DC may leads to miss-reconstruction of the trajectry in case the charged particle passes through the DC plane with small angle between plane and trajectry, as shown in Figure 3.4. In the present DC, however, the trajectory is identified as a common tangential line to the circles with diameter corresponds to the drift times. Thus the right trajectry can be reconstructed independent of the incident angle.

(3) Counter gas

Performance of the He - CO_2 has been tested. He gas is the best choice for the main compornent of the counter gas, because multiple scattering effect is very small. Figure 3.5 shows examples of Monte Carlo caluculations for the trajectries of the β rays in (a) ; Ar - CO_2 85:15 mixture and (b) ; He - CO_2 85:15 mixture. CO_2 gas is adequate for safe operation in a closed room.

(4) Read out and electronics

The outputs from the anode wires are sent for a distance of 50 cm by high voltage cables and are decoupled from the HV cables by 470 pF capacitors. These HV cables were not covered by shield insulator, which contains radioactivities (see Table 3.1). Decoupling capacitors and bleeder resistors are packed every 16 channels in one box made of OFHC.

Signals decoupled from HV are sent by 4 m long twisted pair ribbon cables to the Amp. and Discri. Cards. They are converted into the ECL logic signals. These ECL signals are fed into LeCroy 4291B TDC starts via 15m long twisted pairs.

3-3. Performance

The performance of He - CO_2 gas mixture has not yet been well known. Following studies were carried (Ref. 3.1).

(1) Detection efficency for charged particles

i) Track chamber

The efficiency of the track chamber was measured by using cosmic rays as a function of the applied high voltage.
Experimental set up is shown in Figure 3.6. The efficiency ε of one layer is defined as

$$\varepsilon = \{N(\text{OR}) \cap N(\text{upper PL}) \cap N(\text{lower PL})\}/\{N(\text{upper PL}) \cap N(\text{lower PL})\}, \tag{3.1}$$

where $N(\text{OR})$ is the number of events in which at least one cell in the layer concerned gives a signal, $N(\text{upper PL})$ is the number of events detected by upper PLs, and $N(\text{lower PL})$ is the number of events detected by lower PLs.

ε is shown in Figure 3.7 as a function of the applied high voltage. The range of the efficiency plateau, which is defined as the range of the high voltage that gives the efficiency ε better than 95 %, is about 70 V for all layers. The efficiency of $\varepsilon = 99.2$ % is reached as the average of the maximum efficiencies of all layers. These efficiencies are considered to be quite satisefactry for the present case of He and CO_2 mixture, by noting the fact that the number of the primary ion pairs produced by a charged particle in He gas is about 10 times smaller than that in Ar or other noble gas.

ii) Vertex chamber

The efficiency of the vertex chamber for cosmic rays was measured by the similar way as in case of the track chamber. The result is shown in Figure 3.8. Maximum efficiency is about 90 %, and the range of the efficiency plateau is 30 volts. These values are not quite good. The main reason is maybe that the field strength is not enough for gas amplification, because there is no field wire between one anode wire and another.

Figure 3.9 shows the experimental set up to measure the efficiency for α particles. The α ray from ^{241}Am (E_α =5.41 MeV) was collimated and the intensity was measured by Si SSD. Counting rate of the collimated α rays was 6.85 cps. The counting rates by the vertex chamber were measured alternatively with and without the α beam. In the run without the α beam, α particles were stopped by 100 μm thick Al foil in front of the slit.

Figure 3.10 (a) and (b) are the pulse height spectra with the α beam and without the α beam, respectively. It is found that the α particle produces a clear peak with large pulse height. So α particles can be easily distinguished from the background signals, which are concentrated mostly at the low-pulse height region. Thus number of the α particles are obtained by counting the signals beyond a threshold V_{th} as shown in Figure 3.10. The detection efficiency is defined as follows.

$$\varepsilon_\alpha = (N_\alpha - N_{no\ \alpha}) / N_o \tag{3.2}$$

Here N_α means the counting rate of the signals above V_{th} with the α beam, and $N_{no\ \alpha}$ is that without the α beam where the α particles are stopped by the Al foil. N_o stands for the counting rate of the incident α particle.

Figure 3.11 shows the efficiency ε_α as a function of the distance d from the anode wire. The pulse height threshold was chosen at 600 ch in Figure 3.10. The efficiency of $\varepsilon_\alpha = 80 \sim 85$ % are achieved in the region between the anode (d = 0 mm) and the point of d = 6 mm. Here d is the distance from the anode wire. In the region of d larger than 7 mm, ε_α is less than 70 %. The reduction of the background is considered to be due to the weak field there.

The counting rate of the background in the region over 600 ch was 0.11 cps for one cell, which is much smaller than the rate N_o = 6.85 cps.

(2) Drift velocity and spatial resolution

i) Drift velocity

The relation between the field strength and the drift velocity was measured by using chaged cosmic rays, which are mostly muons.

The drift length X is given by a function of the drift time t as X(t). Let's take events which have the same drift time in the first and the third layer, i.e. $t_1 = t_3$. Here t_i denotes the drift time in the cell of i-th layer. Since the second layer is shifted by a half cell (6 mm) with respect to the first and the third layers, the following relation is obtained (see Figure 3.14).

$$X(t_1) + X(t_2) = 6 \text{ (mm)} \quad (t_1 = t_3) . \tag{3.3}$$

Assuming that X(t) is expressed as a quadratic function,

$$X(t) = a\, t^2 + b\, t + c , \tag{3.4}$$

eq. (3.3) is rewritten as

$$(t_1^2 + t_2^2)\cdot a + (t_1 + t_2)\cdot b + c = 6 . \tag{3.5}$$

The experimental set up is same as Figure 3.6. By selecting the events which have the same drift time in the first and the third layers, twenty sets of ($t_{1,i}$, $t_{2,i}$) were obtained as shown in Figure 3.12.

The parameters a, b, and c were obtained by the least square fit to the measured data for t_1 and t_2.

Then by using these parameters a, b, and c, X(t) is expressed as follows.

$$X(t \text{ nsec}) = -6.48\cdot t^2 + 3.97\cdot t + 0.03 \ (\text{mm}, 0 \text{ mm} \leq X \leq 4.5 \text{ mm}) \tag{3.6}$$

The drift velocity W is obtained from eq. (3.6) as a function of the drift time t as

$$W(t \text{ nsec}) \equiv dX(t)/dt = -13.0\cdot t + 3.97 \ (\text{mm/nsec}). \tag{3.7}$$

The drift velocity W(X) as a function of the drift length X is deduced from eq. (3.6) and eq. (3.7) as

$$W(X) = \sqrt{16.6 \ - \ 25.9\cdot X} \quad (\text{mm/nsec}), \tag{3.8}$$

for the region of $0 \text{ mm} \leq X \leq 4.5 \text{ mm}$. The field strength in one cell is calcurated as shown in Figure 3.3. With this field map and W(X), the relation between the drift velocity W and the field strength E is obtained as given in Figure 3.13.

Validity of the obtained X(t) (eq.(3.6)) has been checked by another way. The tracks which have the drift times of $t_1 = 0$ and $t_3 = 0$. Such tracks pass through the point with X = 6 mm on the second plane, as shown in Figure 3.14(a). Then t(6 mm) is obtained as t_2, which is the drift time on the second plane. The tracks with $t_1 = 0$ and $t_3 = t(6$ mm), which is obtained now, gives t(3 mm) on the second plane, since such tracks are as shown in Figure 3.14(b). Iterating these methods, t(1.5 mm), t(3 mm), t(4.5 mm), t(5.25 mm), and t(6 mm) are obtained successively. As shown in Figure 3.15, t(X) obtained by the iteration method shows deviations from that defined as the inverse of X(t) given by eq.(3.6) at the region with $X > 4.5$ mm But X(t) with $X > 4.5$ mm can be deduced from the field strength map (Figure 3.3(a)) and W - E relation (Figure 3.13). Corrected X(t) is as follows.

$$X(\text{t nsec}) = \begin{cases} -6.48 \cdot t^2 + 3.97 \cdot t + 0.03 \text{ (mm)} & \text{(mm, 0 mm} \leq X \leq \text{4.5 mm)} \\ 32.32 \cdot t^2 - 8.08 \cdot t + 0.93 \text{ (mm)} & \text{(mm, 4.5 mm} \leq X \text{)} \end{cases} \tag{3.9}$$

As shown in Figure 3.16, t(X) obtained as the inverse of eq.(3.9) is quite in good agreement with t(X) obtained by the iteration. This fact gurrantees the reliabilities of X(t) (eq.(3.9)) and the W - E relation given in Figure 3.13.

Same consideration has been also carried for cosmic rays with incident angle of $\theta = 45°$, and the validity of X(t) given by eq.(3.9) has been checked.

Figure 3.17 is the equi- drift time map obtained from the field map (Figure 3.3) and the W - E relation (Figure 3.13).

ii) Spatial resolution

The "intrinsic" spatial resolution of the DC itself was measured by using cosmic rays. Figure 3.18 is the drift time distribution at the second layer for cosmic rays passing through the region with X = 3 ± 0.15 mm on both the first and the third planes. This distribution has a peak at t = 100 nsec, which corresponds to X = 3 mm, and its width can be considered to be the superposition of the spatial resolutions of three layers. It can be assumed that cosmic rays enter these three layers of DC almost perpendicularly, and that these three layers have the same spatial resolution at X = 3 mm. Then the spatial resolution of each layer at 3 mm drift length can be determined so as to reconstruct the shape of the peak in Figure 3.18 with the aid of Monte Carlo simulation. The optimal value of the spatial resolution at X = 3mm is obtained as $\sigma = 290\ \mu$m.

3-4. Reconstruction of trajectry and vertex

The trajectry of the β ray is reconstructed from the measured drift times t_i as follows. Here the indice i stands for the order of the fired cells.

1) The drift length X_i is derived from t_i by using eq.(3.9)
2) An i-th circle C_i with the radius X_i and the center at the i-th anode is drawn for all i = 1,2,...,n.
3) The track is drawn as such a smooth line that is tangential to all these circles C_i.

Actually, in case that the energy of the β ray is small, the trajectry is easily bent by multiple scattering and its reconstruction becomes quite difficult. Following two methods were tried for Monte Carlo simulation.

Method (A): The vertex point is obtained as the intersecting point of the source plane and the reconstructed trajectry.

Method (B): The vertex point is decided as the point where the extension of the fitted line from the first and the second cell crosses the source plane.

The deviations δ of the reconstructed vertex points obtained by the method (A) from the true points and those by the method (B) are as shown in Figure 3.19 (a) and (b), respectively. The vertex resolution Δ is defined as that the area of the spectrum within $\delta = 0$ and $\delta = \Delta$ amounts to 90 % of the total yield. The vertex resolution Δ was obtained as a function of the β ray energy (E_β) for β rays entering with the angle of $\theta = 30°$ was obtained as shown in Figure 3.20 (a), where θ_β is the angle of the β ray with respect to the normal of the source plane. The method (A) seems to give better resolution than the method (B), especially for the β ray with energy more than 800 keV. Figure 3.20 (b) shows Δ in case that the β rays were emitted with $\theta = 60°$. In this case, method (B) becomes better for smaller E_β. These facts can be explained as follows. In case of small E_β and large θ, the deviation Δ is caused by the multiple scattering between the source plane and the first layer, and informations from the second and the third layers do nothing but adding extra errors. In case that E_β is large and/or θ is small, Δ is mainly due to the intrinsic spatial resolutions of each layers. Therefore, it is neccessary to use these two methods depending on E_β and θ. $\Delta_X = 6$ mm (90 % C.L.) was achieved as the vertex resolution for X direction, and $\Delta_Y = 10$ mm for Y direction. Note that the first layer, being 32 mm apart from the source plane, measures the X direction, and the second layer being 44 mm apart from the source plane does the Y direction. Thus Δ_X is better than Δ_Y.

Chapter 4. Performance of ELEGANTS V

4-1. Test run at Osaka University

A measurement was made to test the performance and the operation of ELEGANTS V. This measurement was carried at Osaka, the sea- level laboratry, for about 3 hours. 6 μm thick Aluminized Mylar films was used as a dummy source. There was no shield. Radon gas, which is the radioactive gas contained in the air was not purged out. Trigger of the data aquisition was made whenever at least one PL fires, i.e. whenever signals from both ends of one PL module come in coincidence. The trigger rate was about 1100 counts per second, and the live time was about 2000 seconds.

4-2. Event selection

Histgram (a) in Figure 4.1 shows the energy sum spectrum of all PLs in case that at least one PL fires. It is the energy spectrum of raw data without any further requirements. Compton edges of ^{40}K and ^{208}Tl can be found. There are bumps around $3 \sim 5$ MeV and $5 \sim 10$ MeV, which are considered to be mainly due to cosmic rays as explained below.

The true $\beta\beta$ event has to satisefy following conditions;

Condition A : Two PL modules are fired. Here cases that two β rays hit one PL module and that two β rays hit three or more PL modules by back scattering are neglected for simplicity.

Condition B : There is no γ ray signals from NaI modules for the $0^+ \rightarrow 0^+$ $\beta\beta$ transition, and there is one signal of 0.54 or 1.36 MeV γ ray for the $0^+ \rightarrow 2^+$ $\beta\beta$ transition.

Condition C : There are only two tracks with the vertex point on the source plane.

The histgram (b) in Figure 4.1 is obtained from the histgram (a) by requiring condition A. Yields in the energy region below 5 MeV, which are due to Compton scatterings and low energy γ rays and the bump with lower energy are reduced to about 1/10. The bump at the higher energy region, however, still remains. The higher energy bump above 5 MeV is considered to be due to cosmic muons passing through one top PL and another bottom PL, since the energy loss just correspond to such high energy particles with the minimum ionization and their tracks are almost straight, i.e.

the external angle of the two tracks at the vertex point is almost 180°.

Now let's discuss the background events with two PL modules are fired. There are four types of the backgrounds, γ(BG), $\beta\gamma$(PL), and $\beta\gamma$(source), as discribed below.

1) γ(BG) : The backgrounds due to single γ rays.
  - γ(BG:a): Compton electron scattered at one PL, reaching another PL through the source plane, as shown in Figure 4.2 (a).
  - γ(BG:b): Photo electron produced at one PL, reaching another PL through the source plane, as shown in Figure 4.2 (b).
  - γ(BG:c): Successive interaction of a single γ ray with two PLs, as shown in Figure 4.2 (c).
  - γ(BG:d): Compton scattering on the source plane, where the Compton electron hits one PL and the scattered γ ray hit another PL, as shown in Figure 4.2 (d).
  - γ(BG:e): Successive interaction of a single γ ray in the source film, as shown in Figure 4.2 (e), such as including Compton + photo electric, double Compton, Compton + Møller, and photo electric + Møller processes.

2) $\beta\gamma$(PL) : The backgrounds due to β activities followed by γ rays or internal conversion electrons, which are located around PL.
  - $\beta\gamma$(PL:a): β ray, being emitted from β activities between PL and DC, hits one PL, and the successive γ ray makes Compton scattering at another PL, as shown in Figure 4.3 (a).
  - $\beta\gamma$(PL:b): β ray, being emitted from β activities between PL and DC, hits one PL, and the successive γ ray makes photo effect at another PL, as shown in Figure 4.3 (b).
  - $\beta\gamma$(PL:c): β ray, being emitted from β activities in PL or from those between PL and DC, hits one PL, and the successive conversion electron hits another, as shown in Figure 4.3 (c).
  - $\beta\gamma$(PL:d): β ray, being emitted from β activities in PL or from those between PL and NaI, hits one PL, and the successive γ ray makes Compton scattering at another PL, as shown in Figure 4.3 (d).
  - $\beta\gamma$(PL:e): β ray, emitted from β activities in PL or from those between PL and NaI, hits one PL, and the successive γ ray makes photo effect at another PL, as shown in Figure 4.3 (e).
  - $\beta\gamma$(PL:f): β ray, emitted from β activity outside PL, hits one PL, and the

successive γ ray makes Compton or photo electron at another PL, as shown in Figure 4.3 (f).

3) $\beta\gamma$(source): The backgrounds due to β activities with successive γ decay in the source film.
   - $\beta\gamma$(source:a): β ray emission and γ ray emission as shown in Figure 4.4 (a).
   - $\beta\gamma$(source:b): β ray emission and photo electric effect of the γ ray as shown in Figure 4.4 (b).
   - $\beta\gamma$(source:c): β ray emission and Compton scattering of the γ ray as shown in Figure 4.4 (c).
   - $\beta\gamma$(source:d): β ray emission and internal conversion electron of the γ ray as shown in Figure 4.4 (d).

4) μ(BG): The background due to cosmic rays.
   - μ(BG:a): Energetic cosmic rays (mainly muons) passing through upper and lower PLs as shown in Figure 4.5 (a).
   - μ(BG:b): Photo or Compton electrons associated with energetic γ rays and β rays following muon induced nuclear reactions as shown in Figure 4.5 (b).

Most of the background events γ(BG), $\beta\gamma$(PL), and $\beta\gamma$(source) involving the Compton scattering and μ(BG) are rejected by requiring condition B, since NaI modules are fired by scattered γ rays or cosmic muons passing through them.
On the other hand, it is difficult to reject such γ(BG), $\beta\gamma$(PL), $\beta\gamma$(source) that involve photo electrons, internal conversion electrons, or Compton scattered γ rays escaping through the side walls of DC, because they give no veto signal from NaI.
The sum energy spectrum vetoed by the signals from the NaI modules is shown by the histgram (c) in Figure 4.1. Yields due to Compton scattering are reduced by a factor 10 or so. Two broad peaks in the energy region beyond 3 MeV, which are considered to be due to μ(BG), disappear in the histgram (c).

Most of the background events γ(BG:c), γ(BG:d), $\beta\gamma$(PL:f), and $\beta\gamma$(source:a) are rejected by requiring the condition C, because they do not have two electron trajectries. Some of γ(BG:e), $\beta\gamma$(source:b), and $\beta\gamma$(source:c) can be eliminated by examining the vertex point on the source plane. Most of the events with sum energies more than 3 MeV are considered to be due to cosmic muons passing through small gaps between the NaI modules. The residual backgrounds with the sum energies below 3 MeV are mainly due to such γ(BG:a) that the Compton scattered γ rays escape through the side walls of DC, resulting in no veto signals from the NaI modules, as shown in Figure 4.6. Such events become quite serious backgrounds especially for $2\nu\beta\beta$, because they can hardly be distinguished from the true $\beta\beta$ events.

As given in Table 4.1, the rejection efficiencies with the condition A, B, and C are 99.8 % for the backgrounds due to external γ rays, and 99.99 % or better for cosmic rays.

4-3. Sensitivity for the $\beta\beta$ decay

(1) Sensitivity for $0\nu\beta\beta$

As discussed in Chapter 2, the sensitivity for the $\beta\beta$ decay is limited by the background level. Figure 4.7 is the sum energy spectrum of the two β rays for the $0\nu\beta\beta$ $0^+ \rightarrow 0^+$ transition induced by the mass term $<m_\nu>$ in eq.(1.2), which is caluculated by the Monte Carlo method. Setting the energy threshold at 2.5 MeV, the detection efficiency for $0\nu\beta\beta$ amounts to 54 %. Because of the Q value, possible origins of the background is limited to ^{214}Bi and ^{208}Tl. Neutron capture induced by cosmic muon is expected to be sufficientry suppressed at the Kamioka underground laboratry. The amount of the background can be evaluated as follows;

(1) ^{214}Bi

The decay scheme of the ^{214}Bi is shown in Figure 3.1. The backgrounds due to ^{214}Bi can be classified into following types.

i) BG-Bi(source) (Figure 4.8(a))

If the source film is contaminated by ^{214}Bi, they make backgrounds via the processes of $\beta\gamma$(source:a) and $\beta\gamma$(source:b). In case that the γ ray following ^{214}Bi β decay escapes through the side walls of DC or through the NaI modules, $\beta\gamma$(source:c) also contributes to the backgrounds. These processes can be eliminated by detecting the delayed α ray emitted from ^{214}Po with 164 μsec half life. It was found by the Monte Carlo simulation that 45 % of delayed α rays can come out of the source plane. The detection efficiency of DC for α particles is about 85 % as mentioned in Chapter 3. Then reduction efficiency by detecting the delayed α ray becomes $\sim$ 38 %. The time window for coincidence should be taken as a few msec so as to accept the delayed α rays from most of ^{214}Po. Here the effect of the accidental coincidence with other background signals is negligible, because the counting rate is only 0.1 cps for the backgrounds in the high energy region of the α ray.

The BG-Bi backgrounds associated with the internal conversion electron can be reduced also by detecting the K-X ray following the internal conversion. The overall efficiency of the NaI modules for the K-X ray produced at the source plane is 48 %. Finally, 68 % of the BG-Bi(source) background is expected to be rejected by DC and NaI.

ii) BG-Bi(PL-a) (Figure 4.8(b)) If PL contains ^{214}Bi, β ray feeding the ground state gives the background event as shown in Figure 4.6. 95 % of them can be rejected by detecting the delayed α ray with PL. It should be noted that the single β ray hits first one PL, and goes through the source plane to another PL. The time difference $\Delta t = t_2 - t_1$ between the timing signals t_1, and t_2, from these two PL's, correspond to the flight time of the β ray between the two PL's, is larger than that for the $\beta\beta$ rays emitted from the source plane. Thus proper selection (TOF cut) of the time window in the TOF (Δt) spectrum rejects 90 % of the backgrounds due to the sigle β decay. Proper selection (θ cut, see Figure 4.9) of the bending angle larger than 30° reduce furthermore 80 % of the backgrounds due to the single β ray because such β ray does not bend much at the source plane. Figure 4.10 shows the result of the Monte Carlo simulation for the distribution of the bending angle for single β rays with $E_\beta > 1$ MeV passing through the source plane. More than 80 % of the β rays have bending angles less than 30 °, as shown in Figure 4.10. On the other hand, such θ cut loses only $\sim$ 5 % of the true $\beta\beta$ events, since two β rays from $0\nu\beta\beta$ are widely spreaded in the bending angle, θ.

iii) BG-Bi(PL-b) (Figure 4.8(c)): ^{214}Bi around or in PL can make backgrounds $\beta\gamma$(PL:b, c, e). If the scattered γ ray escapes, $\beta\gamma$(PL:a, d) also contributes to the backgrounds. In these cases, main origin of ^{214}Bi is ^{222}Rn in the air. Thus circulation of the pure N_2 gas is most effective. The delayed α ray is hardly detected, because it may not enter DC. The TOF cut by Δt from the two PLs is effective. The θ cut on the bending angle may become not so effective because the photo- or Compton- electron has small energy and is easily bent in the source plane.

(2) ^{208}Tl

As shown in Figure 4.11, the β decay of ^{208}Tl is followed by the 2614.5 keV γ ray, and sometimes one or two γ rays. The backgrounds due to ^{208}Tl become serious because of its large Q value ($Q_{\beta\beta}$ = 4.99 MeV). There are following types of the backgrounds.

i) BG-Tl(source-a) (Figure 4.12(a))

^{208}Tl in the source film gives backgrounds via the same process as BG-Bi(source). Although the daughter nucleus of ^{208}Tl does not make α decay as that of ^{214}Bi, but the β decay of ^{208}Tl is accompanied by 2 $\sim$ 4 γ rays (see Figure 4.11). Then the backgrounds of this type can be rejected by observing these γ ray by NaI, and the K-X ray in case that one of the γ rays are internally converted.

ii) BG-Tl(source-b) (Figure 4.12(b)): $\beta\gamma$(source:c) due to ^{208}Tl also contributes to the background. It is reduced to 1/20 by detecting γ rays by NaI, and to 1/5 by checking the vertex point.

iii) BG-Tl(PL): ^{208}Tl in or around PL can make backgrounds of the type $\beta\gamma$(PL) (Figure 4.3). Anti-coincidence by NaI for the 583 keV γ ray or the Compton-scattered γ ray, the TOF cut, and the θ cut can reduce them.

Assumig that the amount of the U-chain and Th-chain isotopes in the source film and in PL are less than 0.5 ppb, and that ^{222}Rn is almost completely purged out, the numbers of the background events in one year measurement are cluculated by the Monte Carlo simulation, as given in Table 4.2. They are 2.2 counts for BG-Bi(source), 270 counts for BG-Bi(PL-a), 0.9 counts for BG-Tl(source-a), 1.3 counts for BG-Tl(source-b), and 300 counts for BG-Tl(PL). Applying the reduction techniques as described above, they turn out to 0.7, 0.3, 0.1, 0.02, 0.3, 0.2, respectively, and the total number is 1.6 counts. As mentioned in Chapter 2-2, the limit of the observation is given by the following condition.

$$N_{0\nu\beta\beta} > \delta N_{BG}, \tag{4.1}$$

where

$$N_{0\nu\beta\beta} = N_o \cdot k(0\nu) \cdot \log 2 \cdot t / T^{0\nu}_{\beta\beta} \tag{4.2}$$

In case that the observed number of the background is 1.6 counts, the expected value of δN_{BG} with 68 % C.L. is 2.3 counts. The detection efficiency k(0ν) is estimated as 54 %. Then one year (t = 1) measurement with 200 g of ^{100}Mo ($N_o = 1.2 \times 10^{24}$) allows one to observe $0\nu\beta\beta$ in the region with $T^{\beta\beta}_{1/2} = 2 \times 10^{23}$ years.

(2) Sensitivity for $2\nu\beta\beta$

As for $2\nu\beta\beta$, it is rather difficult to estimate N_{BG}, since there are many possible origins of the background. Using the background rate measured n_{BG} at Osaka University, the sensitivity of the ELEGANTS V at the sea level laboratory without shields for γ rays and cosmic rays can be derived from;

$$N_{2\nu\beta\beta} > \delta N_{BG}, \tag{4.3}$$

where

$$N_{2\nu\beta\beta} = N_o{\cdot}k(2\nu){\cdot}\log 2 \cdot t/T^{2\nu}_{\beta\beta}, \tag{4.4}$$

Defining the $2\nu\beta\beta$ energy region as the region where the sum energy of the two β rays is in between 0.7 MeV and 1.5 MeV, $k(2\nu)$ is estimated as 18.9 %. As given in Table 4.2, the background rate at the $2\nu\beta\beta$ region is 0.5 counts/keV·hour. In this case, δN_{BG} is nearly equal to $\sqrt{N_{BG}}$. Then $T^{2\nu}_{\beta\beta} \sim 10^{20}$ is expected as the observation limit of the $2\nu\beta\beta$ half life even with 1 year measurement without shields against γ rays and cosmic rays.

Chapter 5. Development of the Mo source film

5-1. Purification of the Mo powder

Radioactive U and Th chain isotopes in the source film produce the most serious backgrounds in the $\beta\beta$ measurement. As discussed in Chapter 4, amount of U and Th isotopes should be reduced to less than 0.5 ppb in order to observe long half life $\beta\beta$ decays in the region of $T^{0\nu}_{1/2}(\ ^{100}\mathrm{Mo}\ ) > 10^{23}$ years. ^{100}Mo powder was provided by Oak Ridge National Laboratory. ^{100}Mo metallic foils, however, provided by ORNL were found to be contaminated by 10 $\sim$ 100 ppb U and Th chain isotopes in the previous measurement with ELEGANTS IV. Both the ^{100}Mo powder and natural Mo powder have been purified by using the same chemical process at Nippon Mining Co., Ltd (Ref. 1.11). The contents of U and Th have been checked by Nippon Mining by the inductively coupled plasma mass separation method. The contents in both the purified ^{100}Mo powders and natural the Mo powder are less than 0.5 ppb for U and Th, and 1.2 ppm for K, respectively.

5-2. Construction of the source film

The Mo source is divided into four sections as shown in Figure 5.1. Two of them are the ^{100}Mo source, and other two are the natural Mo source. Each section consists of 8 films, each with 20 mg/cm^2 in thickness and 18 cm × 18 cm in area. The ^{100}Mo and the natural Mo source films were made by using the same process as follows.

1) Grinding the purified powder into fine powder.
2) Mixing with solution of Formvar: 7.60 g of molybdenum, 1.00 g of Formvar, 42 ml of cyclohexanone, and 18 ml of chloroform are used for each piece of the film.
3) Pouring into the mold, which is made of pylex glass. Inner area of the mold is 19 cm × 19 cm area. It was kept holizontally within 4×10^{-4} radian. 5.7 μm thick Mylar film was used as the backing of the source.
4) Drying up. : The solvents were evapolated by using infrared ray lamps for 6 hours.
5) Cutting. : The margin of 5mm width were cut away to avoid the imhomogeneous of source.
6) Measurement of the final masses and the areas of each films (see Table 5.1).

Table 5.2 shows amounts of U, Th, and K in each material used and in each film. U and Th are less than 0.5 ppb, but 2.2 ppm of K is contained in the Mo source film. This potasium comes from Formvar, Mylar, and the original Mo powder, because it agree with the expected amount of 2.4 ppm from the potasium contaminants in the materials used.

16 films with ^{100}Mo and 16 with natural Mo were prepared. Mass, area, and thickness of each films are as shown in Table 5.1.

5-3. Installation in ELEGANTS V

The Mo films were mounted in the source holder made of 3 mm thick stainless steel. Two films of the same type of molybdenum are folded to get the uniform source with the effective thickness of about 40 mg/cm^2. The source plane is divided into four sections as shown in Figure 5.1. Each section consists of four setsof the two fold films. These films are interlieved between 12 μm thick Mylar foils, and the air inside has been pumped out. Total mean thicknesses are 40.2 ± 0.05 g/cm^2 for natural Mo and 40.5 ± 0.1 g/cm^2 for ^{100}Mo. Thickness of the other materials like Mylar films is amounts to 8.5 mg/cm^2. The source assembly has been inserted between two track chambers, and pure N_2 gas is introduced to exhaust radon gas. Cross sectional view around the source plane is as Figure 5.2.

Chapter 6. Background measurement at Kamioka

6-1. Experimental set up

The background run with ELEGANTS V has been carried out by using OFHC foils as a dummy source at the Kamioka underground laboratory. All detectors, data aquisition systems, and heavy shields used in the background measurement are the same as those in the ^{100}Mo measurement. The dummy source consists of two-fold foils, each with 70 cm × 70 cm in area and 36 mg/cm^2 in thickness. The U and Th contaminations in the OFHC foils have been checked to be less than 0.5 ppb. N_2 gas circulation has been gradually improved during the run.

6-2. Measurements

Measurements were carried out from 9 Aug. 1989 to 21 Nov. 1989 to check the whole counter system and the data taking system, to caliblate detectors, and to examine the backgrounds. These runs can be divided into following three types.

RUN-A series : This series is mainly for a tune-up of the detectors, but RUN-A03, A04, and A05 are the first complete measurements of the background events.

RUN-B series : Some improvements or changes were made in this series by taking into account the result of the RUN-A series.

RUN-C series : This series was focused on the survey of the background events and dependence of the background rate on the N_2 gas circulation.

6-3. Results and analysis

Followings are the data of RUN-A05.

RUN-A05 ;
trigger rate : 220 counts per sec.
live time : 10243 seconds.
total events : 2252882 events.

Figure 6.1 (a) shows the sum energy spectrum of β rays in this run. The background rate of ELEGANTS V is obtained at various cuts (conditions) as mentioned in Chapter 4-2 of part I. In case of the $0\nu\beta\beta$ $0^+ \rightarrow 0^+$ transition, following conditions are required.

Cut-1 : Coincidence of two PLs.
Cut-2 : Anti-coincidence with NaI.
Cut-3 : Coincidence of more than 5 out of 6 DC planes for every signals of PLs.
Cut-4 : Consistency of the trajectries and the vertex point in the hit pattern.

Figure 6.1 (b) (c) are the sum energy spectra of two β rays after Cut-1 and 2, respectively. Figure 6.1.(d) shows the sum energy spectra obtained by Cut-3, i.e. requiring the condition that at least 5 of 6 DC planes are fired in coincidence. Operating Cut-4, 22 events remained finally in 0ν region where the sum energy of two β rays are more than 2.5 MeV. The number of the events leads to 2×10^{-3} counts per second (cps) for the background rate.

6-4. Origin of the background

There are three key points to find the origins of the residual backgrounds.

1) Compton edges correspond to 609 keV and 1120 keV γ rays can be found in Figure 6.1. These γ rays are emitted from excited states of ^{214}Po, the daughter nucleus of ^{214}Bi.
2) The end point of the spectrum after Cut-3 is about 3.3 MeV. It corresponds to the Q value of the ^{214}Bi β decay.
3) As shown in Figure 6.2, there are photo peaks due to the successive β and γ decay of ^{214}Pb and ^{214}Bi. No peaks corresponding to others can be found.

Therefore, the most probable candidates for these backgrounds are the successive β and γ decay of ^{214}Pb and ^{214}Bi. ^{214}Bi with $Q_\beta \simeq 3.27$ MeV feeds mostly levels below 2.2 MeV, and thus the following γ rays have energies less than 2.2 MeV. Therefore single γ rays following ^{214}Bi hardly contribute to the backgrounds in the $0\nu\beta\beta$ region of E_{sum} = 2.5 MeV ~ 3.0 MeV. Consequently the β ray from ^{214}Bi must hit one PL to make E_{sum} in the $0\nu\beta\beta$ region. Then possible places of ^{214}Pb and ^{214}Bi are limited to inside or vicinity of PLs.

One of the major source of ^{214}Pb and ^{214}Bi is ^{222}Rn in the air. The gap between PL and NaI is as large as 25 mm, and the total volume of the air in the gaps are 50 litter. Assuming ^{214}Pb and ^{214}Bi are decay products of ^{222}Rn in the air near PL, amounts of them are estimated from the yield of the γ ray photo peaks in NaI as follows.

$$\mathrm{N(photo\ peak)} = \mathrm{R}_{decay} \times \mathrm{BR} \times \varepsilon_\beta \times \Omega_\beta \times \varepsilon_\gamma(\mathrm{peak}) \times \Omega_\gamma \times \mathrm{t}, \tag{6.1}$$

where N(photo peak) is the yield at the photo peak after subtraction of the continuum background, R_{decay} is the decay rate of the nuclei, ^{214}Pb and ^{214}Bi, in this case. BR is the branching ratio. ε_β, ε_γ(peak), Ω_β, and Ω_γ stand for the detection efficiency of the β ray, that of the γ ray photo peak, the acceptance of the PL β counter and that of the NaI γ counter, respectively. Ω_β and Ω_γ are obtained to be about 0.5 and 0.75, respectively, from the Monte Carlo caluculation. ε_β can be set to be one. t means the measurement time. It is t = 10243 seconds in case of RUN-A05.
For the 353 keV γ rays following the ^{214}Pb β decay, N(photo peak) is 4.1×10^4 counts, ε_γ(peak) is about 0.45 , and BR is 0.37. Thus R_{decay} is 60 $\sim$ 70 decays per second (dps). For the 609 keV γ ray, N(photo peak) is 3.5×10^4 counts, BR equals to 0.47, ε_γ(peak) is about 0.25, and R_{decay} is obtained as $\sim$ 75 dps. This is consistent with R_{decay} for ^{214}Pb provided that ^{214}Pb and ^{214}Bi are in radiative balance.

To check the effect of ^{222}Rn in the air on the background, RUN-C15 was carried out by increasing the circulation rate of N_2 gas.

RUN-C15;
trigger rate : 39 cps.
live time : 126212 seconds.
total events : 4096968 events.

The counting rate after Cut 4 for the background in the $0\nu\beta\beta$ region of $E_{\beta1+\beta2}$ = 2.5 $\sim$ 3 MeV is found to be 3×10^{-4} cps. This counting rate is about 6 times improved comparing with that of RUN-A05.

These are summarized as follows.

1) The main component of the background is due to ^{214}Pb and ^{214}Bi.
2) Since the amount of the background due to ^{214}Bi is much reduced by increasing the N_2 gas circulation rate, the origin of these ^{214}Pb and ^{214}Bi is attributed to ^{222}Rn in the air.
3) These isotopes are considered to stay between PL and NaI or PL and DC.
4) No other compornent of the background has been found.

Consequently, it is quite important to reject ^{222}Rn between PL and NaI or NaI and DC.

Chapter 7. Experimental studies for ^{100}Mo $\beta\beta$ decay

7-1. Run with enriched ^{100}Mo and natural Mo sources

Following changes were carried out after the background measurement with the OFHC dummy source.

1) The vertex chamber with the OFHC source foils has been replaced by the Mo source assembly. The OFHC source foils were set on the two planes, one on the top face, and another on the bottom face of the vertex chamber. Tracks of the β rays emitted from one source plane would be bent at another source plane. Then it would be difficult to determine the vertex point from the tracks in the tracking chambers only. The vertex chamber was found to have no sufficient efficiency to determine the vertex point. Thus two source planes have been combined into one plane. It becomes much easier to observe the vertex point, and also to install or exchange the source assembly.
2) Air bags have been inserted between NaI and PL. The space around the source assembly have been kept airtight. Pure N_2 gas has been introduced into them to reject radon gas more completely.

RUN-D series with 100 g of ^{100}Mo and 100 g of natural Mo has started at Dec. 1989.

7-2. Analysis

(1) Event selection

The first run with ^{100}Mo, RUN-D01, was carried out with following conditions.

RUN-D01;
Trigger rate : 19.0 cps.
Number of the acquired events : 4329808 events.
Live time : 258288 seconds.
Dead time : 13.4 %.

Acquired events were discriminated by cuts 1 $\sim$ 4 defined in Chapter 6.1, i.e.

Cut-1 : Signals from only two PLs in coincidence is required. The discrimination level of the energy is 150 keV.

Cut-2 : No signals from NaIs in coincidence with the PL signals is required. The discrimination level of the energy is 40 keV. It is possible to detect the 80 keV K-X ray of ^{214}Po, the daughter nucleus of ^{214}Bi, which makes fatal backgrounds for $\beta\beta$ decays.

Cut-3 : Signals from 5 or 6 out of 6 DC planes in coincidence with signals from PL.

Cut-4 : Two trajectries and one vertex point.

Table 7.1 gives the numbers of the residual events after each cut.

(2) Origin of the backgrounds for $0\nu\beta\beta$

Figure 7.1 shows the energy spectrum obtained from the raw data. Compton edges of 609 keV γ rays and 1.12 MeV γ rays due to ^{214}Bi are seen. As shown in Figure 7.2, the γ rays of ^{214}Pb and ^{214}Bi, and no other γ rays are seen in the NaI spectrum. The decay rate of ^{214}Bi is estimated as 0.42 dps from the counting rate of the photo peak of 609 keV γ ray. As for the counting rate in the $0\nu\beta\beta$ region, i.e. the region with the sum energy of the β rays more than 2.5 MeV, is (6.3 ± 1.7) $\times 10^{-5}$ cps. Figure 7.3 shows the background rates in the $0\nu\beta\beta$ region of RUN-A05, RUN-C15, and RUN-D01 as a function of the trigger rate. The background rate roughly shows linear dependense on the trigger rate. The trigger rate has been shown to be reduced to 17 cps by introducing intense N_2 gas to purge out the radon gas. In this case one may expect that almost all counts of the background are rejected.

7-3. Results for the neutrinoless $\beta\beta$ decay of ^{100}Mo

(1) Event selection in the $0\nu\beta\beta$ region

32 events are remaining after Cut-3 in the region of $0\nu\beta\beta$ with $E_\beta > 2.5$ MeV. Further reduction by examining the tracks and the vertex points were carried out. 14 events do not have complete tracks or vertex. There are 9 events which seem to have vertex points on the ^{100}Mo source films, and 4 events of them have bending angles smaller than 30°. There are 9 events which seem to have vertex points on the natural Mo films. 4 of them have bending angles smaller than 30°.

(2) Limit on the half life of $0\nu\beta\beta$

The number of true events N(true) and its statistical fluctuation m(true) are expressed as follows.

$$N(\text{true}) = N(100) - N(\text{nat}), \qquad (7.1.a)$$

$$\mathrm{m(true)} = \sqrt{\mathrm{m(100)}^2 + \mathrm{m(nat)}^2}. \qquad (7.1.b)$$

Here N(100) and N(nat) stand for the numbers of the observed events with the vertices on the ^{100}Mo films and the natural Mo films, respectively. m(100) and m(nat) are the statistical fluctuations of N(100) and N(nat), respectively. Assuming that N(100)and N(true) obey the Gaussian distributions, m(100) and m(nat) with 68 % of the confidential levels are simply expressed as follows.

$$\mathrm{m(100)} = \sqrt{\mathrm{N(100)}}, \qquad (7.2.a)$$

$$\mathrm{m(nat)} = \sqrt{\mathrm{N(nat)}}. \qquad (7.2.b)$$

From the result of the RUN-D01 without θ cut, they are as follows.

N(100) = 9, m(100) = 3

N(nat) = 9, m(nat) = 3

N(true) = 0, m(true) = 13

The half life of $0\nu\beta\beta$ $T^{0\nu}_{1/2}$ is deduced from N(true) by following equation.

$$T^{0\nu}_{1/2} = \ln 2 \times N_o \times k \times \, t/\mathrm{N(true)} \qquad (7.3)$$

Here N_o is the number of the $\beta\beta$ source nuclei, k is the detection efficiency, and t is the measurement time. In case of RUN-D01, $N_o = 5.4 \times 10^{23}$, $t = 2.6 \times 10^5$ seconds, and k = 0.36 taking the efficiency of DC into account. The upper limits on $T^{0\nu}_{1/2}$ is obtained as

$$T^{0\nu}_{1/2} > 7.6 \times 10^{19} \text{ years (68 \% C.L.).} \qquad (7.4)$$

Requiring the θ cut, N and m are obtained as follows.

N(100) = 5, m(100) = 2.2

N(nat) = 5, m(nat) = 2.2

N(true) = 0, m(true) = 7.1.

Thus one sets $T^{0\nu}_{1/2} > 1.4 \times 10^{20}$ years (68 % C.L.) (7.5)

as a lower limit on the half life of $0\nu\beta\beta$.

Concluding remarks

(1) An ultra low background and high sensitivity rare decay detector 'ELEGANTS V' has been developed. Since it is separated from the $\beta\beta$ source, it can be used to study many kinds of the $\beta\beta$ source nuclei with large amount, about $10^{23} \sim 10^{24}$ nuclei. It consists of three types of detectors, drift chambers for β ray tracks, plastic scintillators for energy and timing of β rays, and NaI scintillators for γ rays and X rays. All the signals from these detectors are properly used for on-line and off-line event selections (cuts) and for evaluation of the background events, which are very crucial for selecting true signals and for rejecting background ones. The drift chambers, which is unique of ELEGANTS V, is the key detector for selecting true events from the background events by analyzing the two β ray tracks and its vertex point.

(2) The drift chamber system has been developed on the basis of new ideas. The chambers are made of selected materials with extremely small amounts of radioactive contaminations. They have the very large acceptance of $\Omega \sim 3.2\pi$. Trajectries of the electrons and other chaged particles can be obtained, being independent of the incoming direction by virtue of the cylindrical electric field. Each plane of the track chamber has the detection effitiency of $\varepsilon \geq 98.5$ % and the spatial resolution of 290 μm with 68 % C.L. The vertex point resolution on the source plane is typically 12 mm × 20mm (90 % C.L.). These drift chambers are operated with the mixed gas of 85% He and 15 %CO_2. Such mixture enables one the safe operation in the closed underground laboratory and very small effect of the multiple scattering on low energy β rays.

(3) The energy resolution of the plastic scintillators is 250 keV (FWHM) for electrons in the $0\nu\beta\beta$ region of $E_\beta = 2.5 \sim 3$ MeV. The time resolution is 700 psec(FWHM) for the 1.5 MeV β ray. As for NaI scintillators, 7.7 % FWHM energy resolution is achieved for ^{137}Cs 662 keV γ ray. The plastic and the NaI scintillators cover large solid angles of $\Omega_\beta = 3.4\ \pi$ and $\Omega_\gamma = 3.2\ \pi$, respectively.

(4) The total performance of ELEGANTS V has been studied at the Osaka university sea level laboratory, without source films. Heavy metal shields for external γ backgrounds and N_2 gas circulation for removing Rn gas in the air were also not used. The backgrounds are reduced by using properly all kinds of data from the three types of detectors. The sensitivities for $0\nu\beta\beta$ and $2\nu\beta\beta$ events, which correspond to the upper limits on the half lives to be measured, are evaluated on the basis of the observed data. They are $T_{1/2}^{0\nu\beta\beta} > 2 \times 10^{23}$ years for $0\nu\beta\beta$, and $T_{1/2}^{2\nu\beta\beta} > 10^{20}$ years for $2\nu\beta\beta$ for one year measurement with 200 g of ^{100}Mo. Thus ELEGANTS V may be used to study a new region of the $\beta\beta$ decay or other rare decay physics.

(5) Clean ^{100}Mo and natural Mo source films have been developed. The source plane consists of 16- ^{100}Mo films and 16- natural Mo films. Each film is 180 mm × 180 mm × 20 mg/cm^2. Each set of the Mo source is 360 mm × 360 mm × 40 mg/cm^2. The amounts of U and Th isotopes, which are most serious background sources, are found to be less than 0.5 ppb.

(6) Measurements were carried out to examine the background level and the sensitivity of the detector system. The origin of the background events in the $0\nu\beta\beta$ region is mainly attributed to ^{214}Bi around the plastic scintillators. ^{214}Bi has the Q value of 3.27 MeV, and its β decay followed by γ rays and/or internal conversion electrons make serious backgrounds in the $0\nu\beta\beta$ region, especially in case that Compton-scattered γ ray escapes through either the NaI scintillator modules or the side walls of the drift chambers. ^{214}Bi is provided by ^{222}Rn in the air around the plastic scintillators. The sensitivity around $\mathrm{T}_{1/2}^{0\nu\beta\beta} \sim 2 \times 10^{23}$ years, which is shown to be achieved by purging out the remaining Rn gas in the vicinity of the PL modules.

(7) The measurement with ^{100}Mo and natural Mo has been started. So far a very short run for a few days , with incomplete Rn gas rejection, leads to the lower limit on $\mathrm{T}_{1/2}^{0\nu\beta\beta}$ as

$$T_{1/2}^{0\nu\beta\beta}(\ 0^+ \rightarrow 0^+\ ) > 1.4 \times 10^{20} \text{ years (68 \% C.L.).}$$

It corresponds to the upper limit on the Majorana neutrino mass $<\mathrm{m}_\nu> < 15.4$ eV by using the matrix element given in Ref. 1.6. It compares with the previous data of

$$T_{1/2}^{0\nu\beta\beta}(\ 0^+ \rightarrow 0^+\ ) > 1.3 \times 10^{20} \text{ years (68 \% C.L.),}$$

obtained by ELEGANTS IV.

(8) The vertex chamber is found to have no sufficient efficiency plataeu and no full efficiency. This is due to the inadequate field strength. It has to be improved to get better vertex resolution and the efficiency for delayed α ray.

(9) It should be emphasized that ELEGANTS V shows very large sensitivity and high selectivity by virtue of the use of the combination of three different types of detectors. It is proved that looking at the differences of the features and the patterns between true events and background ones is the most powerful way to study rare decays.

Figure Captions

Chapter 1.

Fig. 1.1 Diagrams of the $\beta\beta$ decays with two nucleon mechanism.
(a); $2\nu\beta\beta$, (b); $0\nu\beta\beta$ with $<m_\nu>$, (c); $0\nu\beta\beta$ with V + A interaction, and (d); $0\nu B\beta\beta$.

Fig. 1.2 $\beta\beta$ decays with exotic mechanisms.
(a); $2\nu\beta\beta$ via δ isober, (b),(c); $0\nu\beta\beta$ via δ isober, (d); $0\nu\beta\beta$ with Higgs particles, (e), (f), (g), (h), (i); $\beta\beta$ decays with meson exchanges, and (j); $0\nu\beta\beta$ involving SUSY particles.

Chapter 2.

Fig. 2.1 Schematic drawings of ELEGANTS V. (a); top view. (b); side view.

Fig. 2.2 Top view (a) and side view (b) of the plastic scintillator and PM tubes.

Fig. 2.3 Schematic drawing of a pulse height spectrum showing the relation between shape of the Compton edge and the energy resolution for the plastic scintillator.

Fig. 2.4 Energy resolution of the type A plastic scintillator (open circle) and the type B plastic scintillator (closed circle) as functions of the electron energy.

Fig. 2.5 Energy resolution of the NaI scintillators for γ rays.

Fig. 2.6 The relation between roll-off ratio (R) and position (x)of the γ source along NaI crystal. R is difined as

$$R = (V_L - V_R)/(V_L + V_R) ,$$

where V_L and V_R stand for light outputs from PM tubes on both ends.

Chapter 3.

Fig. 3.1 Decay and level scheme of ^{214}Bi.

Fig. 3.2 Outline of the drift chamber, (a); top view and (b); side view. Vertex chamber is put between two track chambers. Plastic scintillators of type B are inserted as shown in the figure.

Fig. 3.3 Cross sectional view of the cell and equi-field map of the track chamber.

•, ×, and ◇ indicate anode, cathode, and field wire, respectively. High voltage is applied on the anode wire. Cathode and field wires are kept at the ground potential.

Fig. 3.4 Mis-tracking case in the uniform field type drift chamber. Drift electron via path (b) reachs anode wire before via path (a), and gives wrong drift time.

Fig. 3.5 Examples of the simulated trajectries in (a); Ar : $CO_2 = 85 : 15$ and (b); He : $CO_2 = 85 : 15$ mixtures. Four examples are given for each gases. The electrons are emitted from the source film with $E_\beta = 500$ keV and $\theta = 60°$.

Fig. 3.6 Set up for measurement of the detection efficiency of track chambers for cosmic rays.

Fig. 3.7 High voltage dependences of the efficiencies of the track chambers. (a); for the upper chamber, and (b); for the lower chamber.

Fig. 3.8 High voltage dependence of efficiency of the vertex chamber.

Fig. 3.9 Set up for measurement of the detection efficiency of the vertex chamber with the ^{241}Am α source.

Fig. 3.10 Pulse height spectra of the vertex chamber for (a) with α source, and (b) without α source.

Fig. 3.11 Position dependence of the detection efficiency for α particle.

Fig. 3.12 Two dementional plot of the drift times, t_1 and t_2 for the first and the second layer, (a); in case particles enter chamber plane perpendicularly, and (b); particles come in with 45 degree of angle against plane. t_1 stands for drift time given by the first and the third plane, and t_2 for the second.

Fig. 3.13 Drift velocity against the field strength for He : $CO_2 = 85 : 15$ mixture.

Fig. 3.14 Geometrical situation for the determination of t(x). • and ∘ denote anode wire and field wire. (a); t(6 mm), (b); t(3 mm), (c); t(4.5 mm), (d); t(1.5 mm), and (e); t(5.12 mm).

Fig. 3.15 Drift time t as a function of the position X for vertical track ($\theta = 0°$).

Fig. 3.16 Corrected drift time t as a function of the position X.

Fig. 3.17 Equi-drift time map of the track chamber.

Fig. 3.18 Drift time spectrum for particles passing through with 3mm of distance from the anode wire. Peaks except for major one are ghosts due to geometrical ambiguity.

Fig. 3.19 Spectra of the vertex reconstruction error δ with (a); method (A) and (b); method (B).

Fig. 3.20 Energy dependence of the vertex resolution Δ. (a); $\theta = 30°$. (b); $\theta = 60°$.

Chapter 4.

Fig. 4.1 Sum energy spectra of the β rays:
(a); No condition is required.
(b); Coinsidence of two plastic scintillator modules is required.
(c); The spectrum of the events vetoed by NaI scintillators.
(d); Coincidence of more than 5 of 6 DC layers is required.

Fig. 4.2 The backgrounds due to the single γ ray (γ(BG)).
(a); Compton electron scattered at one PL reaching another PL through the source plane.
(b); Photo electron produced at one PL reaching another PL through the source plane.
(c); Successive interaction of the single γ ray with two PLs.
(d); Compton electron produced at the source plane and scattered γ ray hit two PL modules in coincidence.
(e); Successive interaction of the single γ ray on the source plane (including Compton + photo electric, double Compton, Compton + Møller, photo electric + Møller processes).

Fig. 4.3 The backgrounds due to β γ emitter around PL ($\beta\gamma$(PL)).
(a); β ray emission between PL and DC followed by Compton scattering at PL.
(b); β ray emission between PL and DC followed by photo electric effect at PL.
(c); β ray emission between PL and DC followed by internal conversion.
(d); β ray emission between PL and NaI followed by Compton scattering at PL.
(e); β ray emission between PL and NaI followed by photo electric effect at PL.
(f); β ray emission outside one PL and Compton or photo electric effect at another PL.

Fig. 4.4 The backgrounds due to the β activities in the source film ($\beta\gamma$(source)).
(a); β ray emission followed by γ ray emission
(b); β ray emission followed by photo electric effect.
(c); β ray emission followed by Compton scattering.
(d); β ray emission followed by internal conversion.

Fig. 4.5 The backgrounds due to cosmic ray (μ(BG)).
(a); Energetic cosmic ray (mainly μ on) passing through upper and lower PLs.
(b); Energetic β ray or γ ray from the unstable nucleus produced by μ on induced neutron capture.

Fig. 4.6 The background by Compton scattering at PL. NaI veto has no effect when scattered γ ray escapes through DC walls.

Fig. 4.7 Spectrum of the sum energy of two β rays for $0\nu\beta\beta$ with $<m_\nu>$ caluculated by the Monte Carlo simulation.

(a); The case that two β rays are emitted to the opposite sides of each other.
(b); The case that two β rays are emitted to the same direction.
Fig. 4.8 The backgrounds for $0\nu\beta\beta$ due to ^{214}Bi:
(a); β ray emission and internal conversion by ^{214}Bi in the source film.
(b); Single β ray emission by ^{214}Bi in the plastic scintillators.
(c); β ray emission and internal conversion by ^{214}Bi between DC and PL.

Fig. 4.9 Cut on the bending angle (θ cut). 80 % of the background with a charged particle crossing over the source plane can be rejected, besides only 5 % of the efficiency for the true $\beta\beta$ events is lost.

Fig. 4.10 Distributions of the bending angle in case that the β ray perpendiculary enter the source plane with (a); 1 MeV and (b); 1.5 MeV of the energy.

Fig. 4.11 Decay and level scheme of ^{208}Tl.

Fig. 4.12 The backgrounds caused by ^{208}Tl in the source film.
(a); β ray followed by internal conversion electron.
(b); β ray followed by Compton electron.
(c); β ray followed by photo electron.

Chapter 5.
Fig. 5.1 Arrangement of the ^{100}Mo and the natural Mo source films mounted in the source holder.

Fig. 5.2 Close-up view around the source plane.

Chapter 6.
Fig. 6.1 Sum energy spectra of the β rays in RUN-A5 with OFHC dummy source foils.
(a); Spectrum from the raw data. There are photo peaks of the γ rays following β decays of ^{214}Pb and ^{214}Bi.
(b); Coincidence of two PLs.
(c); Anti coincidence with NaI.
(d); Coincidence of at least 5 out of 6 DC planes.

Fig. 6.2 Sum energy spectrum of the γ rays in RUN-A5 obtained by NaI in coincidence with at least one PL module. There can be found photo peaks of the γ rays emitted by β decays of ^{214}Pb and ^{214}Bi.
Fig. 6.3 Decay and level scheme of ^{214}Pb.

Chapter 7.

Fig. 7.1 Sum energy spectra of the β rays in RUN-D1 with the ^{100}Mo and the natural Mo source foils.

(a); Spectrum from the raw data.

(b); Coincidence of the two PLs is required.

(c); Spectrum vetoed by NaI.

(d) Coincidence of 5 or more DC planes out of 6.

Fig. 7.2 Energy spectrum from RUN-D01 obtained by NaI in coincidence with at least one PL module. The 295 keV and the 352 keV γ rays of ^{214}Pb and the 609 keV γ rays of ^{214}Bi are observed. Photo peaks of the other nuclei cannot be found.

Fig. 7.3 The trigger rate dependense of the background rate in the $0\nu\beta\beta$ region with $E_{\beta1+\beta2} \geq 2.5$ MeV. The background rate is roughly proportional to the trigger rate. It may be reduced almost completely by increasing the circulation rate of the N_2 gas. The aimed sensitivity for $0\nu\beta\beta$ with $T_{1/2}^{0\nu\beta\beta} \geq 10^{23}$ is expected to be achieved in that case.

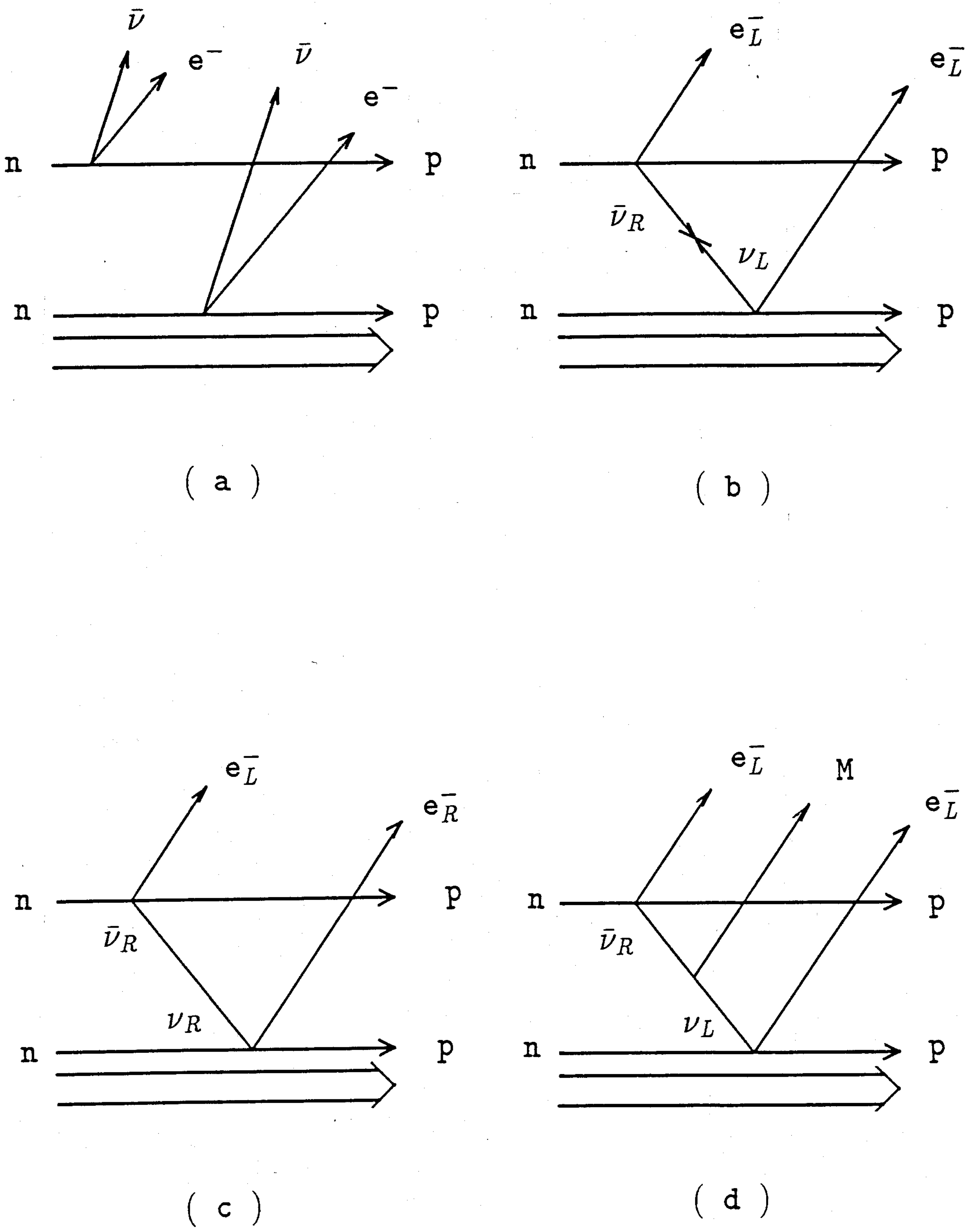
$\bar{\nu}$
e$^-$
$\bar{\nu}$
e$^-$
n
p
n
p
(a)
e$_L^-$
e$_L^-$
n
p
$\bar{\nu}_R$
ν_L
n
p
(b)
e$_L^-$
e$_R^-$
n
p
$\bar{\nu}_R$
ν_R
n
p
(c)
e$_L^-$
M
e$_L^-$
n
p
$\bar{\nu}_R$
ν_L
n
p
(d)

Fig. 1.1

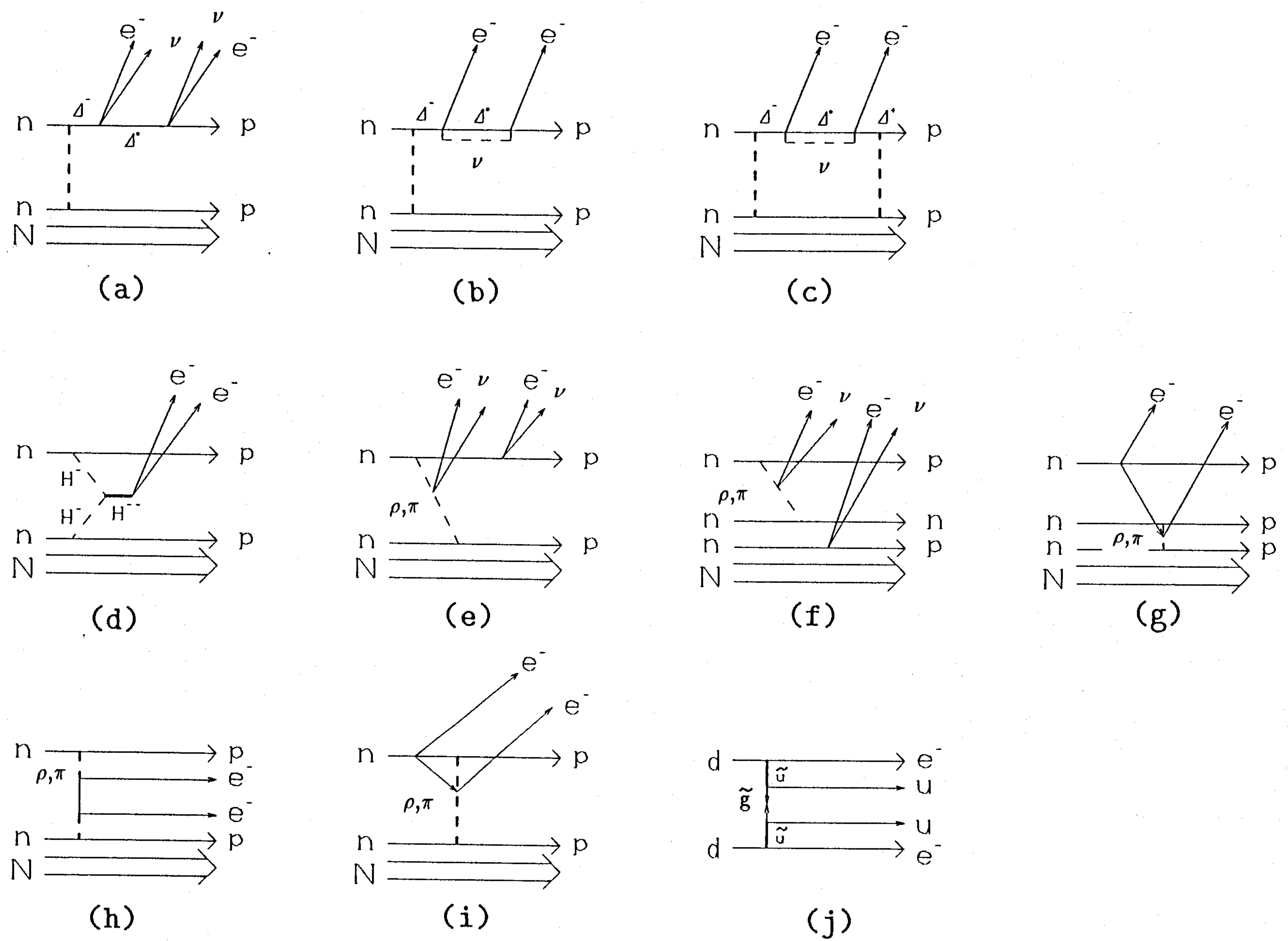
(a)
n
p
n
p
N
Δ^-
Δ^+
e^-
ν
ν
e^-
(b)
Δ^-
Δ^+
ν
(c)
(d)
H^-
H^-
H^{--}
(e)
ρ,π
(f)
(g)
(h)
(i)
(j)
d
u
$\tilde{u}$
$\tilde{g}$

Fig. 1.2

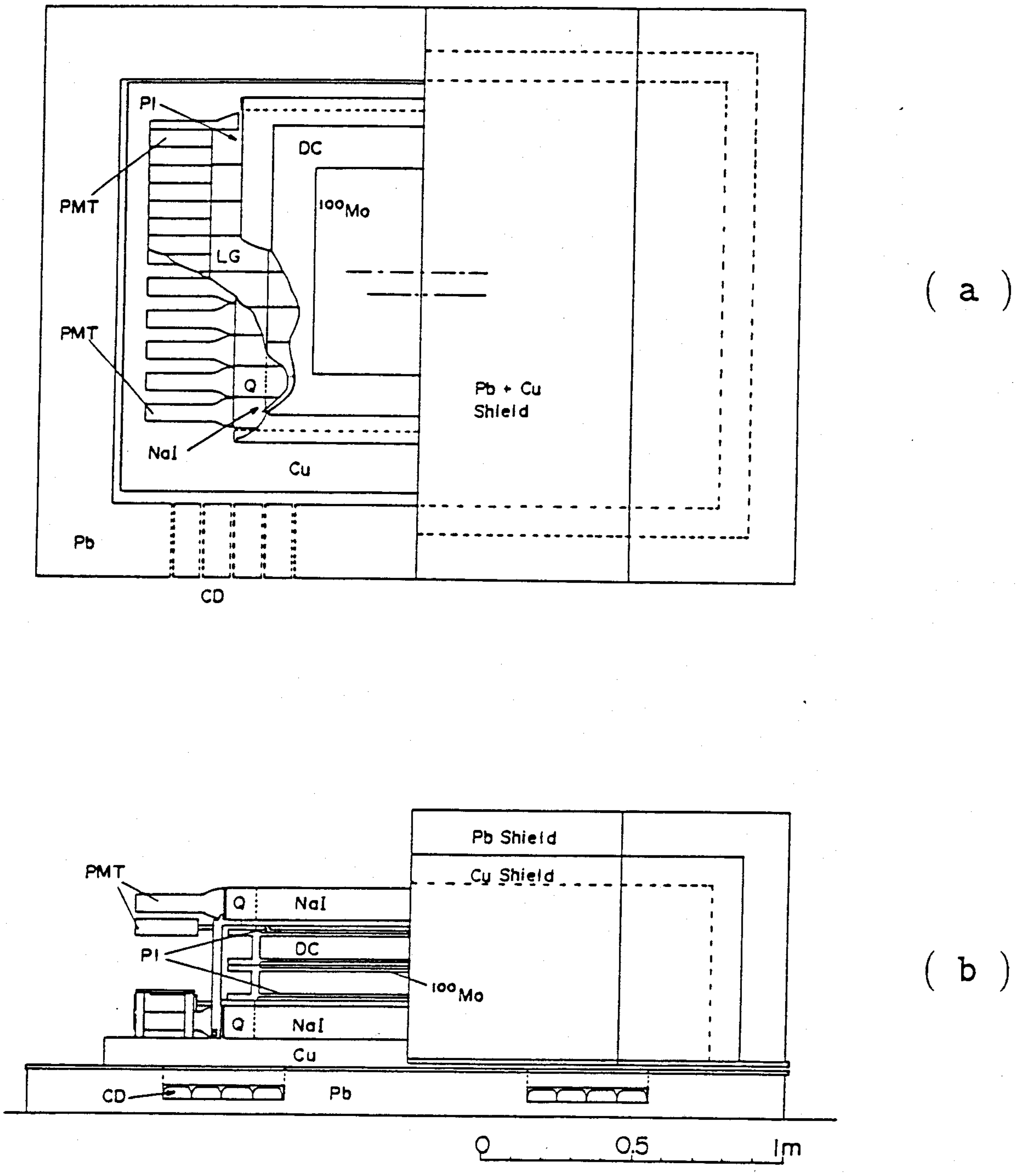
PI
PMT
DC
^{100}Mo
LG
PMT
Q
NaI
Cu
Pb + Cu Shield
Pb
CD
(a)
PMT
Pb Shield
Cu Shield
Q
NaI
PI
DC
^{100}Mo
Q
NaI
Cu
CD
Pb
0
0.5
1m
(b)

Fig. 2.1

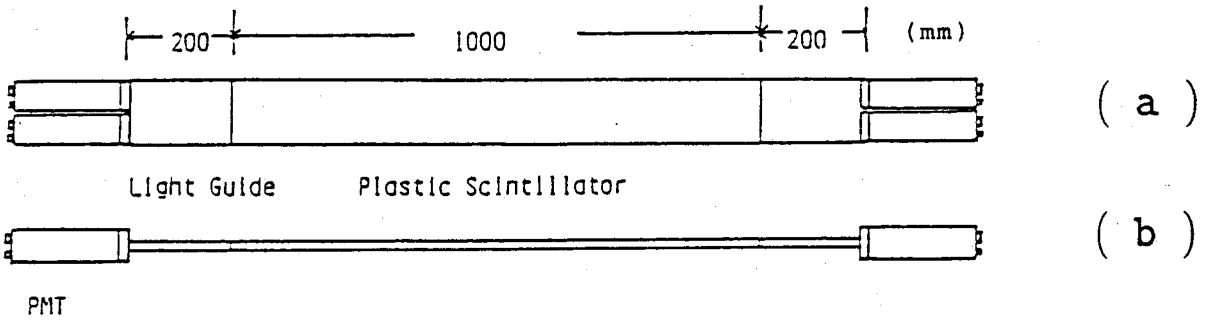
200
1000
200
(mm)
(a)
Light Guide
Plastic Scintillator
(b)
PMT

Fig. 2.2

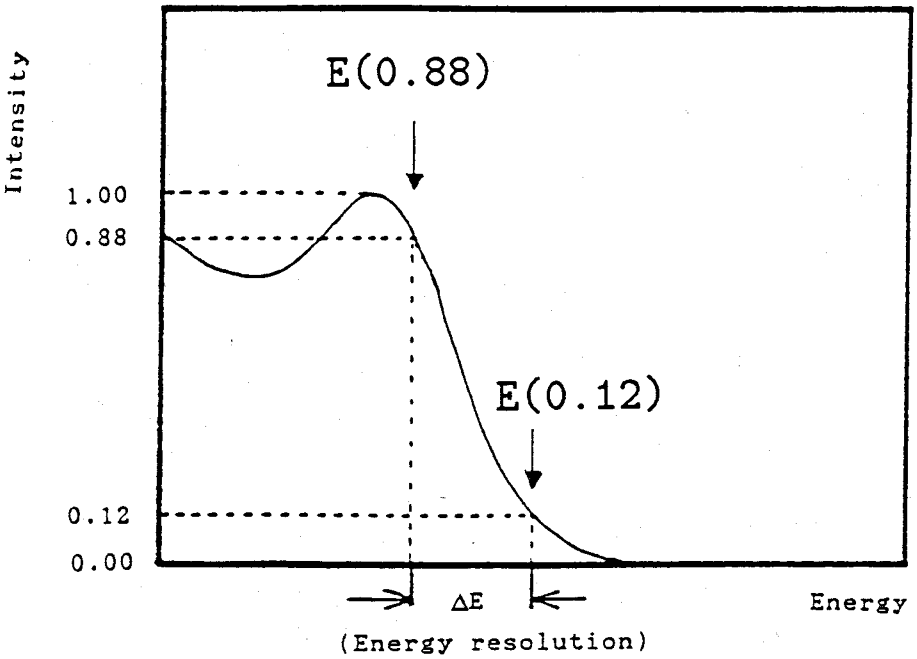
Intensity
E(0.88)
E(0.12)
1.00
0.88
0.12
0.00
ΔE
Energy
(Energy resolution)

Fig. 2.3

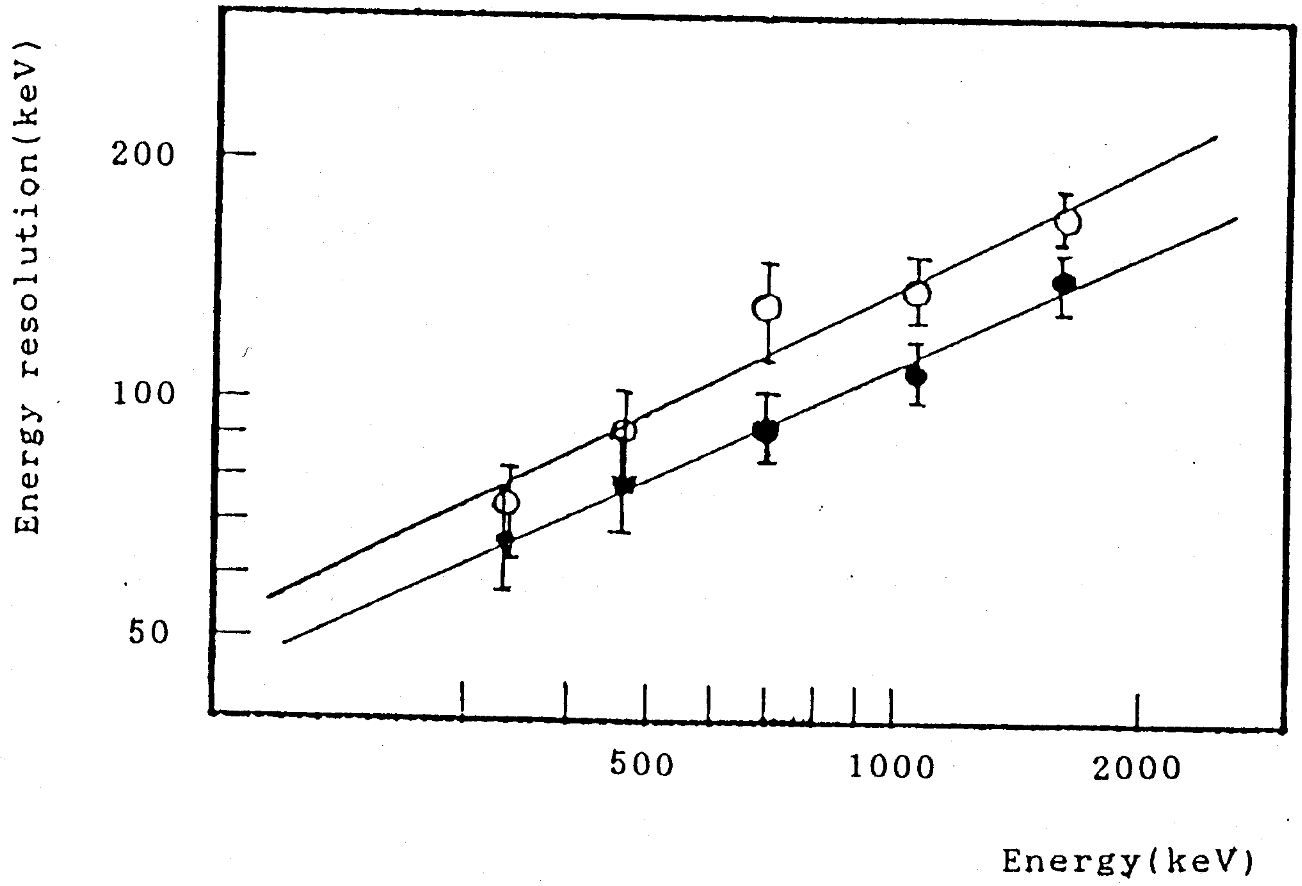

Fig. 2.4

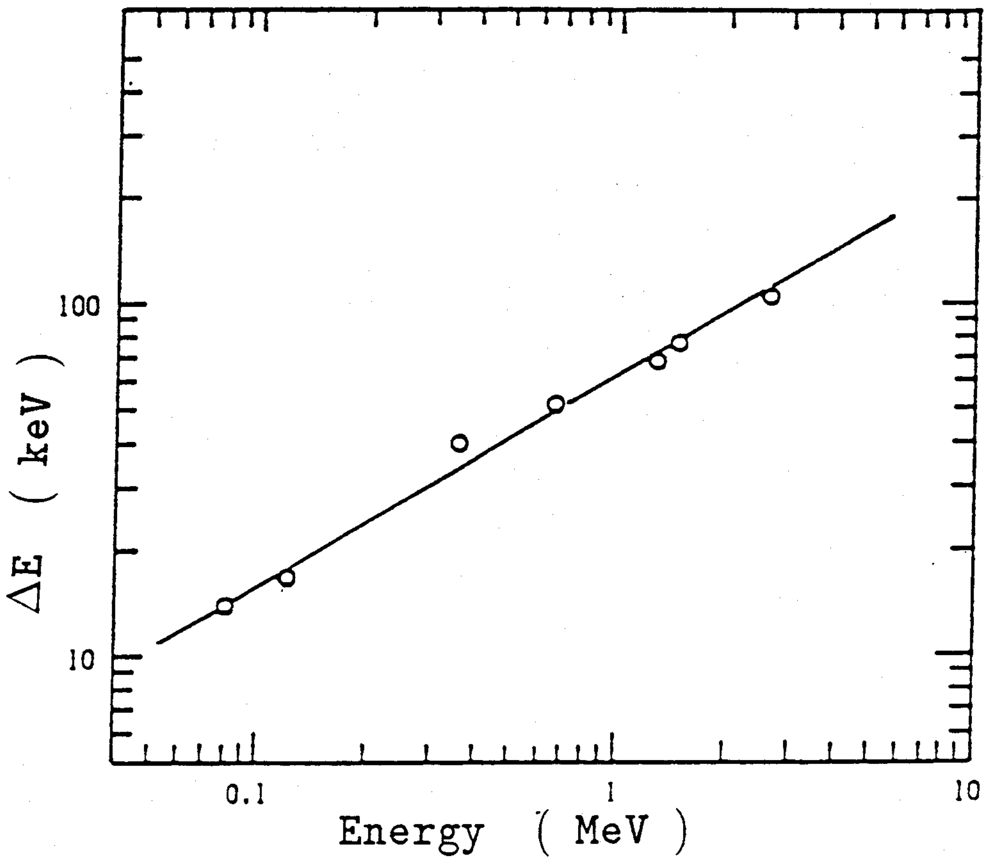
ΔE (keV)
100
10
0.1
1
10
Energy (MeV)

Fig. 2.5

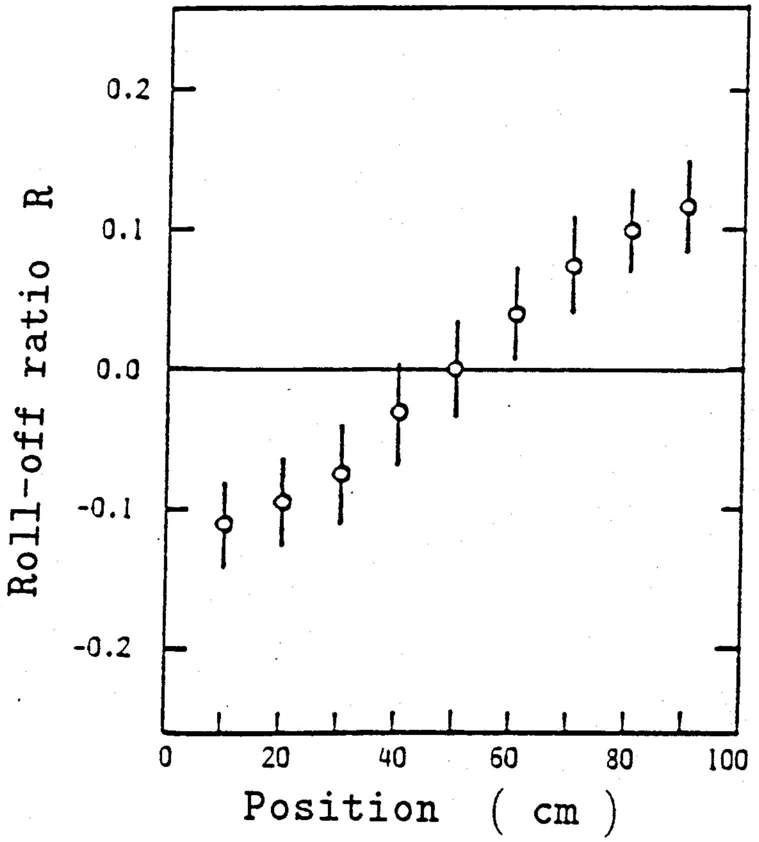
Roll-off ratio R
0.2
0.1
0.0
-0.1
-0.2
0
20
40
60
80
100
Position (cm)

Fig. 2.6

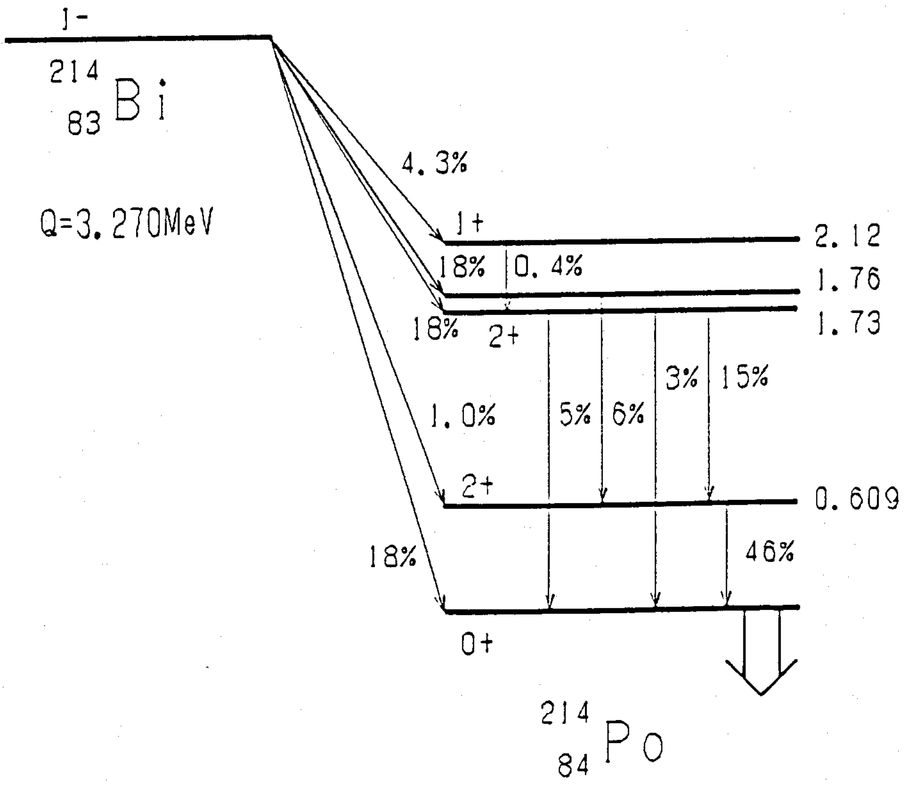
1-
$^{214}_{83}$Bi
Q=3.270MeV
4.3%
1+
2.12
18%
0.4%
1.76
18%
2+
1.73
1.0%
5%
6%
3%
15%
2+
0.609
18%
46%
0+
$^{214}_{84}$Po

Fig. 3.1

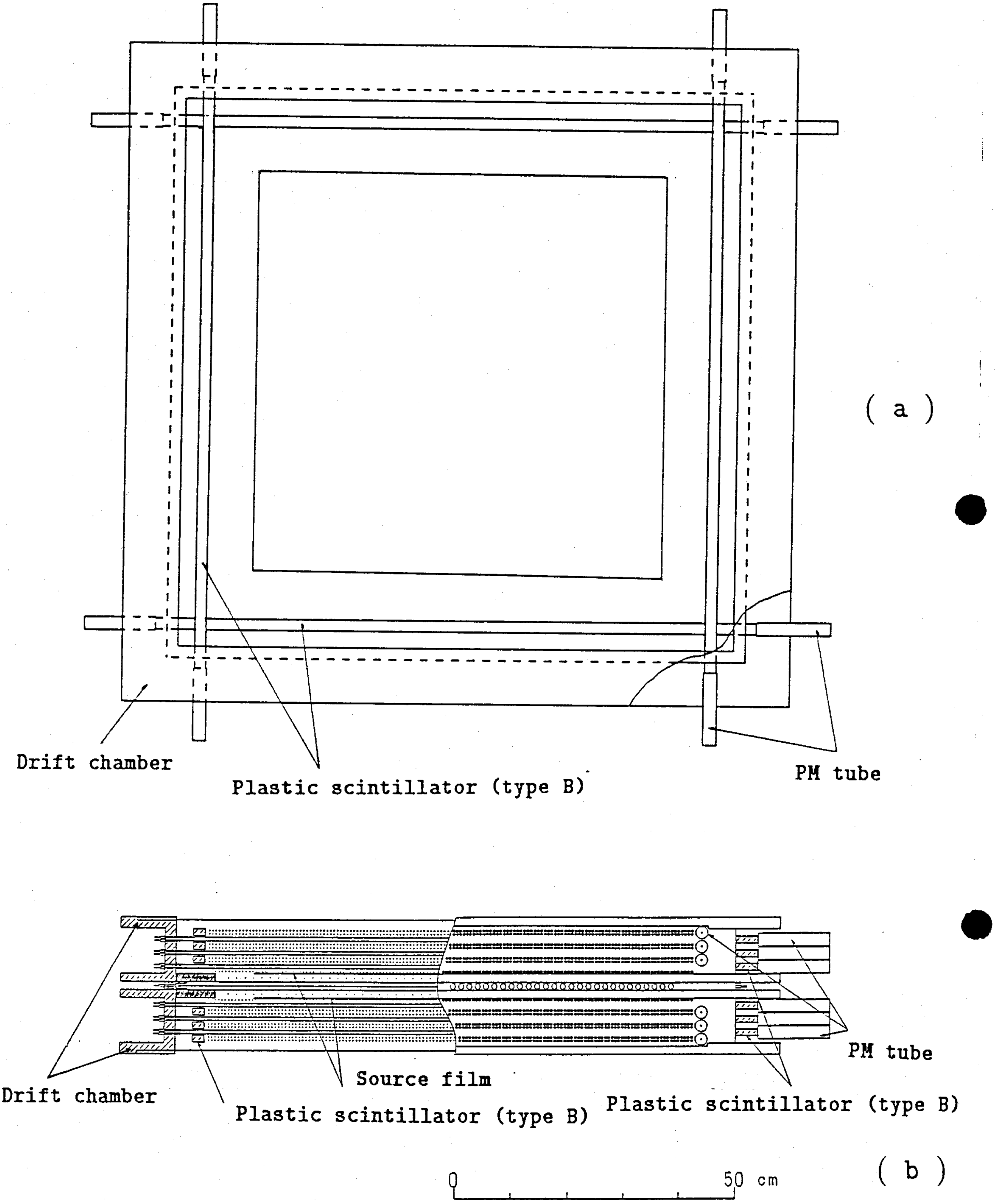
Drift chamber
Plastic scintillator (type B)
PM tube
(a)
PM tube
Drift chamber
Source film
Plastic scintillator (type B)
Plastic scintillator (type B)
0
50 cm
(b)

Fig. 3.2

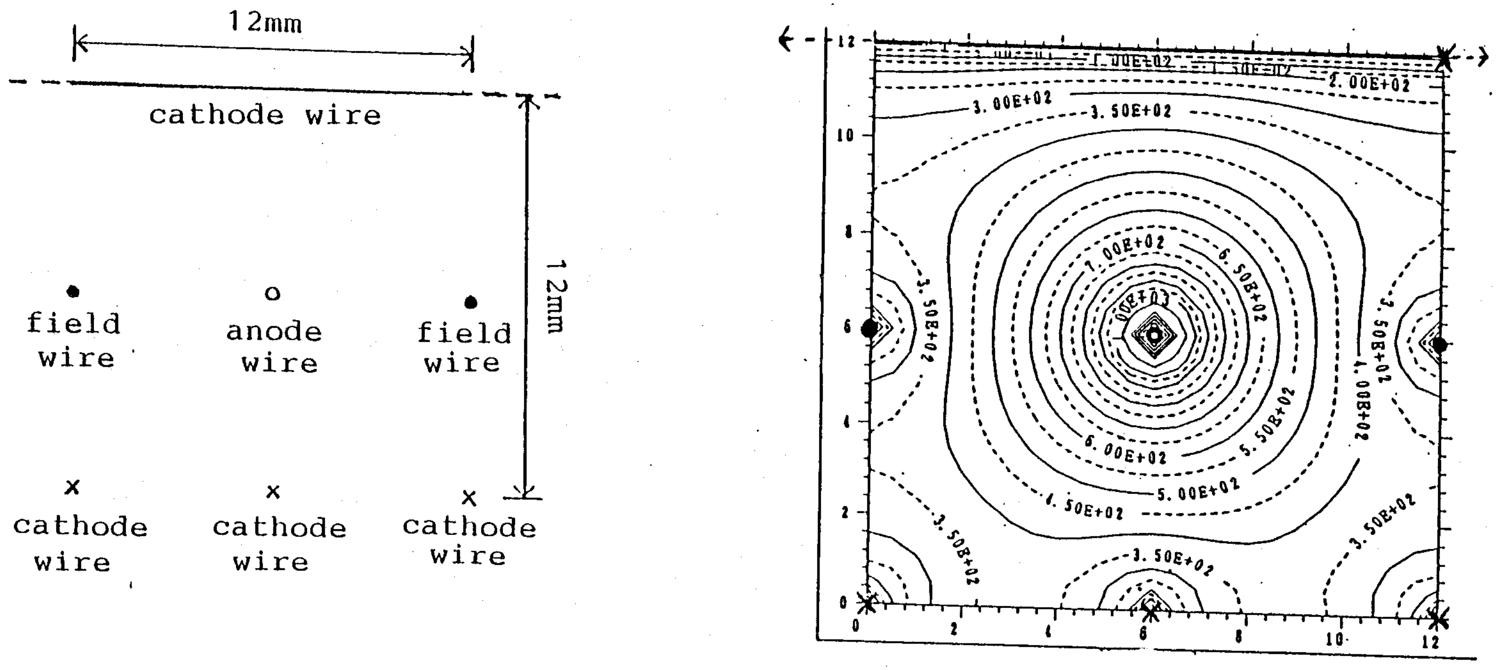
12mm
cathode wire
12mm
field wire
anode wire
field wire
cathode wire
cathode wire
cathode wire
1.00E+02
2.00E+02
3.00E+02
3.50E+02
4.00E+02
4.50E+02
5.00E+02
5.50E+02
6.00E+02
6.50E+02
7.00E+02
0
2
4
6
8
10
12

Fig. 3.3

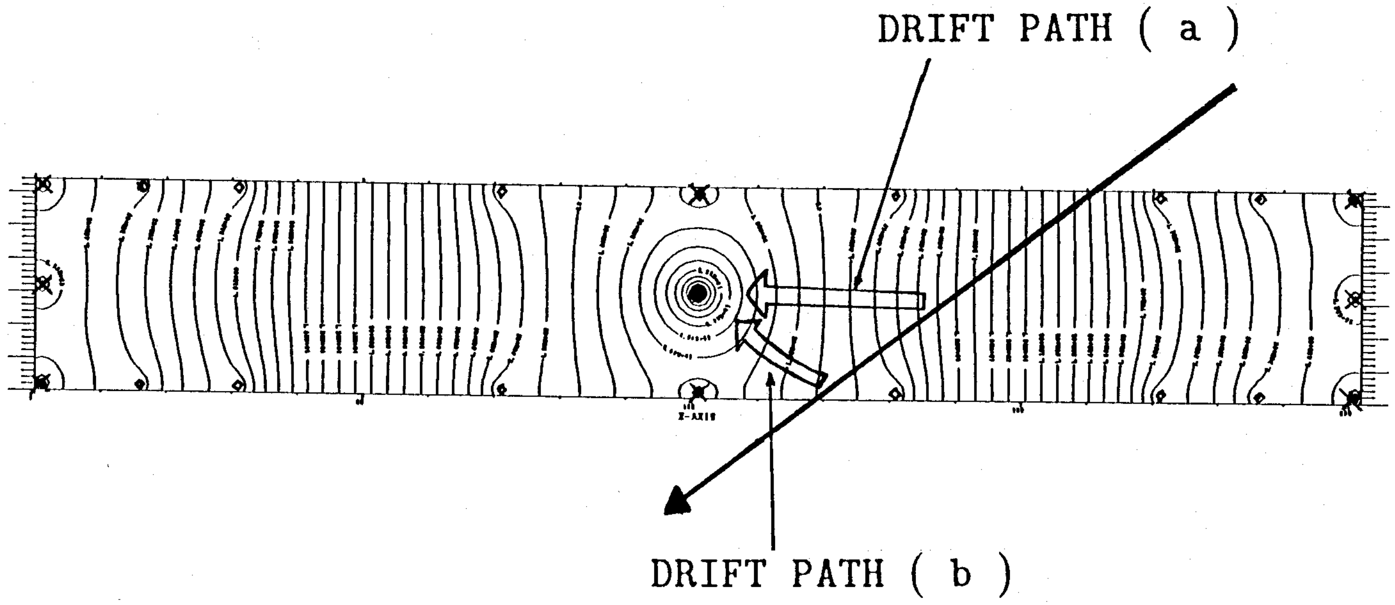

Fig. 3.4

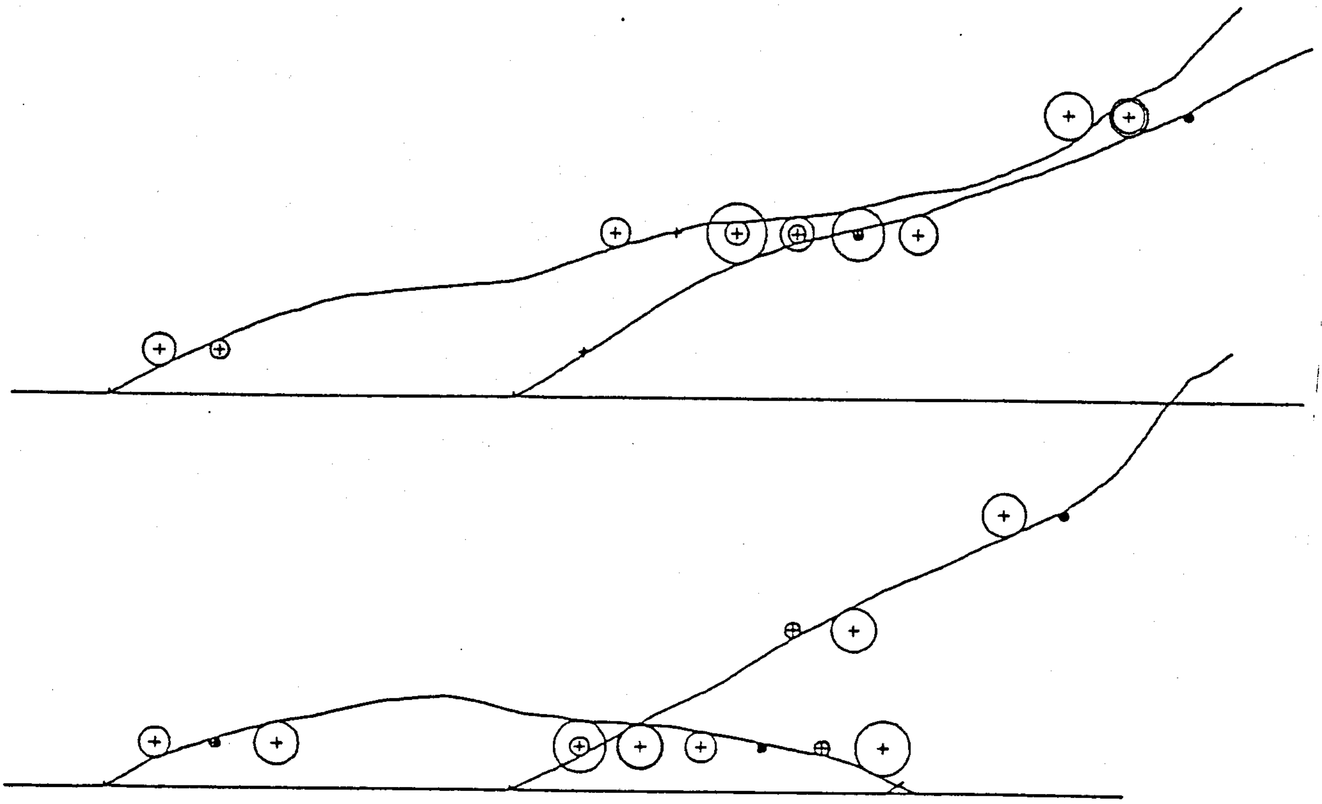

(a) AR - CO_2 85 : 15 E_β = 500 keV

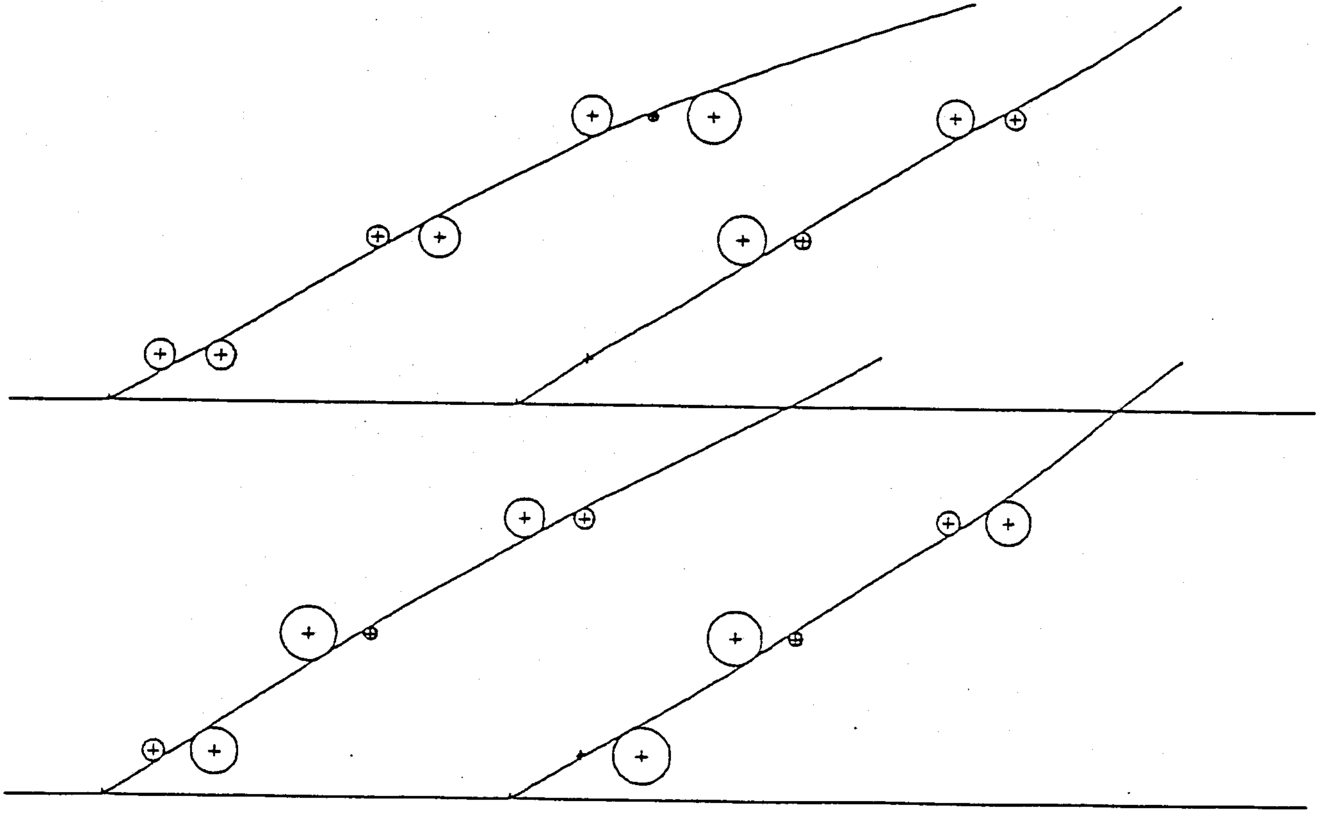

(b) HE - CO_2 85 : 15 E_β = 500 keV

Fig. 3.5

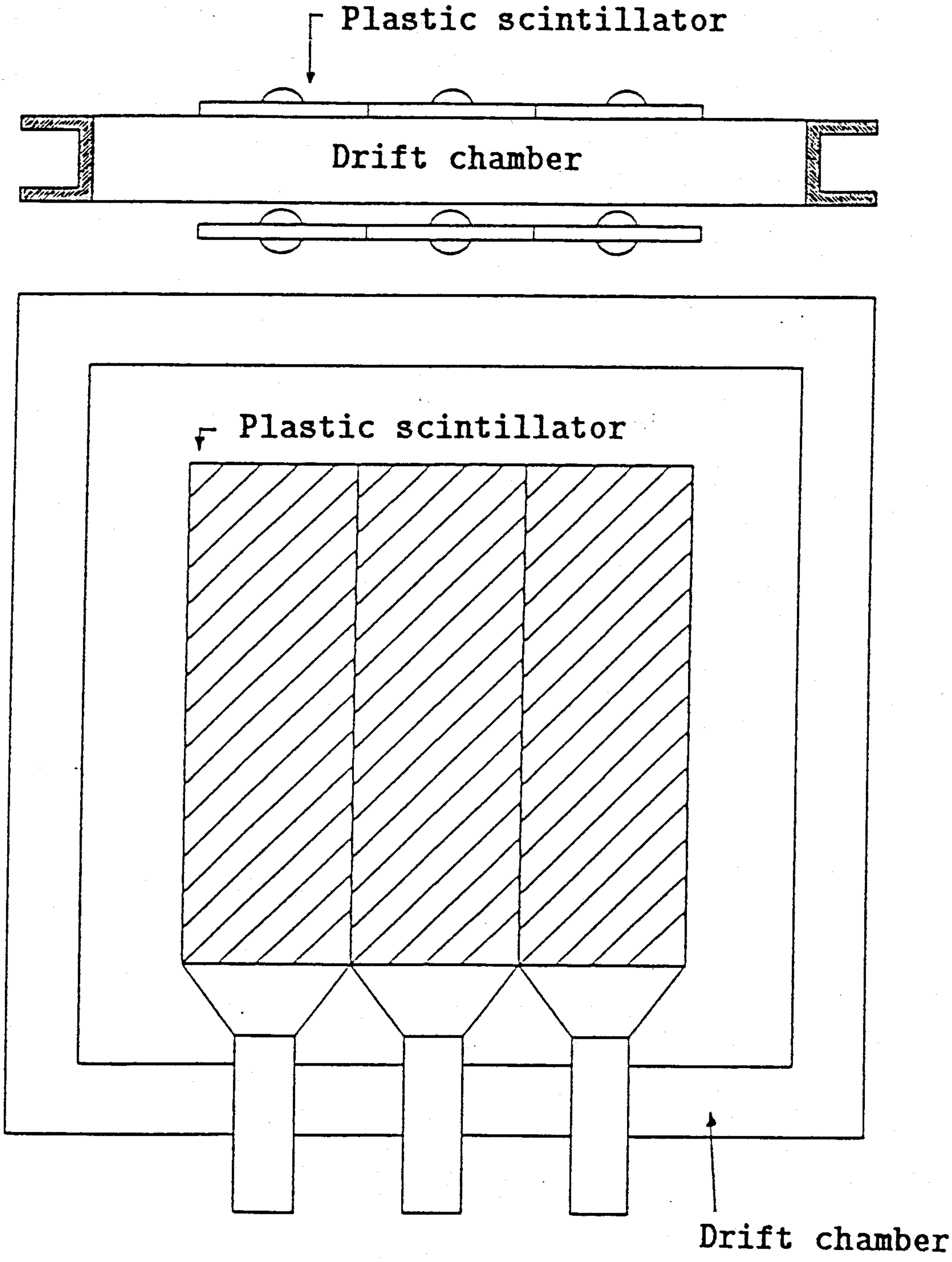
Plastic scintillator
Drift chamber
Plastic scintillator
Drift chamber

Fig. 3.6

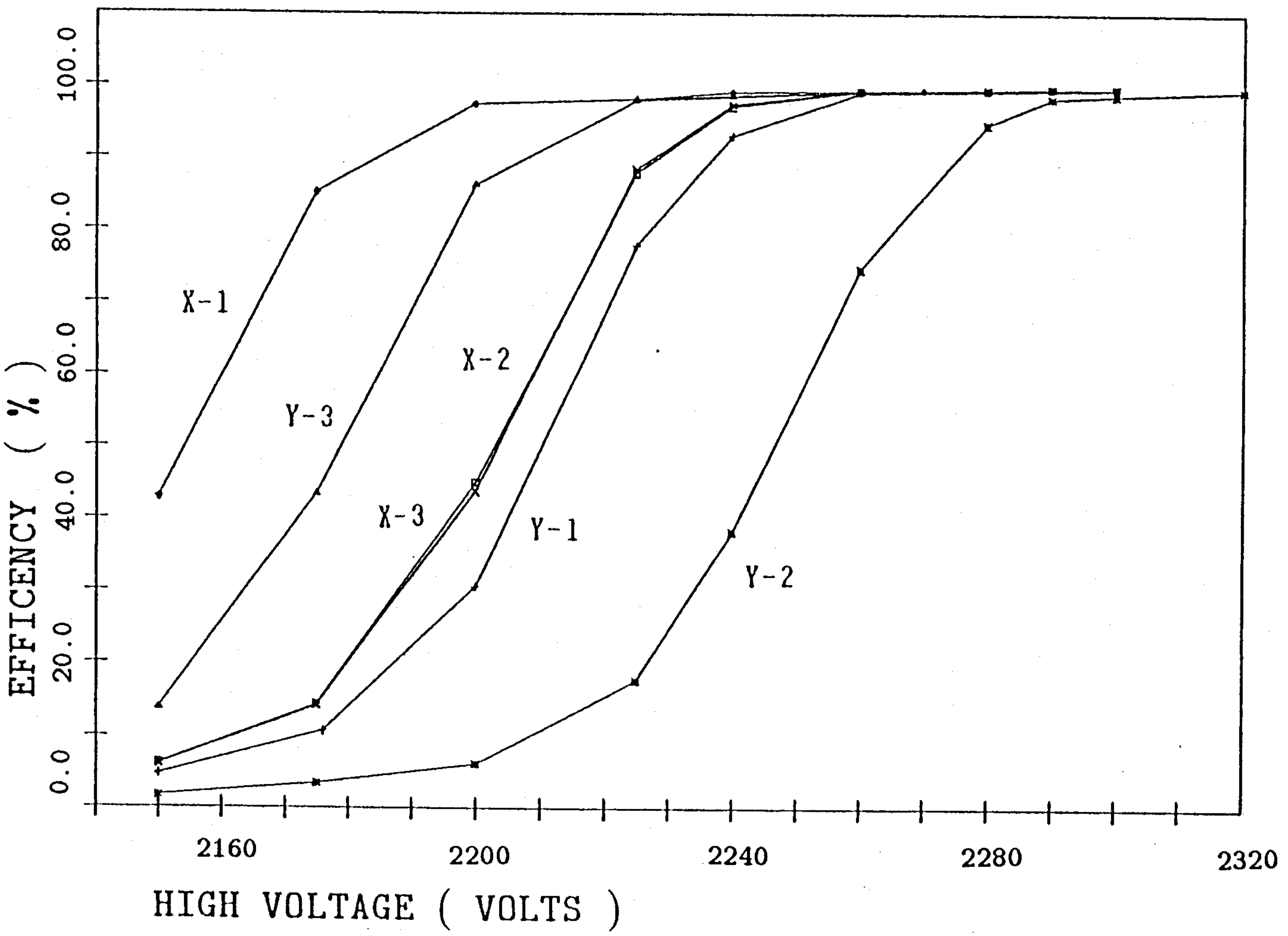
100.0
80.0
60.0
40.0
20.0
0.0
EFFICENCY (%)
2160
2200
2240
2280
2320
HIGH VOLTAGE (VOLTS)
X-1
Y-3
X-2
X-3
Y-1
Y-2

Fig. 3.7 (a)

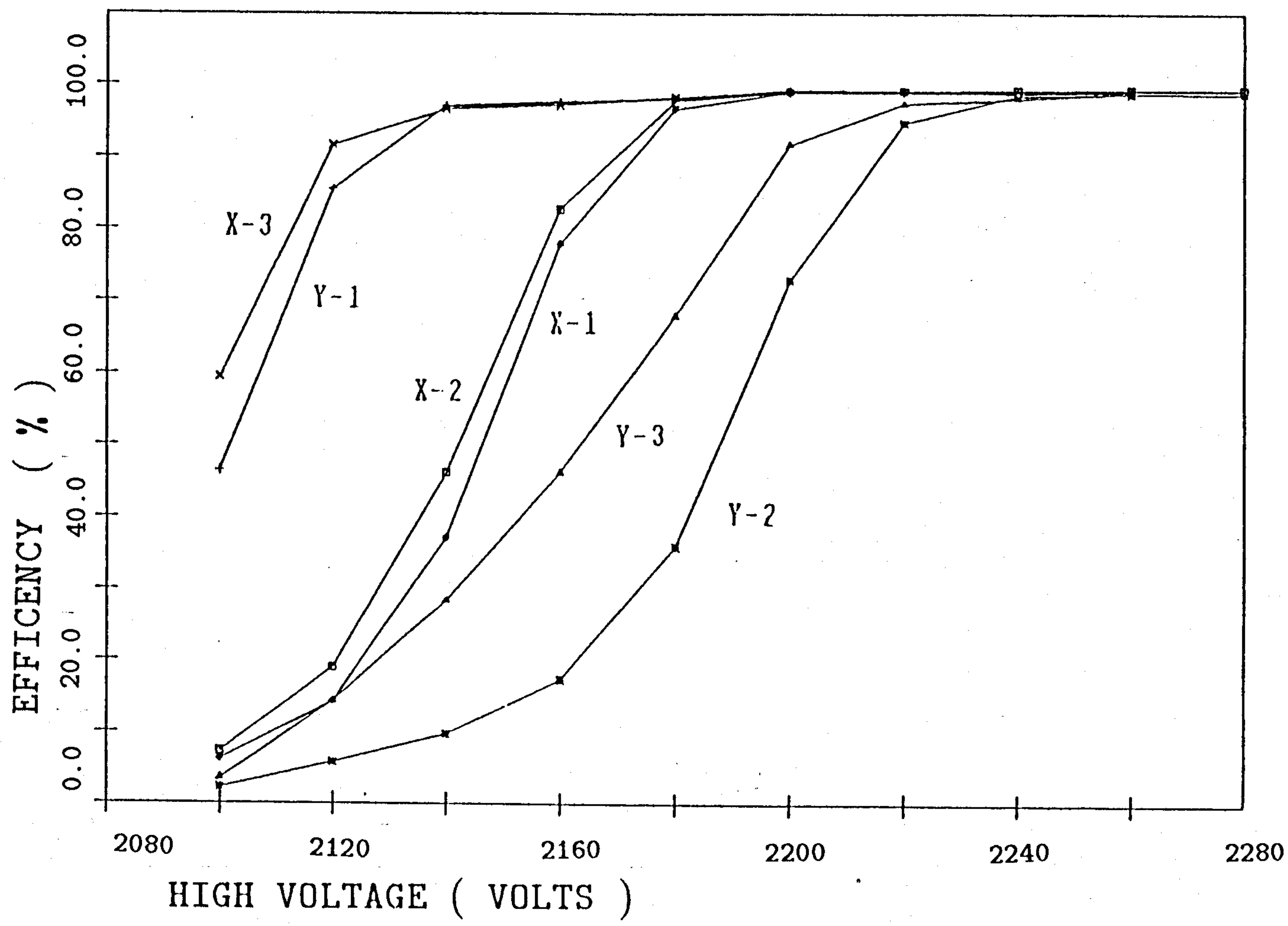
100.0
80.0
60.0
40.0
20.0
0.0
EFFICENCY (%)
2080
2120
2160
2200
2240
2280
HIGH VOLTAGE (VOLTS)
X-3
Y-1
X-2
X-1
Y-3
Y-2

Fig. 3.7 (b)

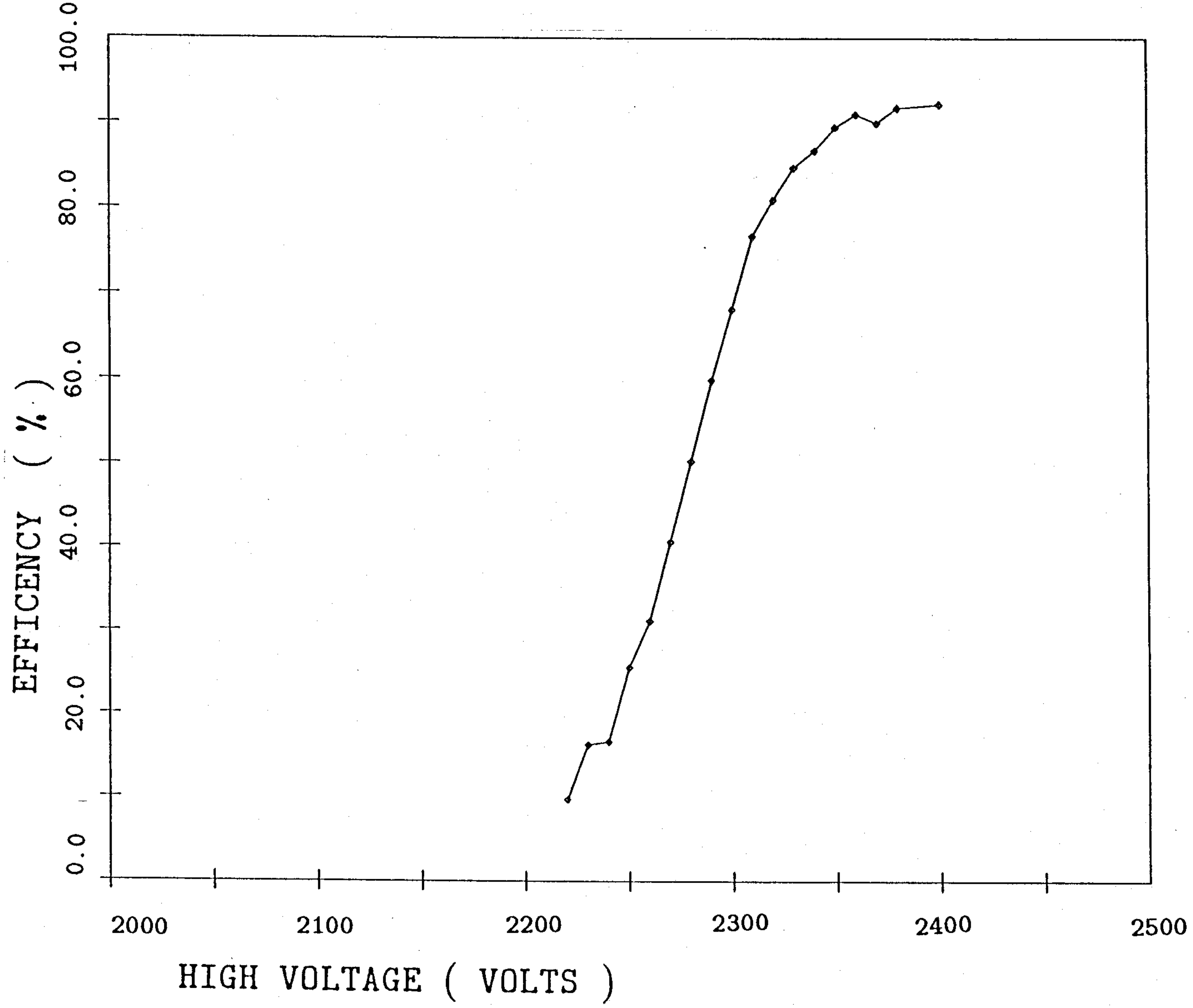
100.0
80.0
60.0
40.0
20.0
0.0
EFFICENCY (%)
2000
2100
2200
2300
2400
2500
HIGH VOLTAGE (VOLTS)

Fig. 3.8

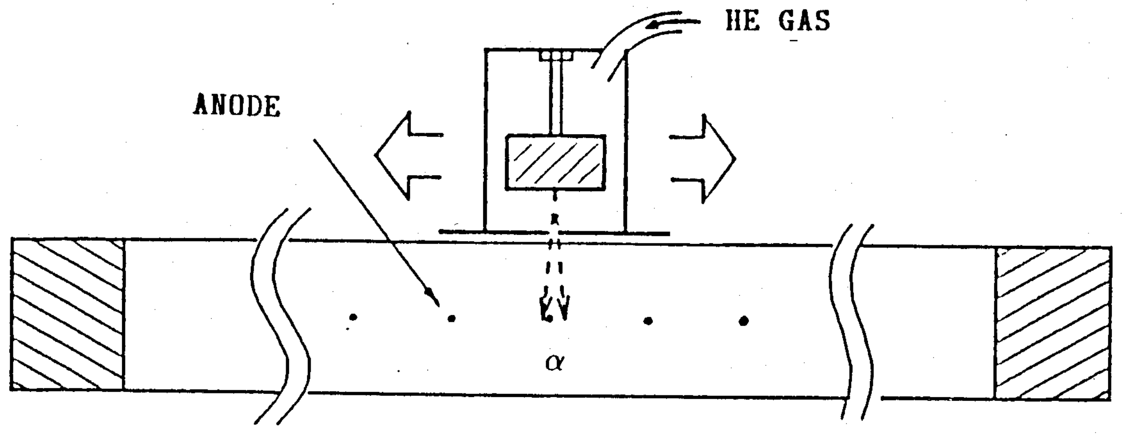

Fig. 3.9

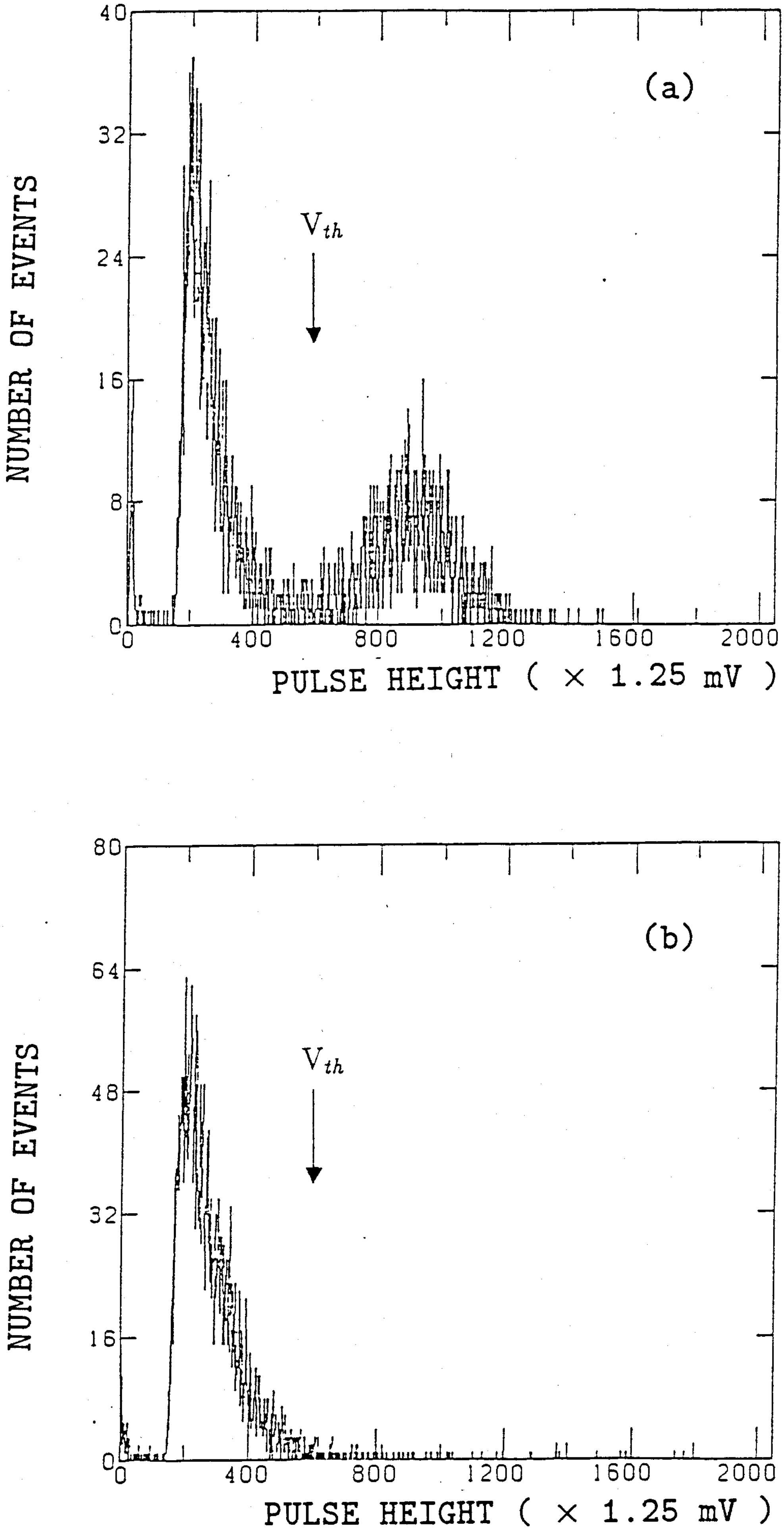
(a)
NUMBER OF EVENTS
0
8
16
24
32
40
V$_{th}$
0
400
800
1200
1600
2000
PULSE HEIGHT (× 1.25 mV)
(b)
NUMBER OF EVENTS
0
16
32
48
64
80
V$_{th}$
0
400
800
1200
1600
2000
PULSE HEIGHT (× 1.25 mV)

Fig. 3.10

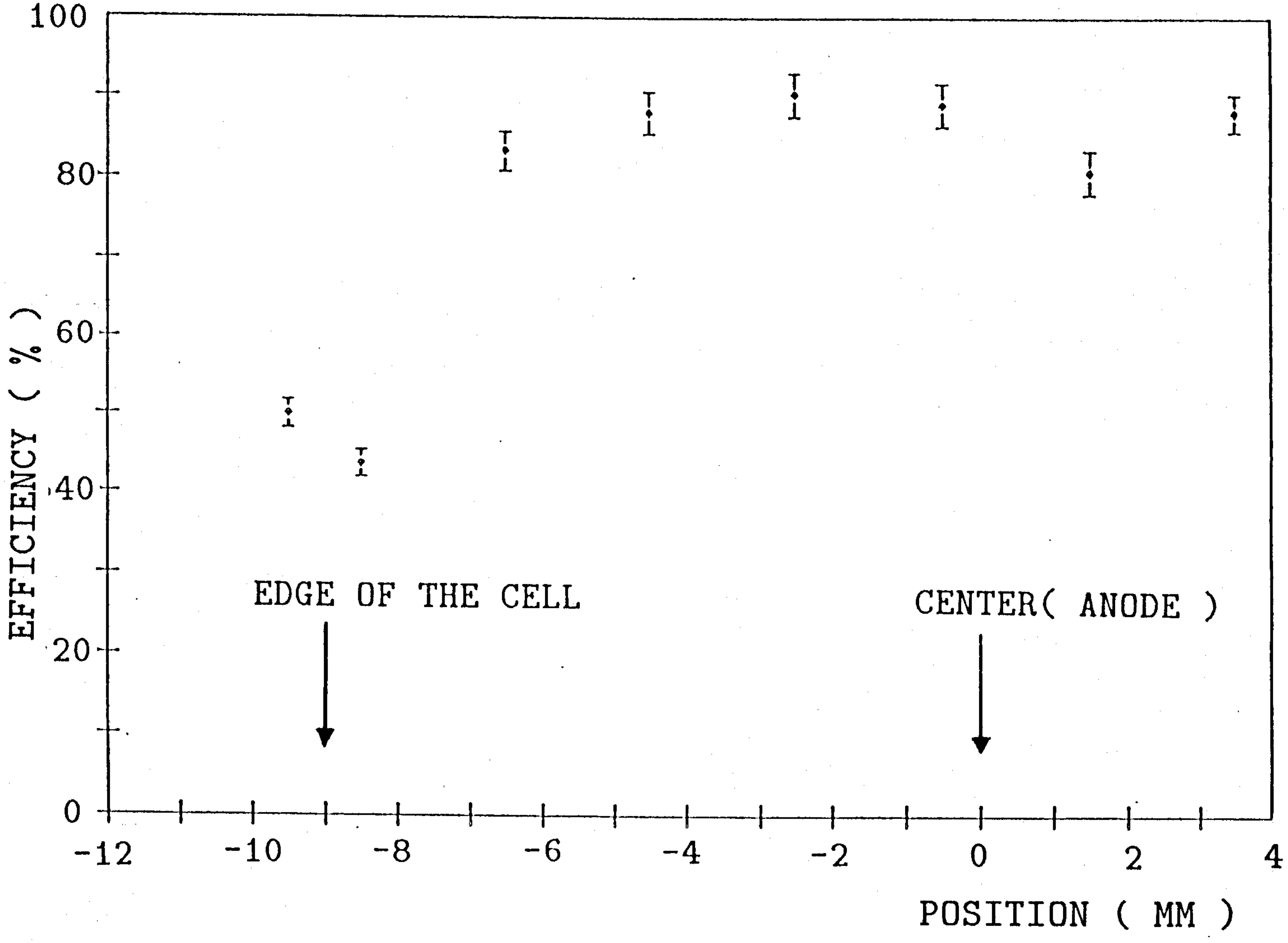
100
80
60
40
20
0
EFFICIENCY (%)
EDGE OF THE CELL
CENTER(ANODE)
-12
-10
-8
-6
-4
-2
0
2
4
POSITION (MM)

Fig. 3.11

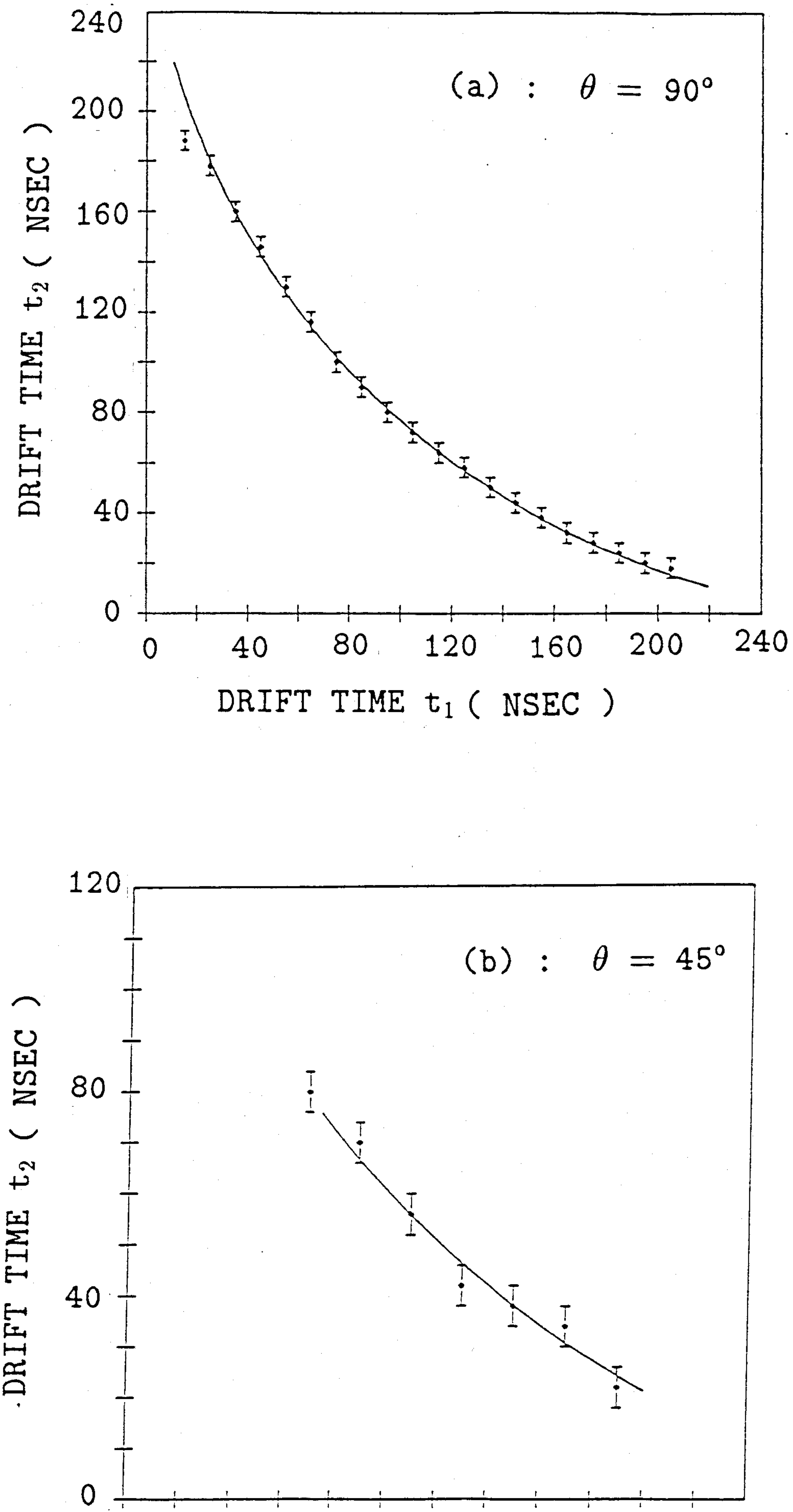
(a) : $\theta = 90°$
DRIFT TIME t_2 (NSEC)
DRIFT TIME t_1 (NSEC)
0
40
80
120
160
200
240
(b) : $\theta = 45°$
DRIFT TIME t_2 (NSEC)
DRIFT TIME t_1 (NSEC)
0
40
80
120

Fig. 3.12

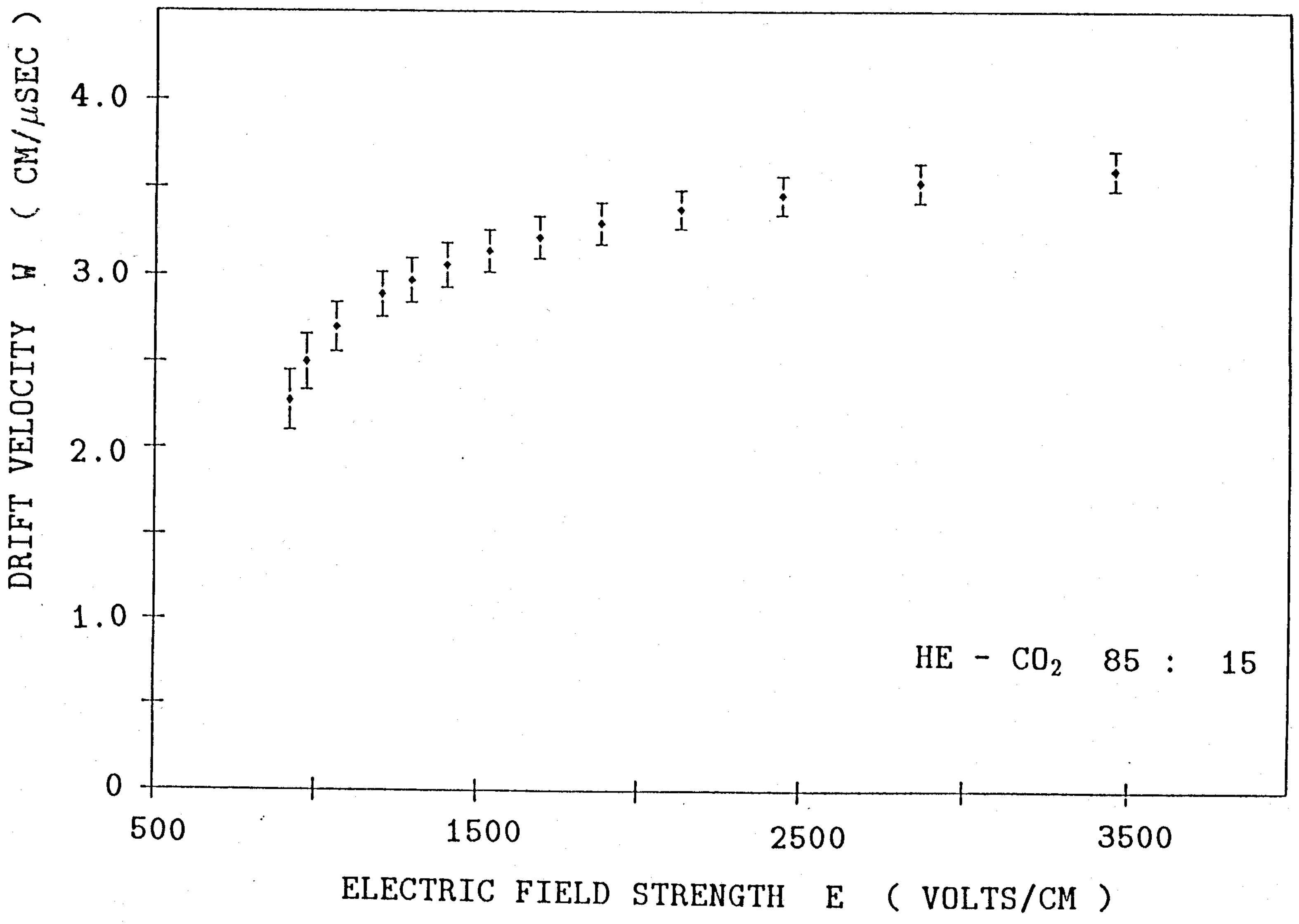
DRIFT VELOCITY W (CM/μSEC)
4.0
3.0
2.0
1.0
0
500
1500
2500
3500
ELECTRIC FIELD STRENGTH E (VOLTS/CM)
HE - CO_2 85 : 15

Fig. 3.13

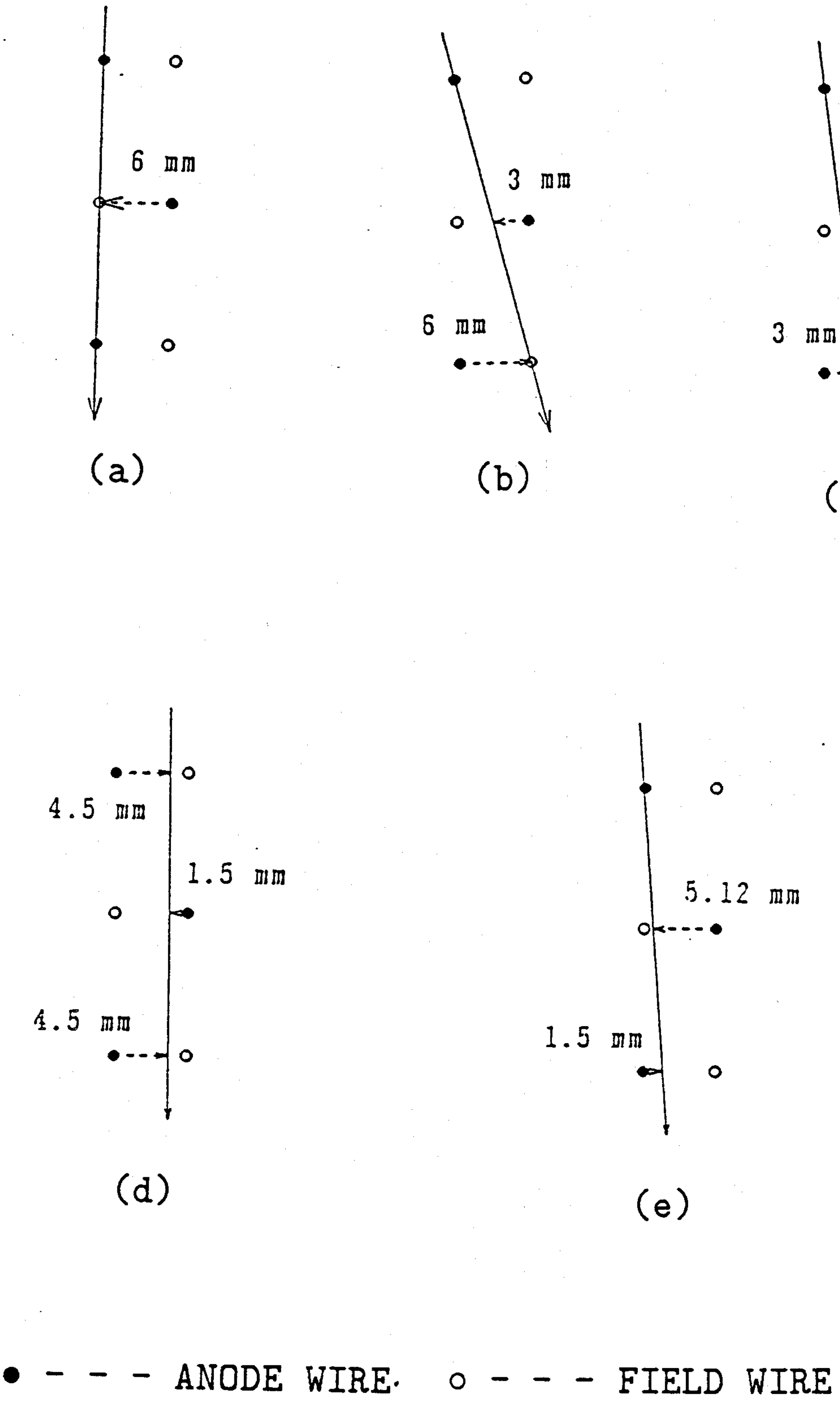
6 mm
(a)
3 mm
6 mm
(b)
4.5 mm
3 mm
(c)
4.5 mm
1.5 mm
4.5 mm
(d)
5.12 mm
1.5 mm
(e)
● - - - ANODE WIRE
○ - - - FIELD WIRE

Fig. 3.14

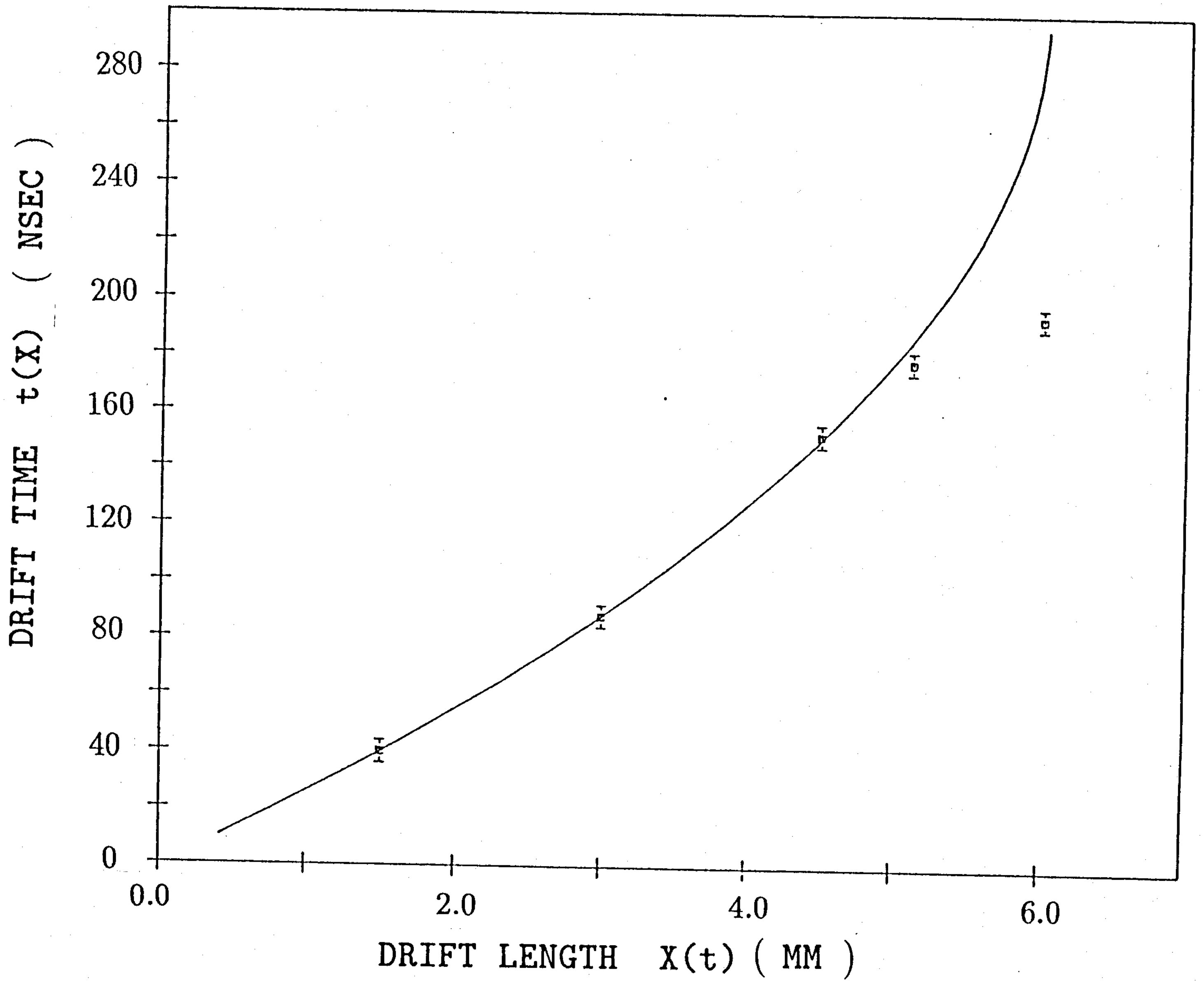
DRIFT TIME t(X) (NSEC)
280
240
200
160
120
80
40
0
0.0
2.0
4.0
6.0
DRIFT LENGTH X(t) (MM)

Fig. 3.15

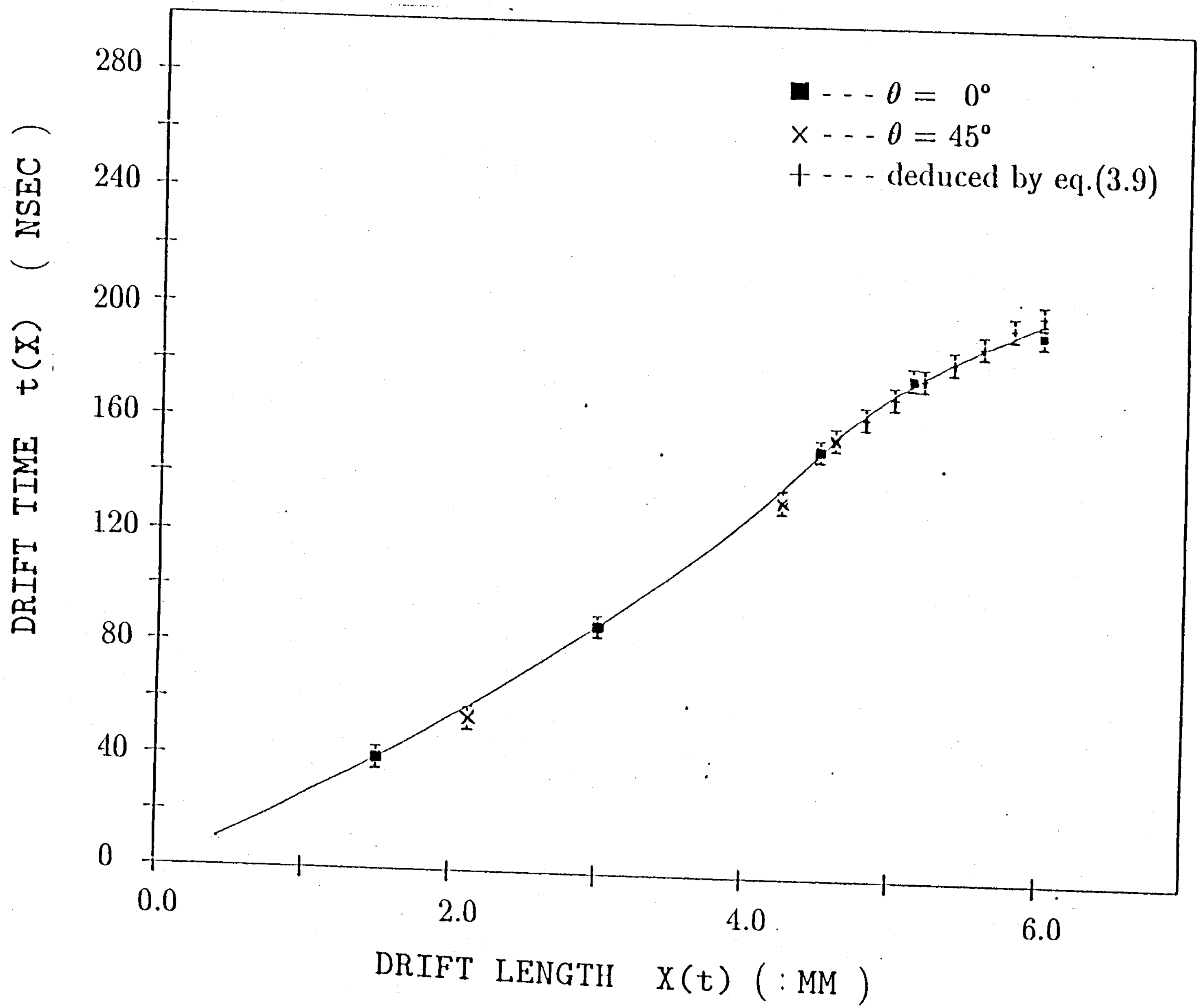
■ - - - $\theta =$ 0°
× - - - $\theta =$ 45°
+ - - - deduced by eq.(3.9)
DRIFT TIME t(X) (NSEC)
280
240
200
160
120
80
40
0
0.0
2.0
4.0
6.0
DRIFT LENGTH X(t) (: MM)

Fig. 3.16

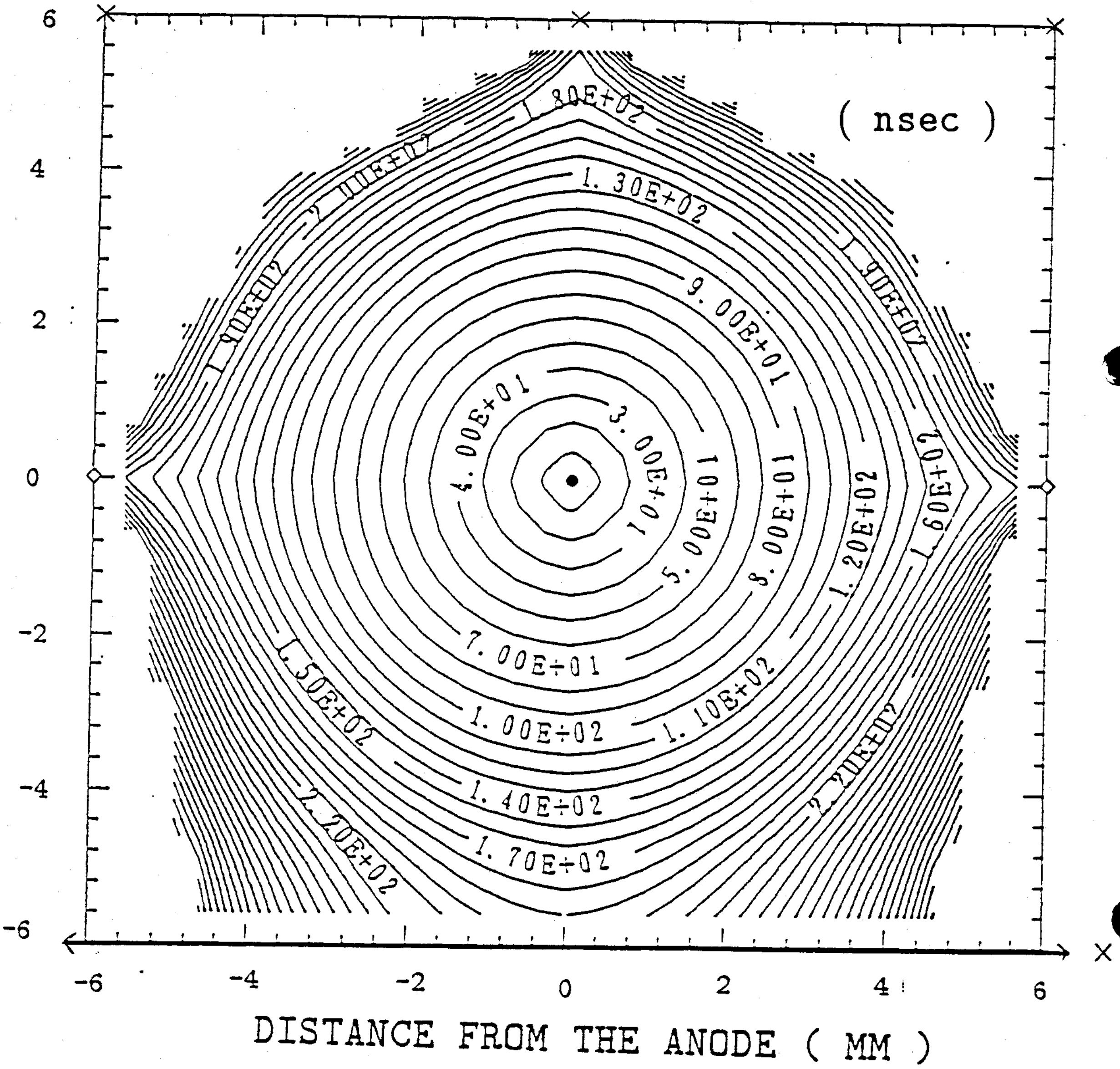
(nsec)
1.80E+02
2.00E+02
1.30E+02
1.90E+02
1.90E+02
9.00E+01
1.00E+01
4.00E+01
3.00E+01
1.00E+01
8.00E+01
1.20E+02
1.60E+02
5.00E+01
7.00E+01
1.00E+02
1.10E+02
1.50E+02
2.00E+02
1.40E+02
1.70E+02
2.20E+02
6
4
2
0
-2
-4
-6
-6
-4
-2
0
2
4
6
DISTANCE FROM THE ANODE (MM)

Fig. 3.17

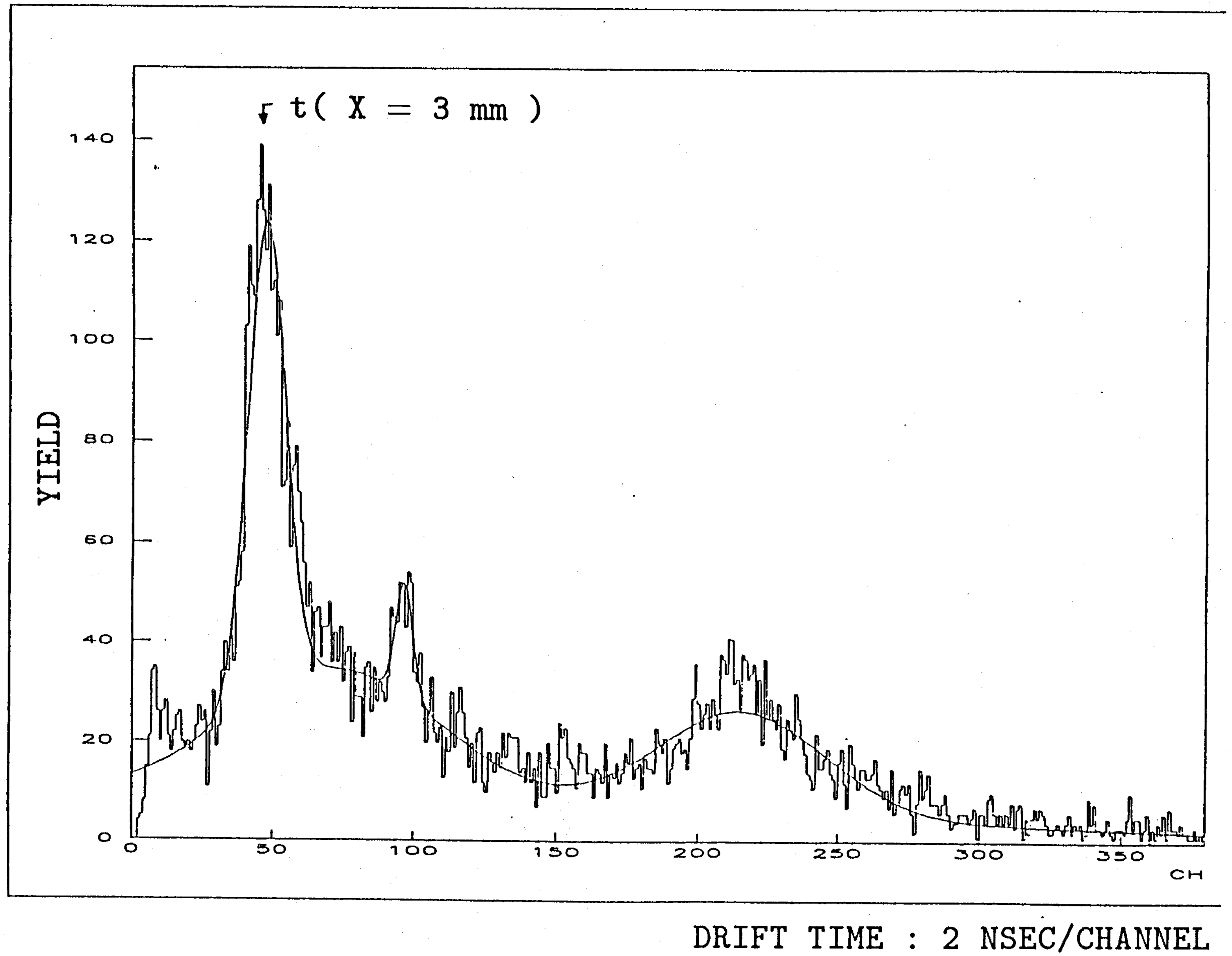
t(X = 3 mm)
YIELD
0
20
40
60
80
100
120
140
0
50
100
150
200
250
300
350
CH
DRIFT TIME : 2 NSEC/CHANNEL

Fig. 3.18

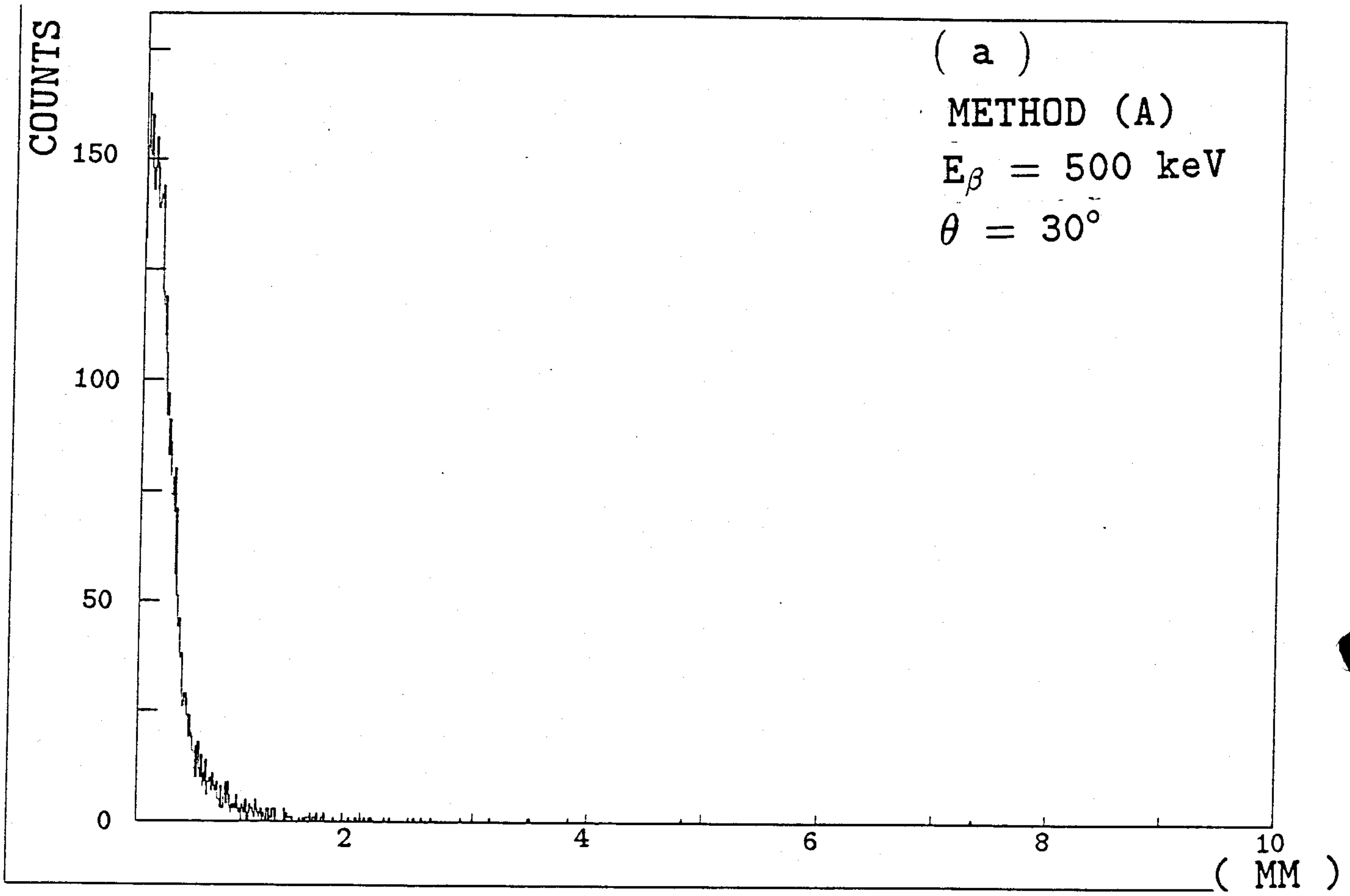

COUNTS
150
100
50
0
2
4
6
8
10
(MM)
(a)
METHOD (A)
E_β = 500 keV
θ = 30°

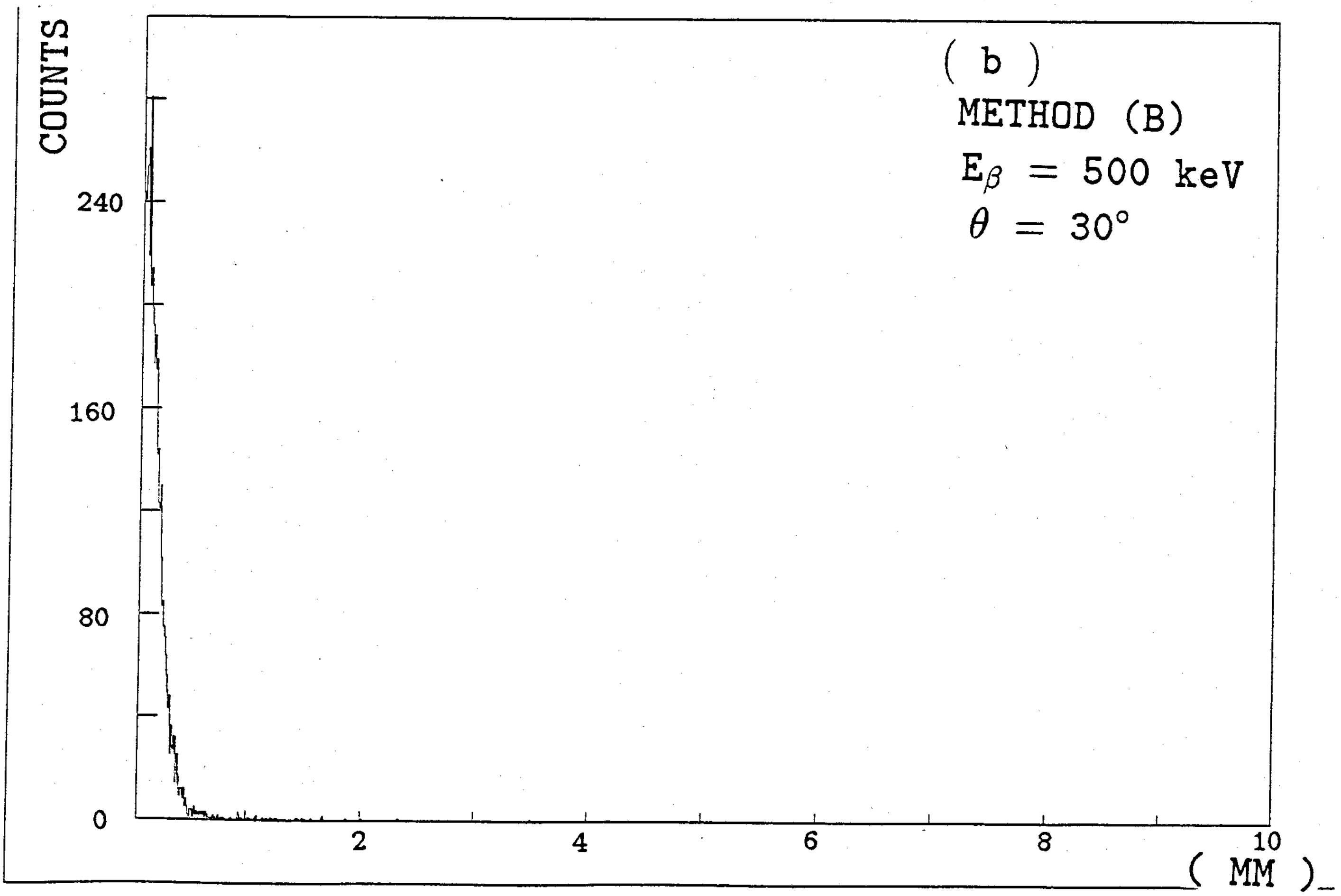

COUNTS
240
160
80
0
2
4
6
8
10
(MM)
(b)
METHOD (B)
E_β = 500 keV
θ = 30°

Fig. 3.19

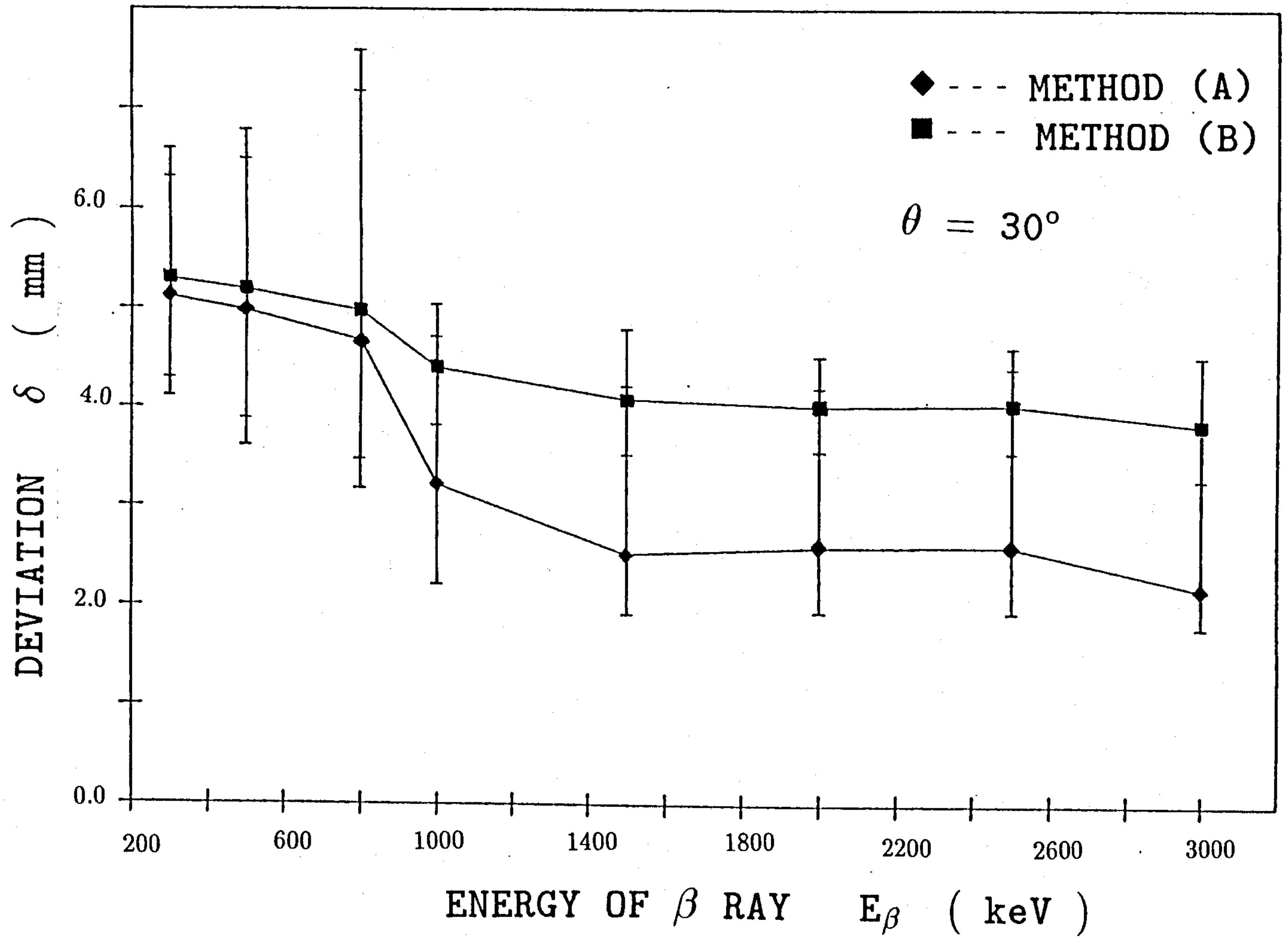
◆ - - - METHOD (A)
■ - - - METHOD (B)
$\theta = 30°$
DEVIATION δ (mm)
0.0
2.0
4.0
6.0
200
600
1000
1400
1800
2200
2600
3000
ENERGY OF β RAY E_β (keV)

Fig. 3.20 (a)

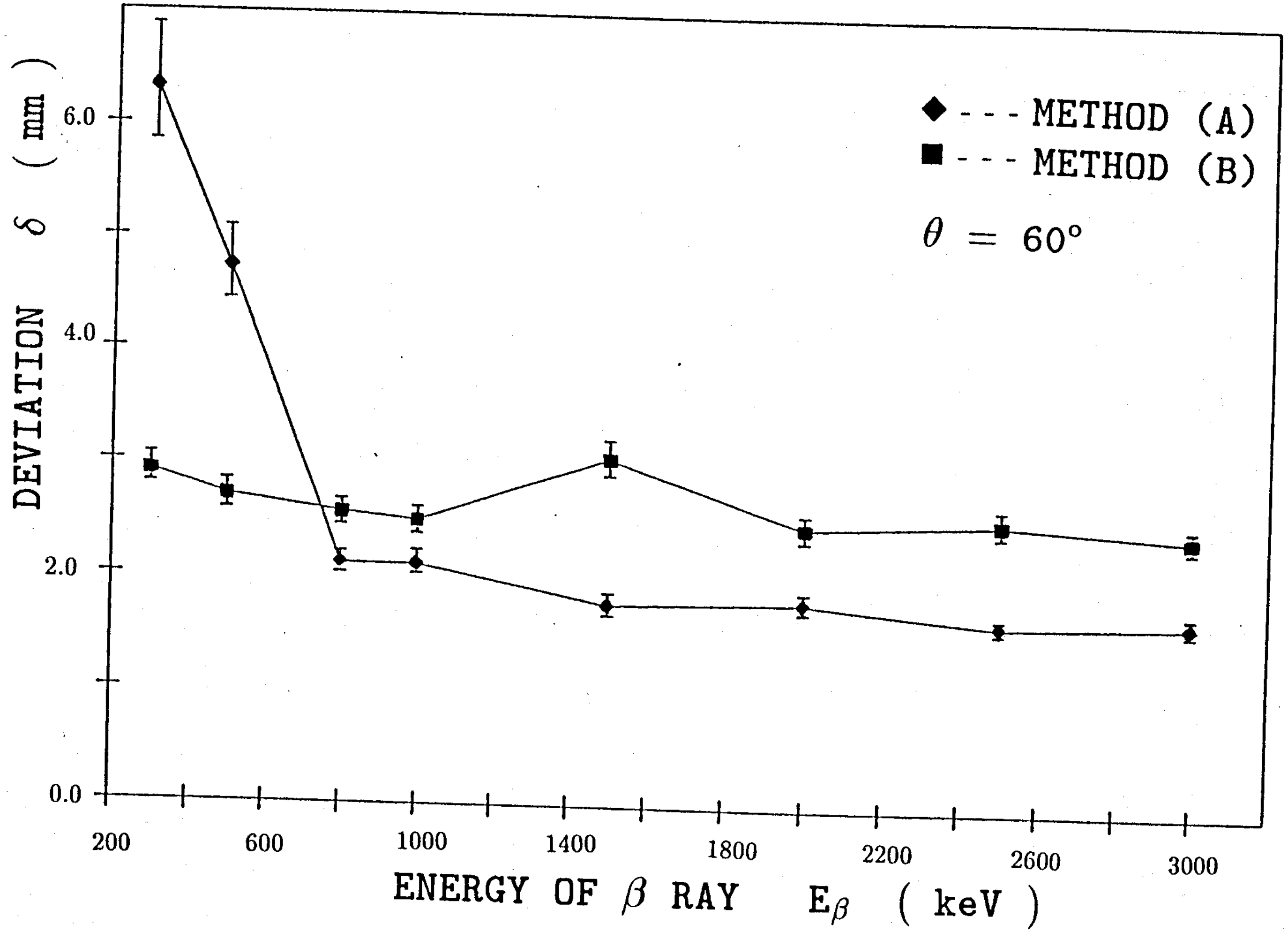
DEVIATION δ (mm)
0.0
2.0
4.0
6.0
200
600
1000
1400
1800
2200
2600
3000
ENERGY OF β RAY E_β (keV)
◆ - - - METHOD (A)
■ - - - METHOD (B)
θ = 60°

Fig. 3.20 (b)

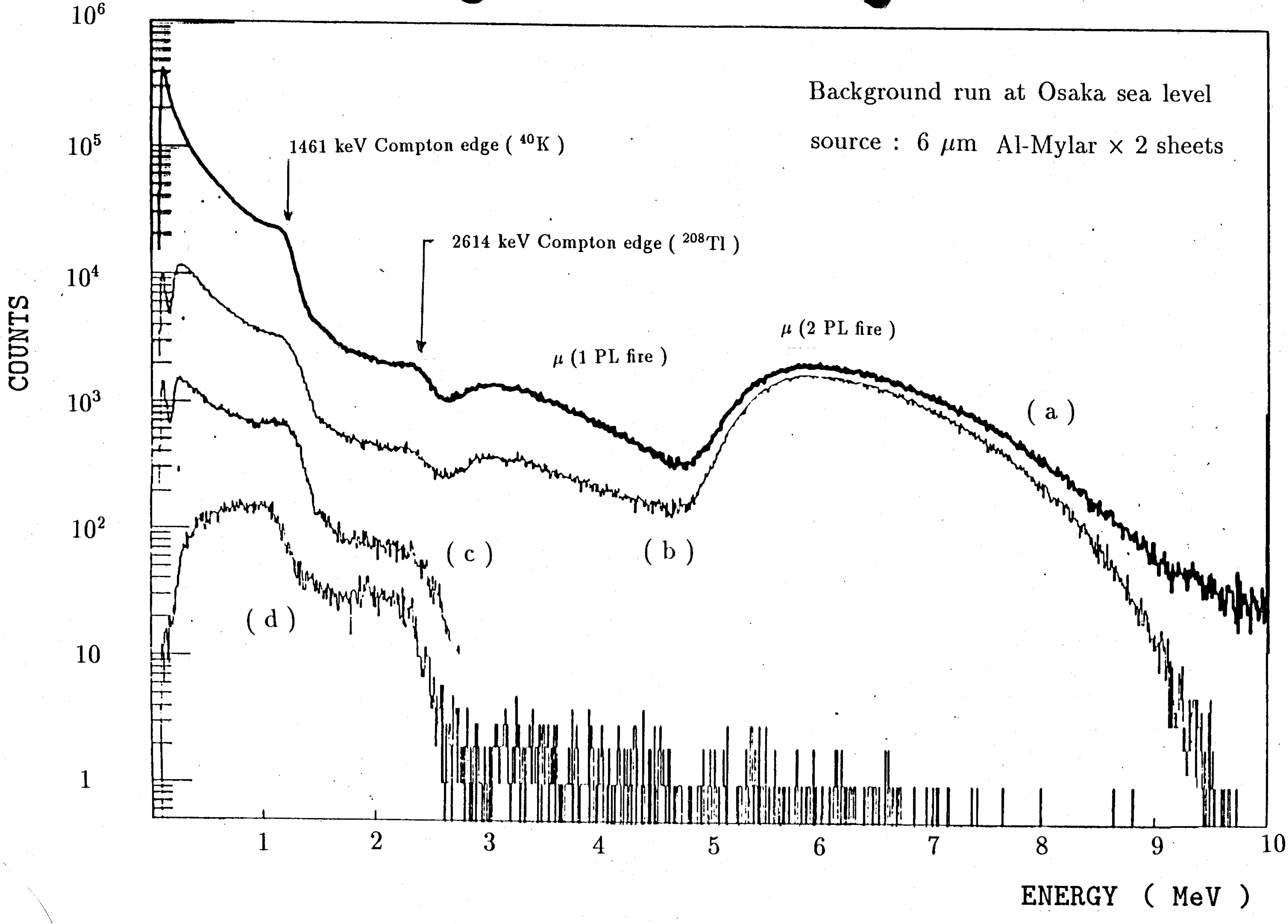

Background run at Osaka sea level
source : 6 μm Al-Mylar × 2 sheets
1461 keV Compton edge (^{40}K)
2614 keV Compton edge (^{208}Tl)
μ (1 PL fire)
μ (2 PL fire)
(a)
(b)
(c)
(d)
COUNTS
10^6
10^5
10^4
10^3
10^2
10
1
1
2
3
4
5
6
7
8
9
10
ENERGY (MeV)

Fig. 4.1

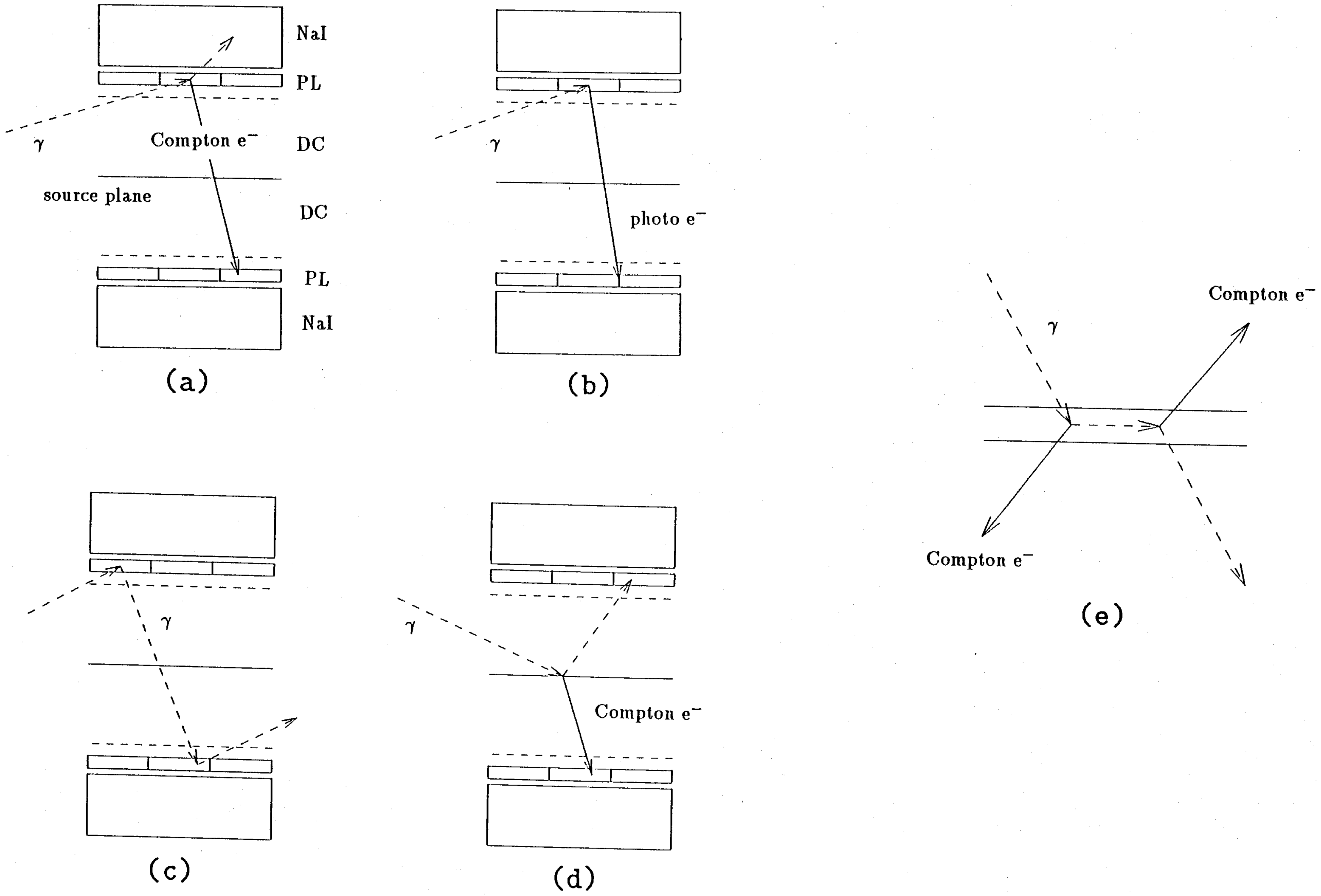
NaI
PL
γ
Compton e⁻
DC
source plane
DC
PL
NaI
(a)
γ
photo e⁻
(b)
γ
Compton e⁻
Compton e⁻
(e)
γ
(c)
γ
Compton e⁻
(d)

Fig. 4.2

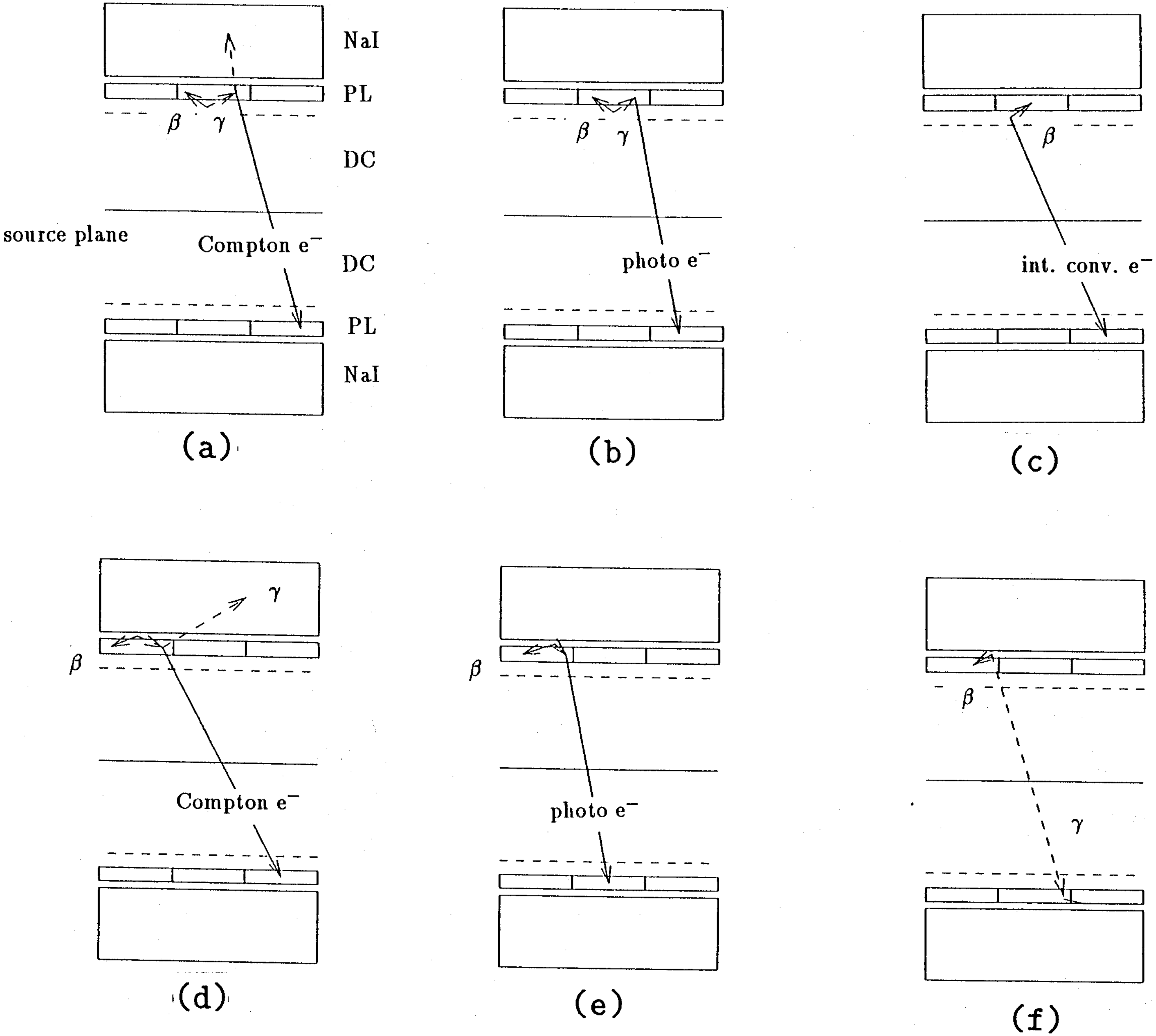
NaI
PL
DC
source plane
DC
PL
NaI
β
γ
Compton e$^-$
(a)
β
γ
photo e$^-$
(b)
β
int. conv. e$^-$
(c)
γ
β
Compton e$^-$
(d)
β
photo e$^-$
(e)
β
γ
(f)

Fig. 4.3

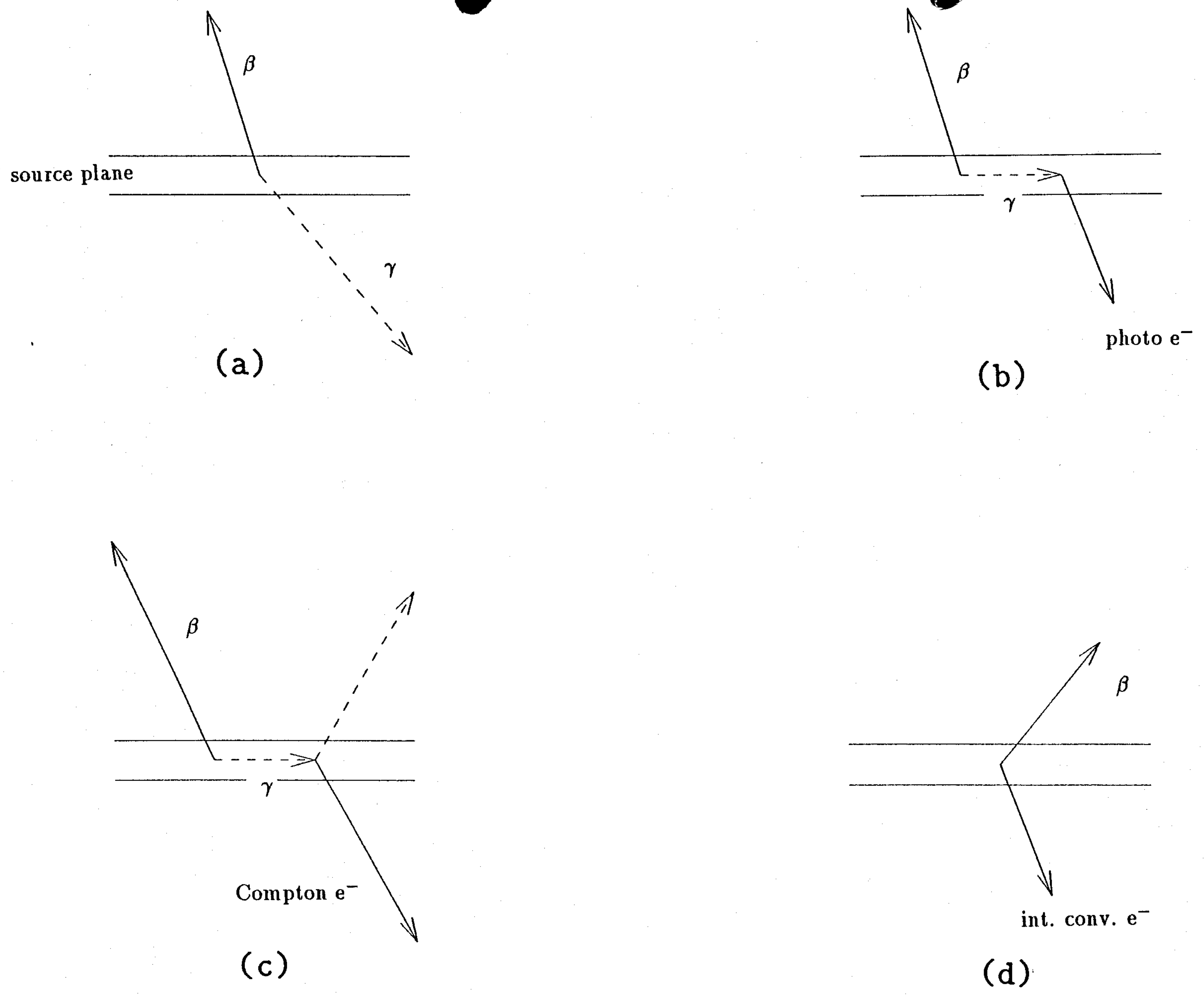
β
source plane
γ
(a)
β
γ
photo e^-
(b)
β
γ
Compton e^-
(c)
β
int. conv. e^-
(d)

Fig. 4.4

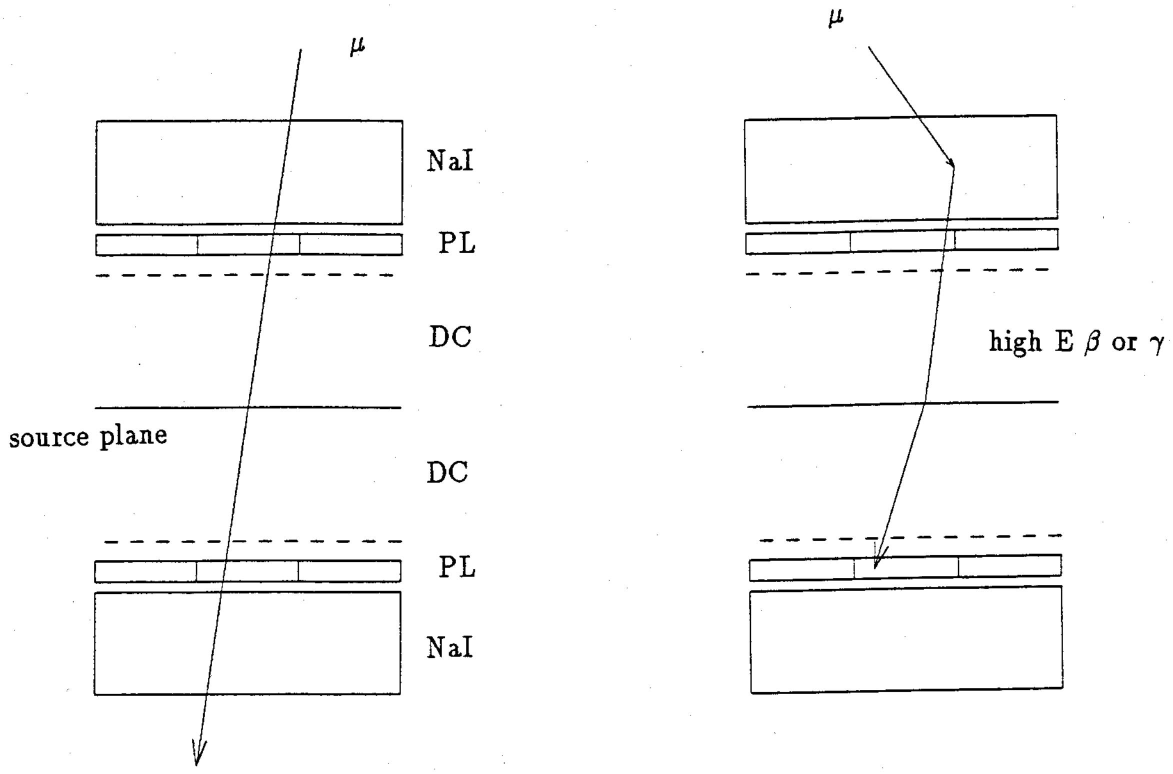

(a) (b)

Fig. 4.5

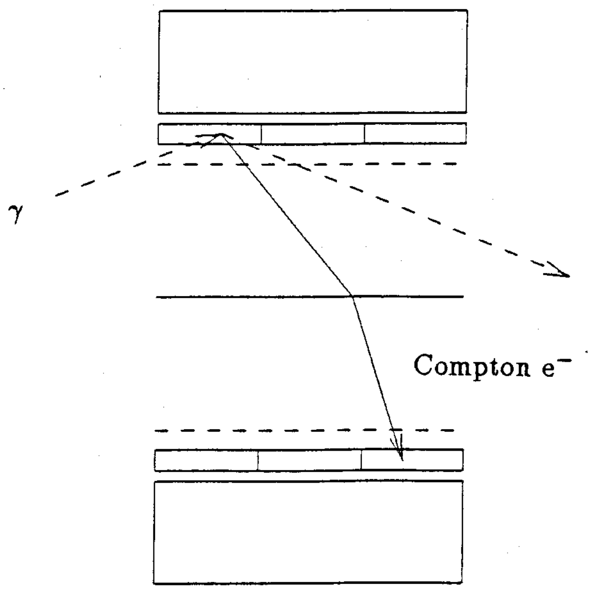

Fig. 4.6

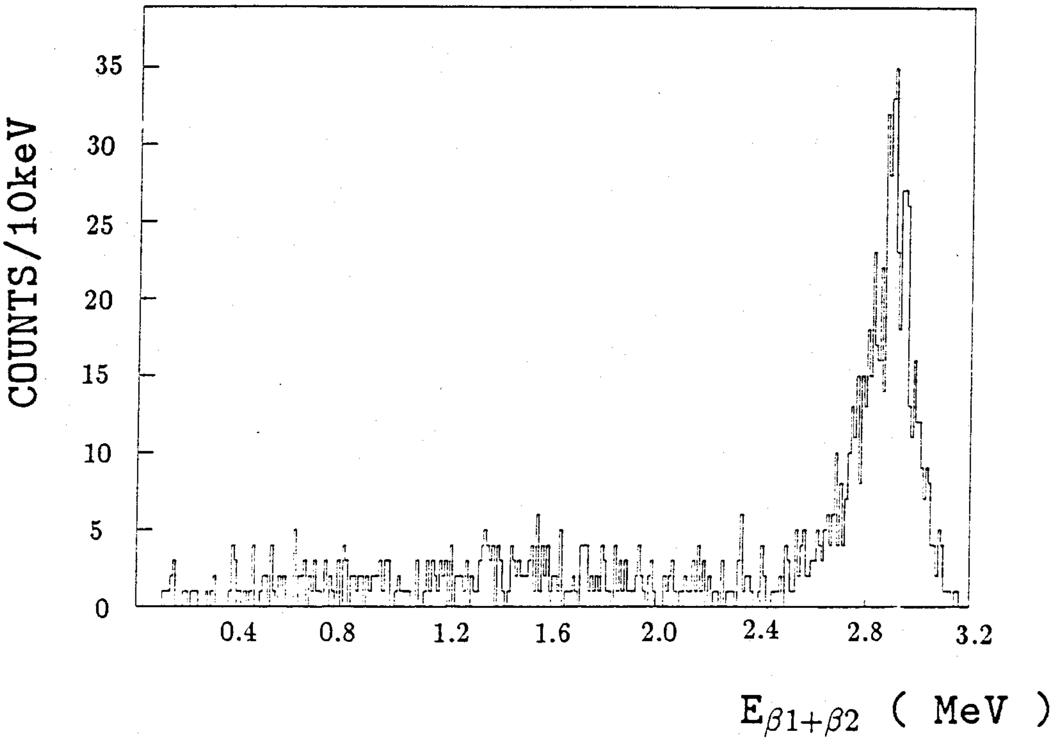
COUNTS/10keV
0
5
10
15
20
25
30
35
0.4
0.8
1.2
1.6
2.0
2.4
2.8
3.2
$E_{\beta1+\beta2}$ (MeV)

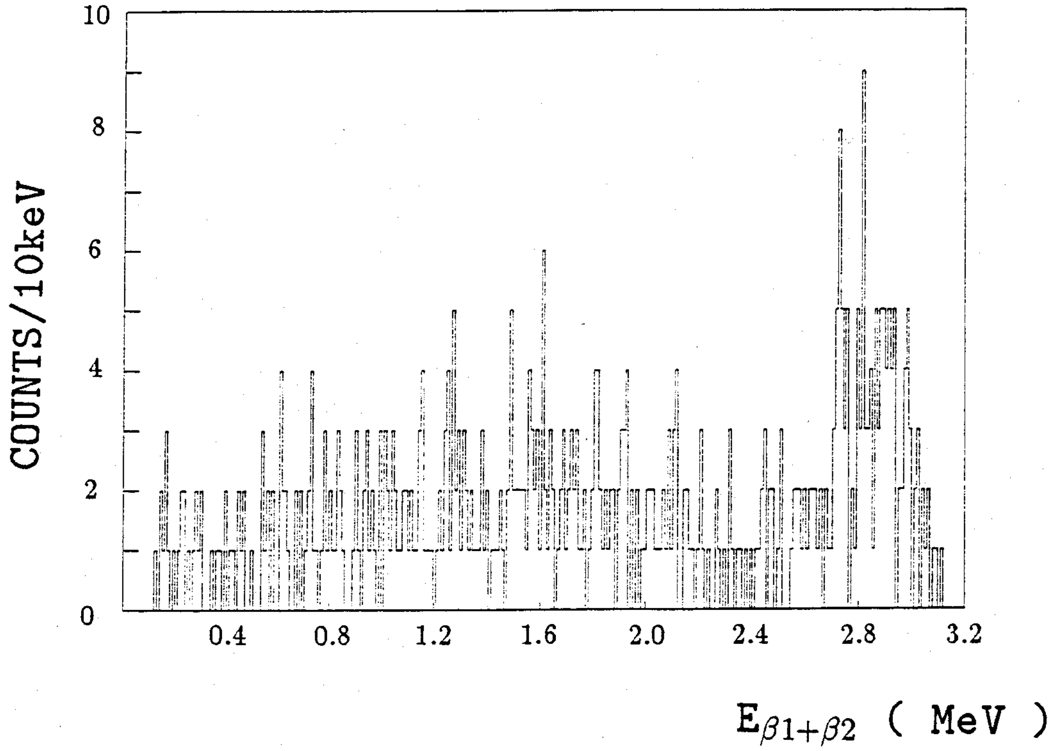
COUNTS/10keV
0
2
4
6
8
10
0.4
0.8
1.2
1.6
2.0
2.4
2.8
3.2
$E_{\beta1+\beta2}$ (MeV)

Fig. 4.7

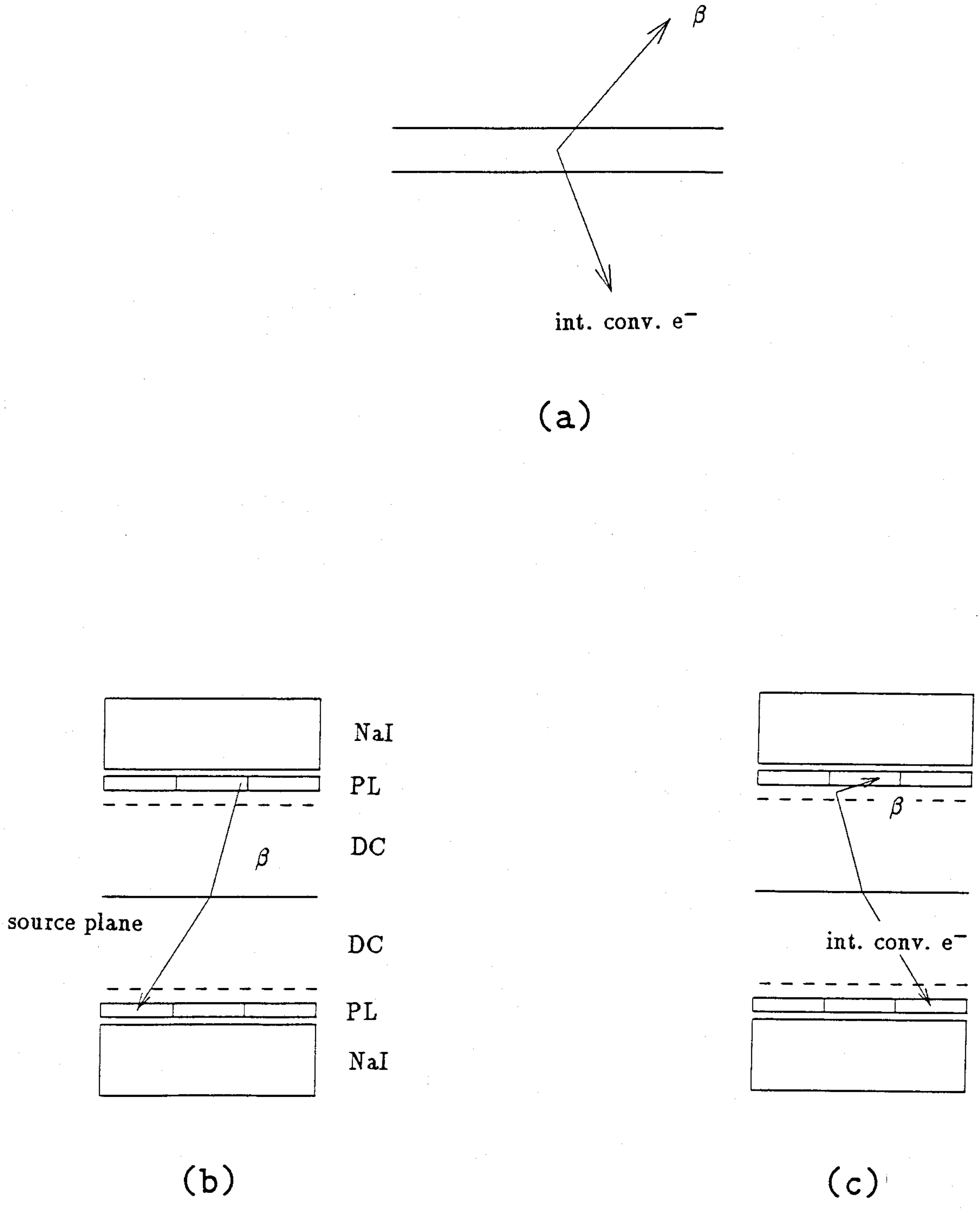

Fig. 4.8

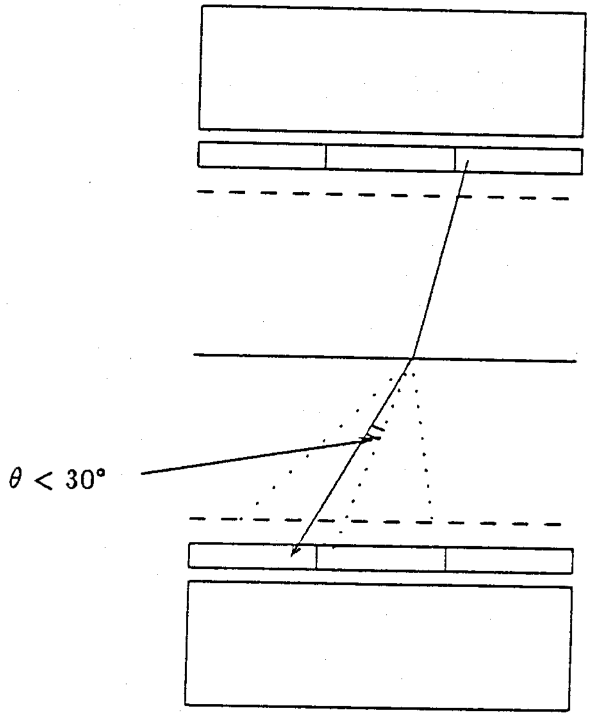

Fig. 4.9

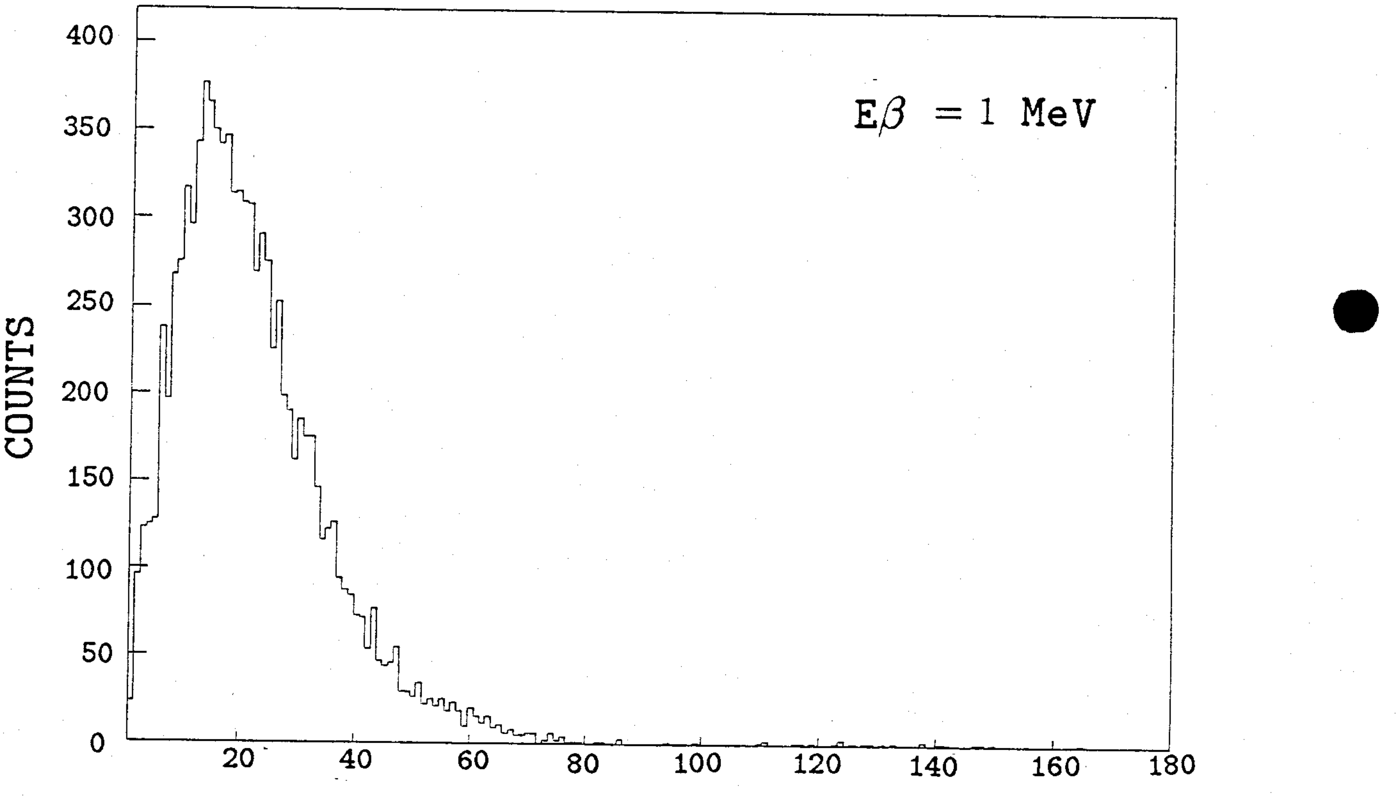

Fig. 4.10

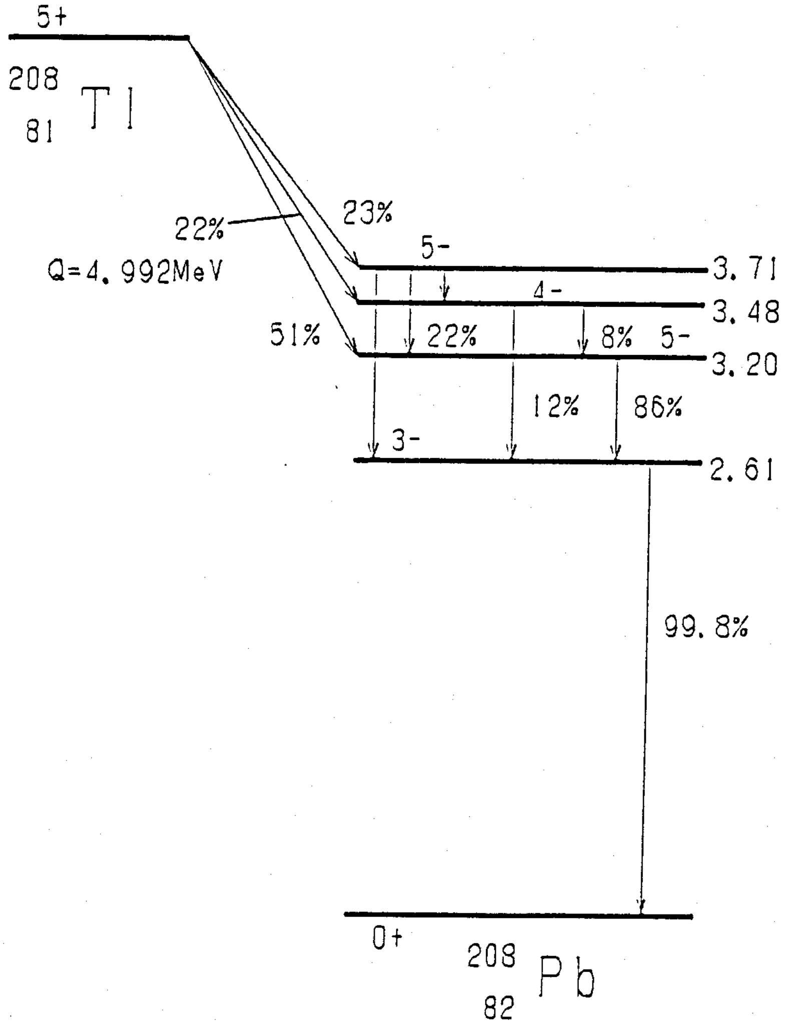
5+
208
81
Tl
22%
Q=4.992MeV
23%
51%
5-
3.71
4-
3.48
22%
8%
5-
3.20
12%
86%
3-
2.61
99.8%
0+
208
82
Pb

Fig. 4.11

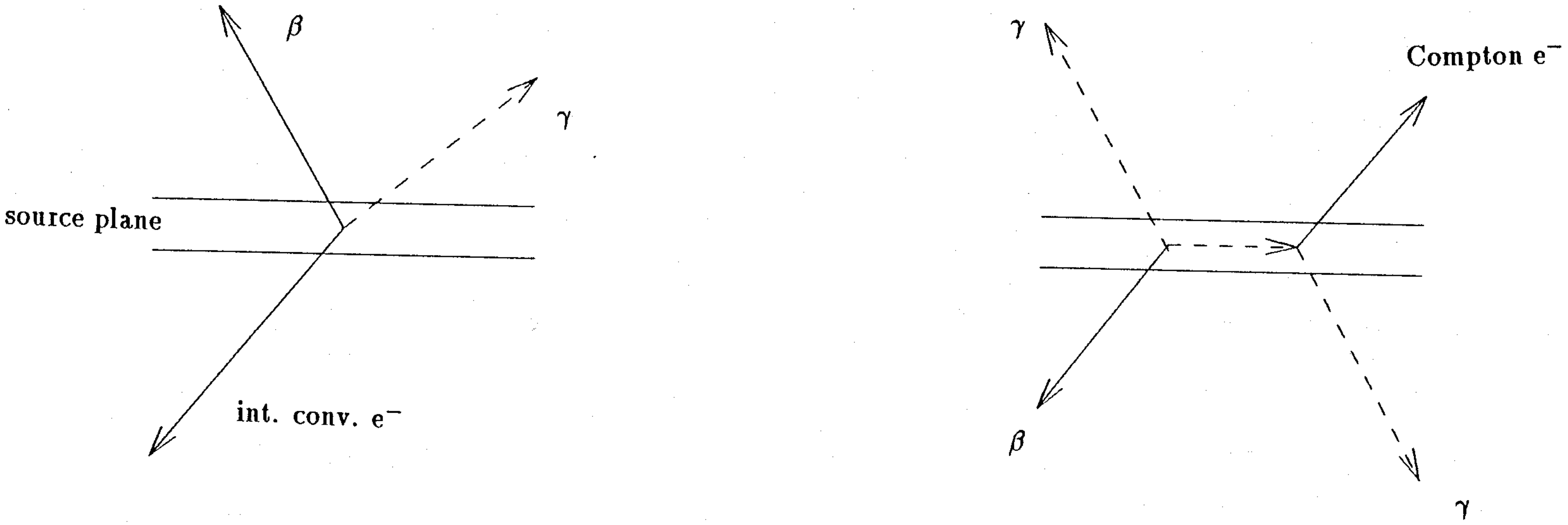

(a) (b)

Fig. 4.12

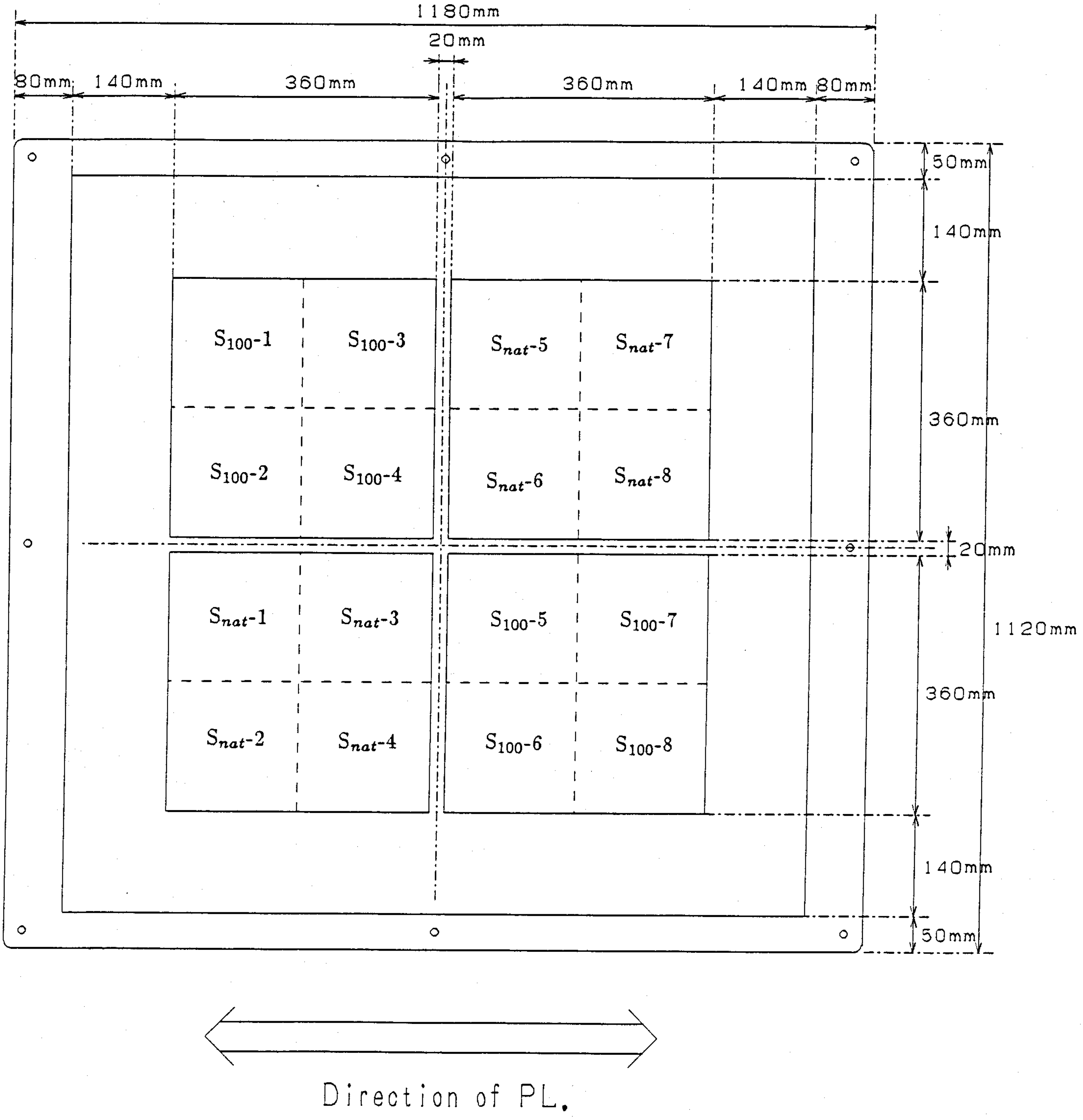
1180mm
20mm
80mm
140mm
360mm
360mm
140mm
80mm
50mm
140mm
360mm
20mm
1120mm
360mm
140mm
50mm
S100-1
S100-3
S100-2
S100-4
Snat-5
Snat-7
Snat-6
Snat-8
Snat-1
Snat-3
Snat-2
Snat-4
S100-5
S100-7
S100-6
S100-8
Direction of PL.

Fig. 5.1

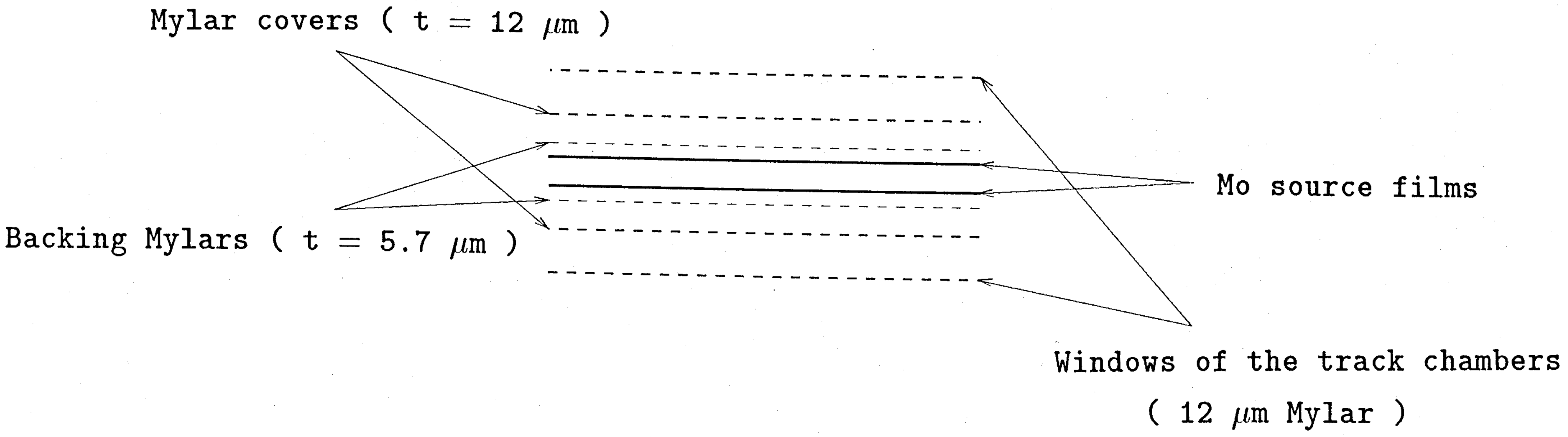
Mylar covers (t = 12 μm)
Backing Mylars (t = 5.7 μm)
Mo source films
Windows of the track chambers
(12 μm Mylar)

Fig. 5.2

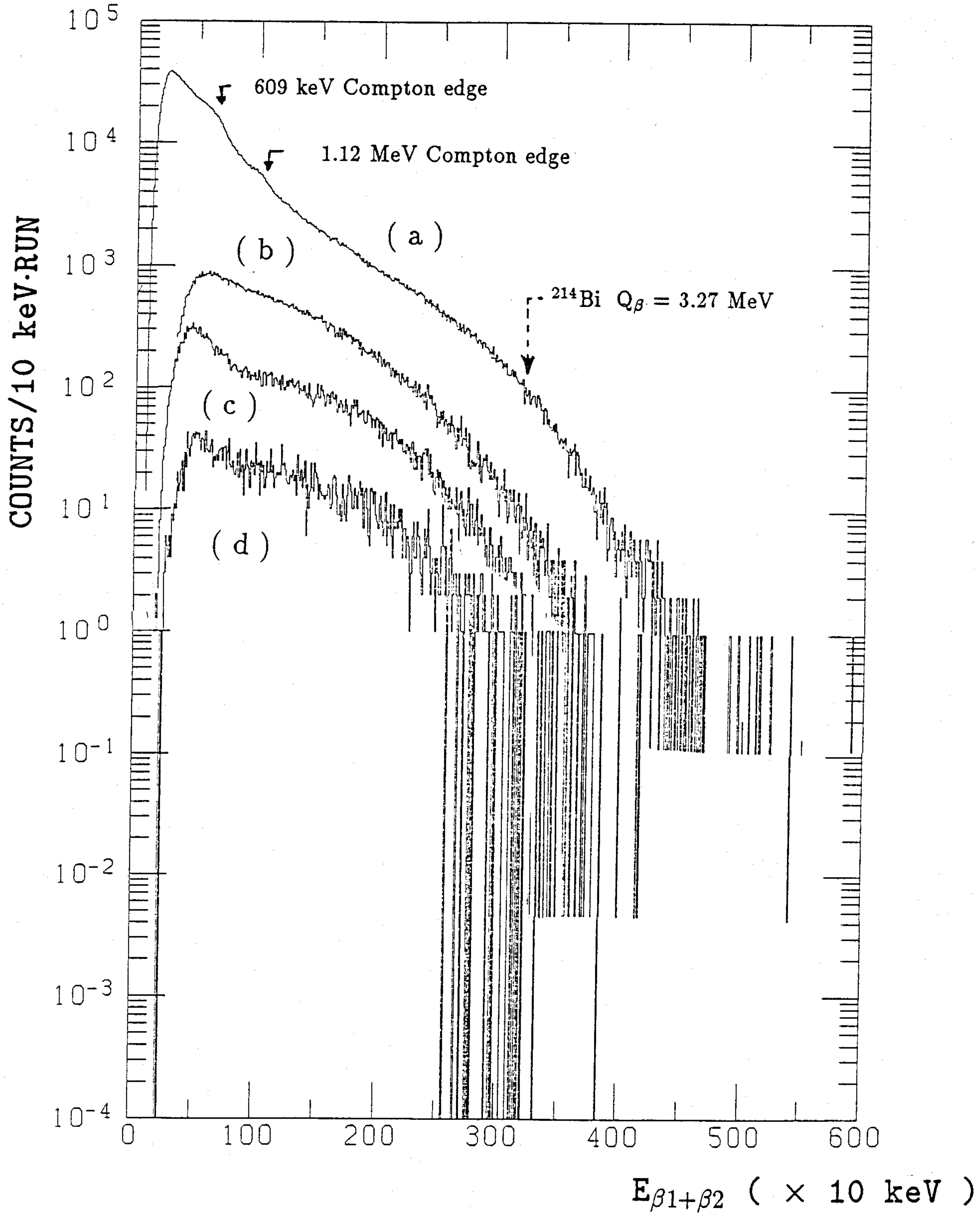
609 keV Compton edge
1.12 MeV Compton edge
(a)
(b)
(c)
(d)
^{214}Bi $Q_\beta = 3.27$ MeV
COUNTS/10 keV·RUN
10^5
10^4
10^3
10^2
10^1
10^0
10^{-1}
10^{-2}
10^{-3}
10^{-4}
0
100
200
300
400
500
600
$E_{\beta1+\beta2}$ (× 10 keV)

Fig. 6.1

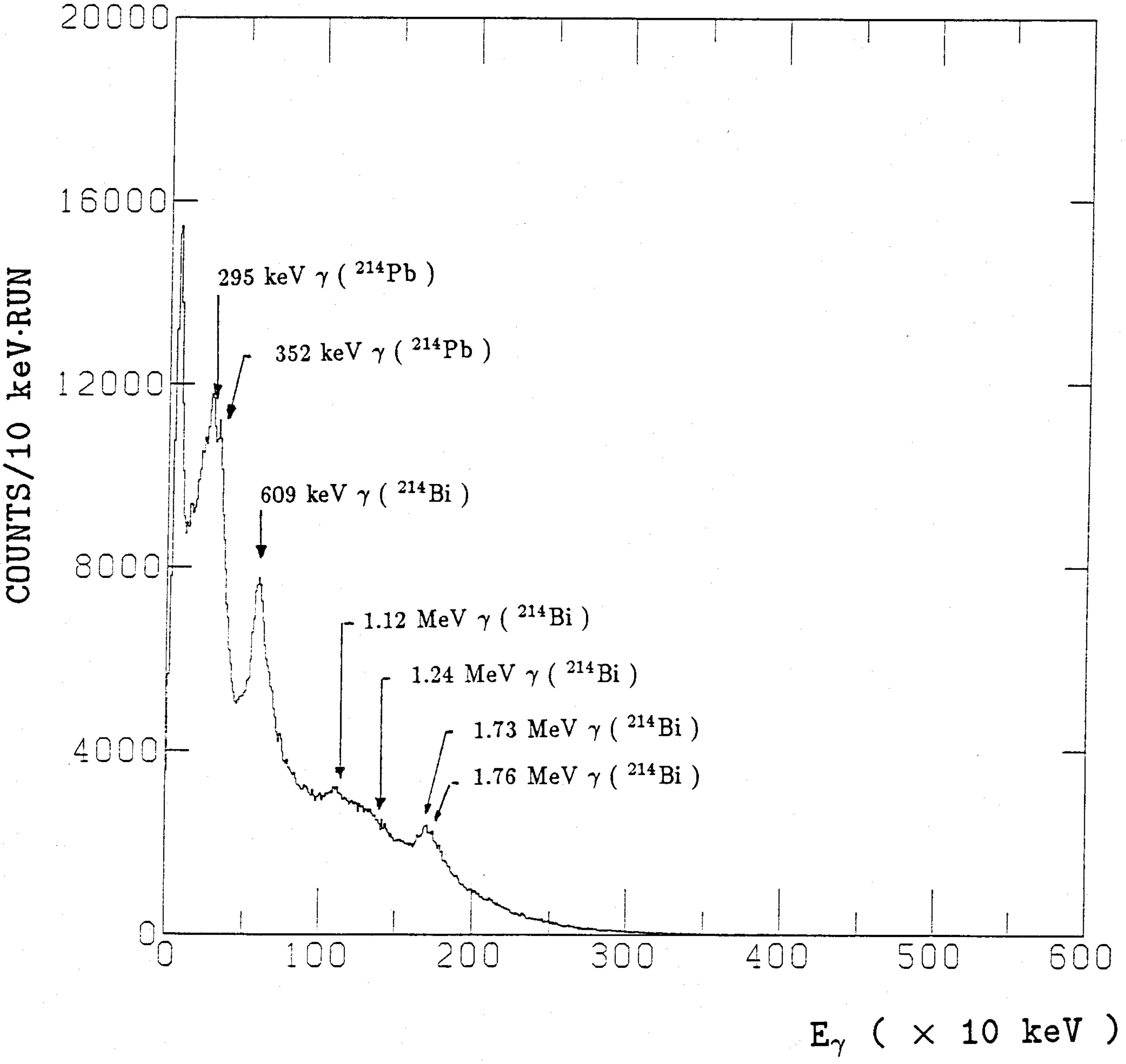

20000
16000
12000
8000
4000
0
0
100
200
300
400
500
600
COUNTS/10 keV·RUN
E_γ (× 10 keV)
295 keV γ (^{214}Pb)
352 keV γ (^{214}Pb)
609 keV γ (^{214}Bi)
1.12 MeV γ (^{214}Bi)
1.24 MeV γ (^{214}Bi)
1.73 MeV γ (^{214}Bi)
1.76 MeV γ (^{214}Bi)

Fig. 6.2

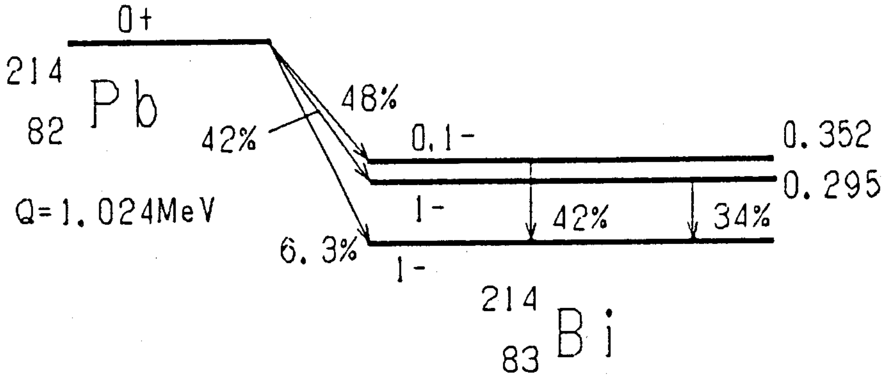

Fig. 6.3

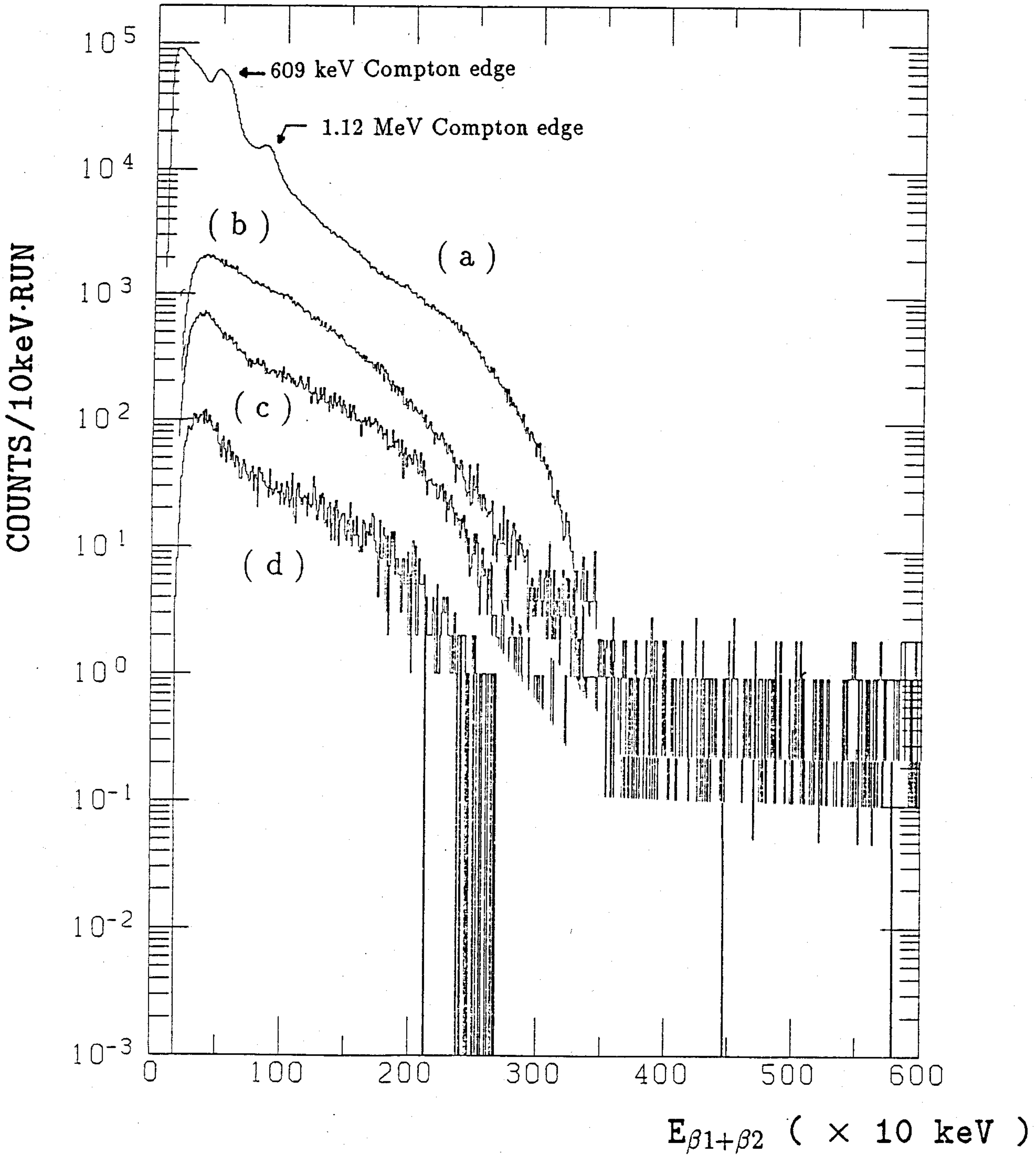
COUNTS/10keV·RUN
10^5
10^4
10^3
10^2
10^1
10^0
10^{-1}
10^{-2}
10^{-3}
609 keV Compton edge
1.12 MeV Compton edge
(a)
(b)
(c)
(d)
0
100
200
300
400
500
600
$E_{\beta1+\beta2}$ (× 10 keV)

Fig. 7.1

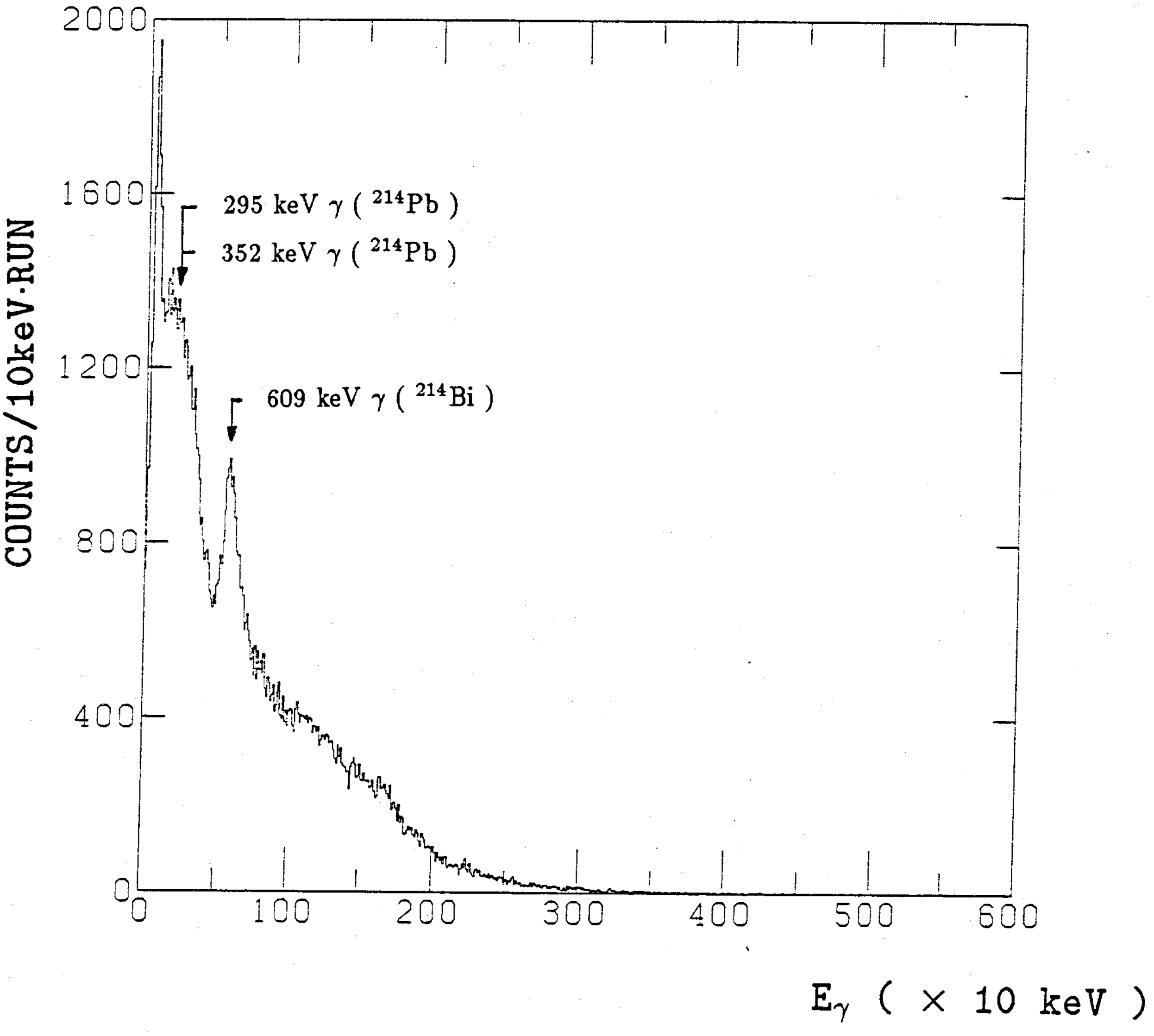
2000
1600
1200
800
400
0
COUNTS/10keV·RUN
295 keV γ (^{214}Pb)
352 keV γ (^{214}Pb)
609 keV γ (^{214}Bi)
0
100
200
300
400
500
600
E_γ (× 10 keV)

Fig. 7.2

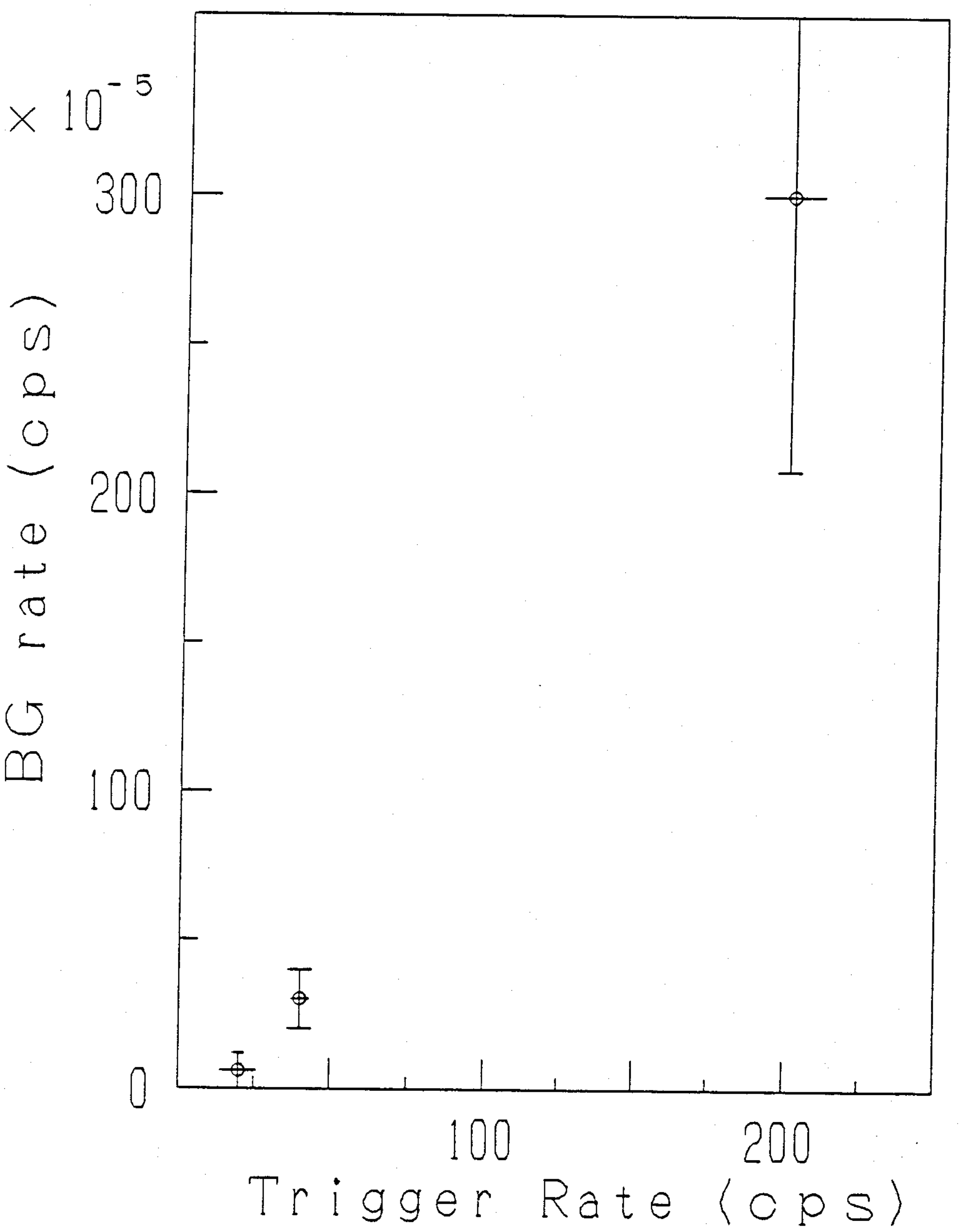

Fig. 7.3

Group	Mode (final state)	$T_{1/2}$ (yrs) (C.L.%)
Kiev (Ref. 1.15)	0ν	$> 1.5 \times 10^{21}$ (68)
Moscow(Ref. 1.16)	2ν	$= (0.8 \sim 6.0) \times 10^{18}$ (95)
LBL/Mt.H/UNM (Ref. 1.17)	0ν	$> 7 \times 10^{21}$ (1σ)
	2ν	$> 2.6 \times 10^{18}$ (90)
	0νB	$> 2.3 \times 10^{20}$ (90)
LBL(Ref. 1.12)	0ν (0^+)	$> 4 \times 10^{21}$ (68)
	0ν (2^+)	$> 4 \times 10^{20}$ (68)
Milan(Ref. 1.18)	0ν (2^+)	$> 1.4 \times 10^{18}$ (90)
Osaka(Ref. 1.11)	2ν	$> 5.4 \times 10^{18}$ (68)
	0ν (0^+)	$> 1.3 \times 10^{20}$ (68)
	0ν (2^+)	$> 2 \times 10^{19}$ (68)
	0νB	$> 4.9 \times 10^{18}$ (68)

Table 1.1 Experimental results of the ^{100}Mo $\beta\beta$ decay

Sample	U-chain (pCi/kg)	Th-chain (pCi/kg)	^{40}K (pCi/kg)
OFHC frame	< 0.24	< 0.20	< 3.1
Stainless Steel	< 0.38	0.31 ± 0.16	3.0 ± 1.6
Brass electrode	< 2.1	< 2.1	< 17
Feed through	< 3.1	< 1.6	< 18
Au-W wire	< 0.33	< 0.11	
OFHC wire	< 0.33	< 0.11	
Solder	< 1.6	< 0.5	
Flux	< 3.3	< 3.1	
HV cable	< 2.2	2.4 ± 0.9	14 ± 11

Table 3.1 Amounts of the radioactivities in the materials used for drift chambers.

Energy region	^{40}K 1.0 $\sim$ 1.2 MeV	^{208}Tl 1.8 $\sim$ 2.3 MeV	muon 3.0 $\sim$ 10.0 MeV	$2\nu\beta\beta$ range 0.7 $\sim$ 1.5 MeV	$0\nu\beta\beta$ range 2.6 $\sim$ 3.0 MeV	total
(raw data)	459507	102851	391448	1699389	40818	10484023
2 PLs coin.	62294	21301	327501	229504	7705	1016664
vetoed by NaI	12898	3622	148	44576	314	102071
DC > 5/6 coin.	2460	1414	62	8172	73	15515

Table 4.1 The numbers of residual events and the reduction efficiency at each reduction stage.

BG origin	contamination (ppb)	decay/yr	to be detected (events/yr)	reduction efficiency (reduction method)	residual (events/yr)
Bi(source)	< 0.5	$< 3.9 \times 10^4$	< 2.2	0.69 (α, K-X)	0.7
Bi(PL)	< 0.5	$< 5.6 \times 10^4$	< 270	0.999 (α, TOF, angle)	0.3
Tl(source-a)	< 0.5	$< 1.2 \times 10^4$	< 0.9	0.88 (γ, K-X)	0.1
Tl(source-b)	< 0.5	$< 1.2 \times 10^4$	< 1.3	0.99 (γ, vertex)	0.02
Tl(PL-a)	< 0.5	$< 1.7 \times 10^4$	< 120	0.998 (γ, TOF, angle)	0.3
Tl(PL-b)	< 0.5	$< 1.7 \times 10^4$	< 180	0.999 (γ, K-X, TOF, angle)	0.2
Total					1.6

Table 4.2 Estimated residual numbers of the backgrounds for $0\nu\beta\beta$ decay

Serial No.	Area (cm^2)	Mass (gramm)	Thickness (mg/cm^2)
nat-1	322.6	6.78	21.0
nat-2	323.1	6.66	20.6
nat-3	324.1	6.64	20.5
nat-4	322.6	6.63	20.6
nat-5	322.7	6.59	20.4
nat-6	322.1	6.50	20.2
nat-7	322.1	6.48	20.1
nat-8	321.7	6.45	20.0
nat-9	322.1	6.43	20.0
nat-10	322.1	6.41	19.9
nat-11	320.9	6.40	19.9
nat-12	322.1	6.37	19.8
nat-13	322.2	6.36	19.7
nat-14	322.0	6.31	19.6
nat-15	322.9	6.29	19.5
nat-16	323.9	6.28	19.4

natural Mo : mean thickness = 20.1 ± 0.1 g/cm^2

Serial No.	Area (cm^2)	Mass (gramm)	Thickness (mg/cm^2)
100-1	322.1	7.02	20.6
100-2	322.5	6.93	20.5
100-3	322.1	6.89	20.6
100-4	321.8	6.67	20.4
100-5	322.8	6.63	20.2
100-6	321.9	6.59	20.1
100-7	322.1	6.56	20.0
100-8	322.6	6.55	20.0
100-9	321.2	6.54	19.9
100-10	322.0	6.46	19.9
100-11	322.6	6.41	19.8
100-12	320.9	6.34	19.7
100-13	322.4	6.21	19.6
100-14	322.3	6.20	19.5
100-15	321.0	6.19	19.4
100-16	321.0	6.16	19.4

^{100}Mo : mean thickness = 21.5 ± 0.4 g/cm^2

Table 5.1 Data of natural Mo and ^{100}Mo source film (1)

Source No.		Thickness (mg/cm^2)
S_{100}-1	(100-1 + 100-16)	40.9
S_{100}-2	(100-2 + 100-15)	40.8
S_{100}-3	(100-3 + 100-14)	40.7
S_{100}-4	(100-4 + 100-13)	39.8
S_{100}-5	(100-5 + 100-12)	40.3
S_{100}-6	(100-6 + 100-11)	40.4
S_{100}-7	(100-7 + 100-10)	40.5
S_{100}-8	(100-8 + 100-9)	40.7
S_{nat}-1	(nat-1 + nat-16)	40.4
S_{nat}-2	(nat-2 + nat-15)	40.1
S_{nat}-3	(nat-3 + nat-14)	40.1
S_{nat}-4	(nat-4 + nat-13)	40.3
S_{nat}-5	(nat-5 + nat-12)	40.2
S_{nat}-6	(nat-6 + nat-11)	40.1
S_{nat}-7	(nat-7 + nat-10)	40.0
S_{nat}-8	(nat-8 + nat-9)	40.0

^{100}Mo : mean thickness = 40.5 ± 0.1 g/cm^2

natural Mo : mean thickness = 40.2 ± 0.05 g/cm^2

Table 5.1 Data of natural Mo and ^{100}Mo source film (2)

Material	U(ppb)	Th(ppb)	K (ppm)
Mo powder	< 0.5	< 0.5	1.2
Formvar powder	0.1	0.2	9.7
Mylar foil	< 0.5	< 0.5	2.6
cyclohexanone	< 0.01	< 0.01	~ 5 (ppb)
Chloroform	< 0.01	< 0.01	< 1 (ppb)
Mo film	< 0.5	< 0.5	2.2

Table 5.2 Contamination levels of U, Th, and K in the source materials.

Cut	Events	Reduction ratio
(raw data)	4329808	1/1
2 PLs coin.	163401	1/25
vetoed by NaI	45905	1/100
DC $>$ 5/6 coin.	6305	1/700
Hit pattern anal.	$\sim$ 3000	1/1400

Table 7.1 The numbers of residual events and the reduction efficiency at each reduction stage.

Refferences

Ref 1.1 T. Yanagida, Proc. Workshop on Unified Theory and Baryon Number in the Universe, edited by Sawada and Sugamoto, (KEK, 1979).
M. Gell-Mann, P. Ramond, and R. Slansky, in Supergravity, edited by van Nieuwenhuizen and Freedman, (North-Holland,Amsterdam, 1979).
G. Senjanoviç and R. N. Mohapatra, Phys. Rev. Lett. 44 (1980) 912.

Ref. 1.2 H. Primakoff and S.P. Rosen, Phys. Rev. 184 (1969) 1925

Ref. 1.3 J.D. Vergados, Phys. Rev. D 25 (1982) 914

Ref. 1.4 J.D. Vergados and R.N. Mohapatra, Phys. Rev. Lett. 47(1981)1713

Ref. 1.5 R.N. Mohapatra, Phys. Rev. D 34 (1986) 3457
J.D. Vergados, Phys. Lett. 184B (1987) 55

Ref. 1.6 K. Grotz and H.V. Klapdor, Nucl. Phys. A460 (1986) 395

Ref. 1.7 W.C. Haxton, G.J. Stephenson and D. Strottman, Phys. Rev. D 25 (1982) 2360, Phys. Rev. Lett. 47 (1981) 153.
M. Doi, T. Kotani, and E. Takasugi, Prog. Theoretical Phys., Supplement 83 (1985).
R.N. Mohapatra and E. Takasugi, preprint Osaka, OS-GE-88-02 (1988)
H. Primakoff and S.P. Rosen, Rept. Prog. Phys. 22 (1959) 121.

Ref. 1.8 P.O.Caldwell, R.M. Eisberg, D.M. Grumm, D.L. Hale, M.S. Witherell, F.S. Goulding, D.A.Landis, N.W. Madden, D.F. Malone, R.H. Pehl, and A.R. Smith, Phys. Rev. D. 33 (1986) 2737, Phys. Rev. Lett. 54 (1985) 281.
E. Fiorini et al., Phys. Lett. 25B (1967) 602, Nuovo Cimento
E. Belloti et al., Phys. Lett. 146B (1984) 450, Nuovo Cimento 95A (1986) 1.
F.T. Avignone III et al., Phys. Rev. Lett. 50 (1983) 721, Phys. Rev. C34 (1986) 666.
J.J. Simpson et al., Phys. Rev. Lett. 53 (1984) 141.
H. Ejiri et al., Nucl. Phys. A448 (1986) 271, Proc. Int. Conf. Neutrino Masses and Neutrino Astrophysics, Telemark, 1987, p281.
P.Dassie et al., Nuovo Cimento A85 (1985) 19.

Ref. 1.9 M.Z. Iqbal et al., Proc. Int. Conf. Neutrino Masses and Neutrino Astrophysics, Telemark, 1987, p317.
E. Bellotti et al., Proc. Int. Conf. Neutrino Masses and Neutrino Astrophysics, Telemark, 1987, p307.

Ref. 1.10 S.R. Elliott, A.A. Hahn and M.K. Moe, Phys. Rev. Lett. 56 (1986) 2582, Phys. Rev. Lett. 59 (1987) 1649, UCI Neutrino No. 87-27 (1987)

Ref. 1.11 T. Watanabe, Dr. thesis., Osaka Univ., 1988.
H. Ejiri et al., Proc. Int. Conf. Neutrino Masses and Neutrino Astrophysics, Telemark, 1987, p281.

Ref. 1.12 M. Alston-Garnjost et al., Phys. Rev. Lett. 63 (1989) 1671.

Ref. 1.13 K. Muto and H.V. Klapdor, Phys. Lett. B201 (1988) 420

Ref. 1.14 T. Tomoda et.al., Nucl. Phys. A452 (1986) 591
T. Tomoda and A. Faessler, Phys. Lett. B199 (1987) 475
P. Vogel and M. Zirnbauer, Phys. Rev. Lett. 57 (1986) 3148

Ref. 1.15 Yu. Zdesenko et al., Proc. Int. Conf. Neutrino'82, Balatonfured, Hungary, 1982, p209.

Ref. 1.16 A.A. Klimenko et al., Proc. Yamada Conf. Nucl. Weak Process and Nucl. Structure, Osaka, 1989, p180.

Ref. 1.17 M. Alston-Garnjost et al., Proc. Int. Conf. Neutrino Masses and Neutrino Astrophysics, Telemark, 1987, p298.
M. Alston-Garnjost et al., Phys. Rev. Lett. 60 (1988) 1928.

Ref. 1.18 E. Belloti, E. Fiorini et al., AIP Conf. Proc. Telemark'82, p99.

Ref. 1.19 T. Kirsten et al., Proc. Int. Symp. Nucl. Beta Decays and Neutrino, Osaka, 1986, p81.
O.K. Manuel, Proc. Int. Symp. Nucl. Beta Decays and Neutrino, Osaka, 1986, p71.

Ref. 1.20 K. Okada et al., Proc. Int. Conf. PANIC 87, Kyoto, Nucl. Phys. A478 (1988) 447c.

Ref. 2.1 M.Z. Iqbal et.al., Nucl. Inst. Methods A259 (1987) 459
see also Ref. 1.9.

Ref. 2.2 See Ref. 1.16.

Ref. 2.3 H. Ejiri, T. Shibata, Y. Nagai and S. Nakayama, Nucl. Inst. Methods 134 (1976) 107

Ref. 3.1 F. Sauli, 'Principles of operation of Multi Wire and Drift Chambers' Textbook of Academic Training Programme of CERN.
G. Charpak, R. Bouclier,et.al. Nucl. Inst. Methods 62 (1968) 235

Acknowledgement

The author would like to thank Professor H. Ejiri for valuable discussions, suggestions, and his very kind encouragement throughout this work. He also thanks Professor T. Shibata, Dr.'s K.Okada, H.Ohsumi, H. Sano, N. Kamikubota, and T. Watanabe for their kind collaborations and discussions during whole course of this experiment. The author is deeply indebted to all other members of the Ejiri's group at Dept. Phys. and OULNS, Osaka Univ., who are graduate students; J. Tanaka, T. Taniguchi, H. Kobiki, N. Tanabe, N. Yamamoto, H. Kinoshita, and K. Fushimi, and technical staffs; K. Matsuoka, K. Higa, H. Iwata, T. Mizuta, and K. Onishi, and secretaries; S. Tsuzuki and R. Gokoh.

The author and collaborators wish to thank Professors M. Koshiba, Y. Totsuka, and K. Nakamura, Univ. of Tokyo and Inst. for Cosmic Ray Research, and H. Suda, Kobe Univ. for their kind arrangements and encouragements at the Kamioka underground lab. Thanks are also due to Kamioka Mining & Smelting Co., Ltd. for the help at the Kamioka mine.

The author wishes to thank Professors T. Kotani, E. Takasugi, M. Doi, H. Nishiura, and K. Muto for valuable discussions and suggestions.

Construction of the track chambers were performed at National Lab. for High Energy Phys. The author would like to acknowledge his best thanks to Professor T. Inagaki for his kind arrangements and encouragements. He is also quite grateful to Mr. Shimazu, Mr. Miura, Mr. Ohkuma, Mr. Konno, Mr. Harada, Mr. Ochiai, Mrs. Kato, Mrs. Sato, Mrs. Sugiura, and other members of REPIC Co., Ltd. Actually construction of the chambers have never been performed without about twenty people's efforts and favors.

The author would like to thank Nippon Mining Co., Ltd. Refinement and analysis of Mo source were performed by their kind collborations.

The author wishes to express his best regard to his families Kei, Mizue, and Wakako Shima for their continuous helps and encouragements.

Finally, the author wishes to thank to his best friend Mr. Takehiro Kamada. This work could never be accomplished without his inestimatable efforts and favors. These drift chambers are really the symbol of the friendship between him and the author.